Self-propelled particles driven by light

Von der Fakultät Mathematik und Physik
der Universität Stuttgart
zur Erlangung der Würde eines Doktors der Naturwissenschaften (Dr. rer. nat.)
genehmigte Abhandlung

von

Ivo Buttinoni

aus Treviglio (BG), Italien

Hauptberichter: Prof. Dr. Clemens Bechinger
Mitberichter: Prof. Dr. Peer Fischer

Tag der mündlichen Prüfung: 22-10-2013

2. Physikalisches Institut der Universität Stuttgart

2014

Contents

1

Part I

Theoretical background

Chapter 1

Self-propulsion of micrometric objects

The past 50 years registered a growing interest towards the motion of micrometric objects in viscous fluids. The peculiarity of these systems consists in a very awkward hydrodynamics in contrast with what we are used to observe in the macroscopic world.

The development of microscopy techniques showed that microorganisms like bacteria and cells have to employ clever strategies in order to propel themselves upon such conditions. Needless to say, the understanding of the motion of eukaryotic and prokaryotic microswimmers is a fundamental issue in biology, biophysics as well as in medical science. In the last decade, physicists also put a lot of effort to mimic the propulsion of biological microorganism using artificial micro-robots or self-propelled particles. Manmade micro-engines could in fact yield thriving opportunities for drug delivery applications.

In this Chapter, I will present the main features of self-propulsion of micrometric objects, both biological and artificial. I will describe how their hydrodynamics is strongly affected by the absence of inertial effects and what this implies in terms of ability to swim. I will provide a short glimpse over biological systems, e.g., bacteria and cells, focusing then on how these swimming tactics can be emulated artificially. Finally, I will introduce few paradigmatic examples of how artificial propellers could be exploited for delivery application.

1.1 Swimming at low Reynolds number

Our physical intuition and everyday experience of the concept of "swimming" are often misleading in the microscopic world. The swimming style a scuba diver uses to proceed underwater would indeed not work at smaller

length scales. This enormous behavioral difference is strictly related to the role of *inertia*.

In short, the hydrodynamic properties of the motion of an object swimming in a liquid of viscosity η is described by the classical Navier-Stokes equation (1.1):

$$-\nabla\rho + \eta\nabla^2\mathbf{v} = \rho\frac{\partial\mathbf{v}}{\partial t} + \rho(\mathbf{v}\cdot\nabla)\mathbf{v}, \tag{1.1}$$

where $\mathbf{v}$ and ρ are the velocity and the density of the floating object, respectively. The terms on the right-hand side are responsible of the high non-linearity related to the emergence of *inertia*. Back to the easy example of the scuba diver, the presence of these non-linear effects facilitates the motion since the swimmer experiences a glide forward even after a stroke.

However, inertia-driven phenomena tend to fade either when the surrounding fluid is too viscous or when the immersed object becomes too small. In order to quantify the contribute of inertia to the overall motion, we generally rely on the dimensionless Reynolds number which indicates the ratio of inertial forces to viscous forces. Its mathematical expression reads as follows (1.2):

$$Re = \frac{av\rho}{\eta}, \tag{1.2}$$

where a embodies the size of the object. When $Re \gg 1$ the motion is dominated by inertia as in several phenomena at the macroscopic scale; for instance, for a man swimming in water, $Re \sim 10^4$. On the other hand, when a drops to the micrometric length scale, the Reynolds number becomes much smaller than 1 as in the case of bacteria swimming in water where $Re \sim 10^{-4}$. Very viscous fluids produce the same effect since η appears in the denominator of Eq.(1.2).

If $Re \ll 1$, the Eq.(1.1) turns out to be linear since the right-hand terms are approximatively 0. Due to this linearity a stroke forward is perfectly cancelled out by an identical stroke backward, resulting in no net displacement. Hence, compared to the scuba diver's predicament, an additional effort is needed to achieve a net propulsion at low Reynolds number.

This idea has been nicely illustrated by Purcell in a famous article from the 70s [1]. To clarify the dilemma about propulsion at low Reynolds number Purcell formulated the well-known *Scallop Theorem*. A scallop (see Fig.1.1(a)) is probably one of the simplest animal in nature, yet it is able to swim in seawater just by opening and closing its shell, i.e., exploiting only one degree of freedom. Nonetheless, in the absence of inertia, i.e., at low Reynolds number, a scallop would not manage to move forward and would wind up performing a *reciprocal motion*. The only way to achieve a propulsion without inertia consists in breaking *time-reversal symmetry* by having motors with more than one degree of freedom. This can be done, for
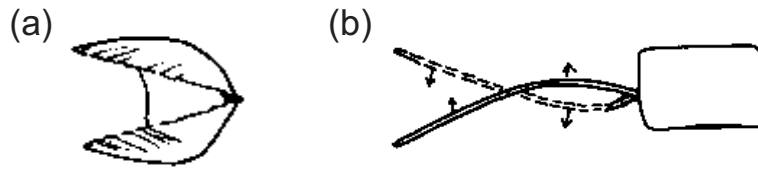
Figure 1.1: Sketches taken from Purcell's paper "Life at low Reynolds number" [1]. At low Re a scallop (a) does not swim whilst an organism equipped with a flexible oar (b) does.

instance, through a flexible wiggling motor linked to the object's body as illustrated in Fig.1.1(b).

Nevertheless, a flexible oar is certainly not the only solution. In the next Section, I will describe how biological microorganisms, whose small size yields a $Re \ll 1$, overcome the impasse of navigating in a liquid in the absence inertia.

1.2   Biological microswimmers

Bacteria, algae and cells are biological organisms whose size varies from few up to hundreds microns; therefore, when floating in aqueous solutions, they behave as overdamped inertia-free systems and, as previously mentioned, the locomotion strategy requires more than one degree of freedom to produce a net propulsion. For this reason, Nature decided to supply them with flexible filaments that are embedded as appendices of the body. These lashes are called *flagella* or *cilia*, meaning in Latin "whips" and "eyelashes", respectively; the distinction between the two terms is not rigorous but varies from organism to organism, although usually rests on either their length (*cilia* are often shorter) or their function [2].

When propelling the microorganism, these appendices deform in order to trigger a non-reciprocal motion; due to the reasons extensively discussed in §1.1 the propulsive and the recovery strokes must break the time-reversal symmetry. In short, two very distinguishable propulsive mechanisms have been so far observed [3]: the *screw-like rotation* and the *whip-like beat* (Fig.1.2).[1]

- *Screw-like* micromotors usually rely on the presence of one or several flagella, often longer than the body of the microorganism. These filaments are rigid, exhibits an helical shape and, when rotating, man-

---

[1]The beating mode is often ascribed to ciliary motion, while the rotating mode is attributed to the flagellar one. Although this distinction is fairly accepted amongst certain communities, it clashes with few counterexamples, e.g., the *Chlamydomonas reinhardtii* whose flagella exhibits a beating motion. [4]
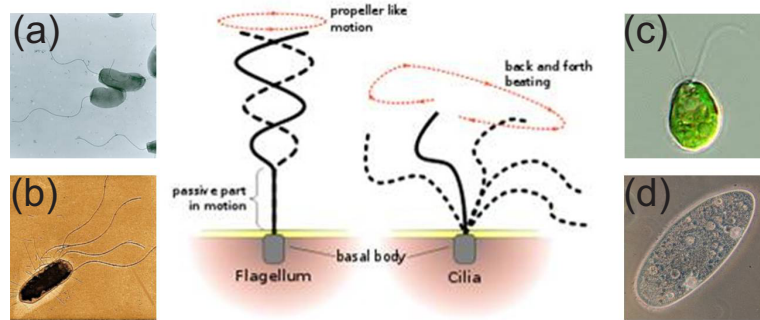
Figure 1.2: Examples of biological propulsion mechanisms (sketch taken from Wikipedia). Bacteria and biological cells can be pushed by the rotation of helical flagella (left) or pulled by the whip-like beating of flexible cilia (right). Examples of the first type are the (a) *Vibrio Cholerae* (picture taken from http://news.ucsc.edu/2009/12/3429.html) and the *Escherichia Coli* (picture taken from Wikipedia), whilst the (c) *Chlamydomonas reinhardtii* alga [6] and the (d) *Paramecium* protozoa (picture taken from Wikipedia) belong to the latter.

age to break the symmetry causing a directed motion of the organism. The flagella often push the cell body forward as rear motors, although counterexamples exists where the screw-like rotation actually pulls the cell (e.g., *Caulobacter crescentus* [5]). Each microorganism can be equipped either with one single flagellum, like the *Vibrio Cholerae* bacterium (Fig.1.2(a)), or with multiple filaments that bundle together hydrodynamically, e.g., in the case of the *Escherichia Coli* bacteria (Fig.1.2(b)).

• *Whip-like* motors exploits the deformation of short flexible filaments (cilia), embedded to the cell body. These appendices often wiggle simultaneously in order to amplify the strength of the strokes.

Thanks to the development of microscopy and particle tracking techniques, the motion of the these biological swimmers has attracted the interests of the physics community during the second half of the last century. Their trajectories have been identified as the first experimental example of the so-called *active Brownian motion*, i.e., a novel type of motion that rises from the coexistence of Brownian and ballistic features.

The *E.coli* bacterium has been chosen, among all the available bacterial species, as model system because of its handiness as well as its low microbiological dangerousness. Furthermore, its typical size of the order of few microns implies that the Brownian component plays a role in the overall motion of these microorganisms. Pioneering studies concerning the active
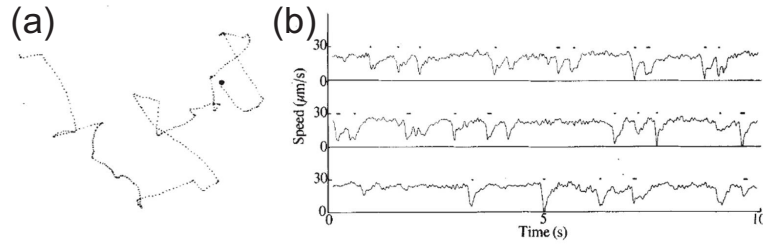
Figure 1.3: (a) Persistent random walk of an *E.coli* bacterium: the trajectory is characterized by ballistic "runs" alternated with random reorientations ("tumbles") [8]. (b) Speed during a "run and tumble" motion. The velocity drops to zero when the bacterium tumbles [8].

motion of these bacteria have been performed by H. Berg and coauthors [7, 8]. As mentioned above, in order to swim through a liquid, *E. coli* bacteria exploit the screw-like rotation of helical flagella that propel the cell body forward. In particular, these appendices possess a left-handed configuration and they thus wrap together when the rotation happens to be counter-clockwise. On the other hand, when the flagella rotate clockwise, they unbundle and stretch out uniformly; by doing so, the motion is arrested and the *E.coli* only fluctuate until a new random direction is chosen. The motion of these biological organisms is therefore defined by the so-called *run* and *tumble* events, i.e., the bacterium is propelled along straight ballistic runs and reorients randomly while tumbling. The tumbling rate determines the length of the ballistic segments, i.e., long runs correspond to low tumbling rates. Inside an homogeneous environment, the average length of the runs is roughly constant and therefore acts as a *persistence length* of the effective random walk. A typical resulting trajectory is shown in Fig.1.3 alongside with the swimming speed. Under starving condition, a migration up the food gradient is possible by adjusting the persistence length to the concentration of nutrients. In particular, runs are longer up the gradient. This process is known as *chemotaxis*.

Within Chapter 3 I will address in detail the properties of the persistent random walk (or active Brownian motion); for the time being, it's enough to stress that the active motion of these complex living organisms can be described by a simple model that takes into account propulsive events occurring at short time intervals mediated by a large time scale random diffusion. In spite of the simplicity of the model, tons of novel physical phenomena spring from this type of motion.

7

1.3   Bio-inspired artificial microswimmers

Inspired by the amazingly efficient design of natural cilia and flagella, during the past decades scientists and engineers committed themselves to mimic these swimming strategies using suitably assembled artificial micro- and nano-motors.
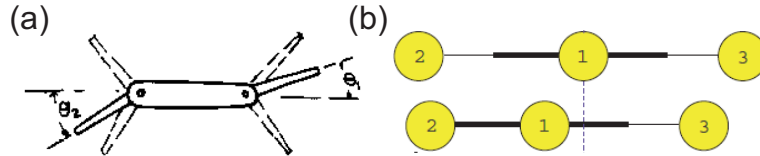
Figure 1.4: (a) A drawn of Purcell's model swimmer. The angles θ_1 and θ_2 change periodically in order to break the symmetry [1]. (b) Schematic representation of the Golestanian's swimmer which is essentially a 1D simplification of (a) [9].

The key-ingredient to devise a successful swimmer consists in breaking the time reversal symmetry, as underlined in §1.1. Back to the 70s, Purcell already proposed a simple hypothetic swimmer consisting of three rigid arms (see Fig.1.4(a)) that periodically change the two angle θ_1 and θ_2 and, thus, break the symmetry. More recently Golestanian and coworkers have presented a 1D simplified model (Fig.1.4(b)) of such oscillatory motors, where three beads are linked by rigid rods that vary their length periodically between two values. Despite its naiveté, this model clearly shows how a periodic cycle can break time reversal symmetry and, therefore, provide a directed propulsion.

Flagella- and cilia-inspired micromotors follow the same driving mechanism, cleverly elucidated by Golestanian, and perform a complex periodic strokes with several features in common with bacterial locomotion. This Section aims to present few paradigmatic examples of recent realization of bio-inspired microswimmers. Nonetheless, a complete list of experimental accomplishments is beyond the scope of this Chapter.

Microorganisms equipped with *cilia* are usually propelled due to the whip-like beating of these appendices (see §1.2). A similar stroke can be achieved also artificially by realizing a waving snake-like propeller which can be obtained, for instance, linking in a row a certain number of spherical colloids and agitating them with an external field [10]. In Ref. [10] colloidal superpamagnetic particles, coated with streptavidin, are tethered together with double stranded DNA linkers and lined up under an external uniform magnetic field as illustrated in Fig.1.5. The so-assembled "snake" is then actuated by oscillating a magnetic field perpendicular to it. The wiggling produced by the oscillation emulates the biological ciliary beating and is sufficient to break time reversal symmetry acting, thus, as a driving micro-
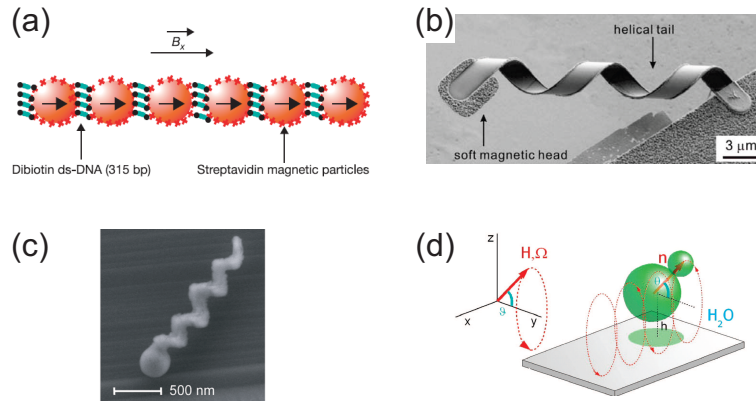
Figure 1.5: (a) A cilia-inspired magnetic microswimmer. It consists of a snake of magnetic beads, linked by DNA and aligned with an uniform magnetic field. The active motion is then triggered by an further magnetic field oscillating perpendicularly to the snake [10]. (b-d) Flagella-inspired magnetic microswimmers. (b) Helical ribbon supplied with a soft magnetic head [11]. (c) SiO_2 propeller coated with a ferromagnetic material (cobalt). (d) DNA-bounded paramagnetic beads subjected to a sinusoidal magnetic field [12].

engine.

An alternative approach is based on emulating the screw-like rotation of bacterial flagella. Examples include magnetic helical tails activated under an external magnetic field [11, 13]. The screw-like rotation of these objects triggered by rotating magnetic field breaks time reversal symmetry and induces the propulsion. Fig.1.5(b) shows an helical ribbon equipped with a soft magnetic head, whereas a similar device can be also fabricated growing a twisty silica layer half-coated with a ferromagnetic material (Fig.1.5(c)). Finally, Fig.1.5(d) displays a further example, shape-wise different from the ones above but conceptually very related. Two DNA-bounded paramagnetic beads, with different size, hereby rotates when subjected to a sinusoidal magnetic field parallel to the glass substrate beneath [12].

All the example presented in this Section fall into the category of magnetic artificial microswimmers since, although their shape recalls the natural design of bacterial flagella (or cilia), an external magnetic field is needed to actuate the motion. A second class of manmade propelled will be presented in detail in the next Chapter.

1.4   Drug delivery applications

As described in §1.3, several artificial propulsive mechanisms can be devised in order to assemble autonomous micro-robots. Further driving strategies will be also introduced throughout the manuscript.

During the past decade, the interests around these self-powered systems grew exponentially: they in fact are not only handy models to study and clone the more complex behavior of biological microswimmers [14], but they also represent the first attempt to address the challenge of micro and nano cargo's delivery [15].

Concerning the former, the motion of self-propelled objects resembles the active trajectories typical of biological swimmers. This active motion, characterized by both a ballistic and a random term (the propulsion and the reorientation, respectively), contains a remarkable amount of novel features that attracted the physics community alike (see Chapter 3). Hence, the importance of relying upon simplified experimental systems has certainly attracted the interest of a broad audience.

From a more practical point of view, self-powered micro and nano devices are a considerable breakthrough in the field of drug delivery. In fact, researchers became recently very interested in engineering micro-transporters that are able to carry micro and nano cargos throughout small capillaries, e.g., human vessels or microfluidic circuits, without the need of external driving fields. A success in this sense would have a huge impact over the pharmaceutical industry since a particular drug could be selectively driven to a specific cellular target [16].

At the moment, the road to entirely fulfill this goal appears impervious and poorly explored. In order to target a specific cell we indeed need to address the following basic requirements:

- The swimmer should be able to navigate in three dimensions and to track down the cargos floating in the liquid.

- The swimmer should be able to pick-up only the desired cargo, i.e., the transporter-cargo link should be selective.

- The swimmer should be able to deliver the cargo to a precise location.

- The drop-off should occur in the proximity of the target.

Even though substantial developments are still needed to achieve the listed goals, some noteworthy steps forward have been recently made. For instance, it has been demonstrated that $Pt-Au$ phoretic rod-like swimmers[2] can collect and drag a cargo, provided that the surface of the two "actors" are coated properly [17, 18]. A first alternative, shown in Fig.1.6(a), consists in exploiting an electrostatic bond between charged polystyrene particles and a negatively charged segment of the rod [17]. Other attachment methods rely on chemical bonds, e.g., the streptadivin-biotin interaction shown in Fig.1.6(b) [17], or magnetic forces [18]. Magnetic swimmers can be then

---

[2]For details about the propulsion mechanism that powers the so-called "phoretic microswimmers", see Chapter 2.
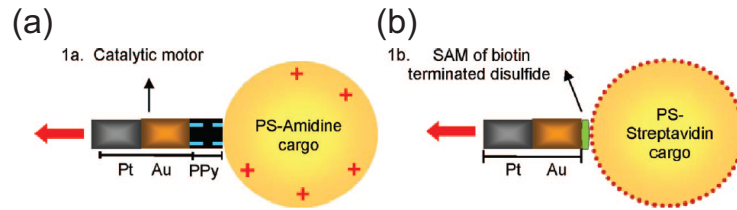
Figure 1.6: Experimental methods used to attach a polystyrene cargo to a self-propelled $Pt-Au$ rod [17]. (a) Electrostatic interaction. (b) Strepradivin-biotin bond.

guided with an external fields through microchannels, fabricated using soft lithography techniques [12, 18]. In conclusion, although the delivery requirements listed above are far to be entirely fulfilled, artificial micro-motors certainly are an appealing tool to tackle drug delivery issues.

Chapter 2

Phoretic Swimmers

As extensively discussed in §1, breaking time reversal symmetry is fundamental to achieve self-propulsion at the micrometric scale. The more intuitive way to do so consists in employing asymmetric motors, e.g., helical belts, yielding a non-reciprocal motion.

Nevertheless, the symmetry break can be also obtained without the need of such complicated geometries. A clever alternative is based on the modification of the physical properties of the surrounding medium. It is indeed well established that classical spherical colloids experience a phoretic force when dispersed in a fluid with an heterogeneous distribution of physical or chemical properties. This driving phoretic force may be, for instance, due to either a temperature (*thermophoresis*) or a chemical (*diffusiophoresis*) gradient. Of course, to have an internal propulsion, the gradient has to be triggered by the particle itself. For this reason, this type of swimmers are often addressed as *self-propelled phoretic particles*.

In this Chapter, I will first cover the basic features of phoretic forces: in particular, I will discuss their origin, which is ascribed to the interaction between the particle's surface and the molecules of the liquid. Chronologically, the first discovered phoretic phenomenon was *electrophoresis*: colloids have been hereby observed to be driven by an applied electric field when dispersed in an electrolyte solution. Later, phoretic forces have been found also in uncharged solution, thanks to the presence of chemical or temperature distributions.

The second part of the Chapter will be instead focused on self-phoretic phenomena, where the colloids are able to create their own local gradient. In order to interact asymmetrically with their surrounding, these particles have to show some kind of surface pattern, e.g., an hemisphere made of a different material. I will discuss how these so-called Janus or patchy particles propel themselves inside different media, providing very recent experimental examples of this phoretic propulsion.

2.1   The origin of phoretic forces

The origin of phoretic phenomena has been very controversial and is yet not totally understood. Micro- and nano-metric objects, suspended in a fluid, have been often observed to drift up or down a gradient such as a solute distribution. This motion recalls what would happen in the presence of an external force field, e.g., a magnetic force. However, during a phoretic migration, no net force is applied and the drift is purely a non-equilibrium effect.

The first experimental observation of phoretic migration is dated 1807, when Ferdinand Frederic Reuss found out that clay particles floating in common water respond to a constant electric field with a net motion [19]. Surprisingly, no force was effectively acting on the clay particles owing to the electrostatic screening and the motion was merely caused by the rearrangement of the water ions. The discovery of this phenomenon, nowadays well-known as *electrophoresis*, encouraged scientists to develop tons of useful applications for industrial or biological systems. For example, electrophoresis was used to sort proteins [20] or DNA/RNA mixtures [21] according to their size and mobility. Other applications include electrodialysis techniques, immunology, capillary science [21, 22] and so forth.

During the second half of the past century, numerical simulations, followed by experimental works [23, 24, 25, 26, 27, 28], demonstrated that migrations can occur even in uncharged inhomogeneous solution such as gradients of nonelectrolytes. This phenomenon is usually named as *diffusio-phoresis* or *chemophoresis*[1].

Moreover, micro-metric particles have been also shown to drift in homogeneous fluids, e.g., water, provided that a temperature gradient is present. This effect, called *thermophoresis*, was discovered by the physiologist Carl Ludwig who witnessed that the diffusion of salt in water is affected by a temperature gradient [29]. A theoretical explanation for this phenomenon was then given by Charles Soret in 1879 [30]. Nevertheless, in spite of all the additional theoretical efforts during the last century, the literature still lacks a self-standing predictive model for the thermophoretic drift of microparticles in a liquid.

What is the reason for all these phoretic migrations then? In 1989, J. L. Anderson wrote an outstanding review [31] in which he analyzed the universality of the three "out of equilibrium" effects presented above. Phoretic forces come into play under non-equilibrium conditions and when interfacial phenomena become important.

---

[1]The nomenclature is confusing. Some people define "diffusiophoresis" the bare migration in a nonionic solution, whilst others prefer to use the word "chemophoresis" for that. In the latter case, the definition of "diffusiophoresis" embraces the motion both in electrolytes ("electrophoresis") and nonelectrolytes solutions.
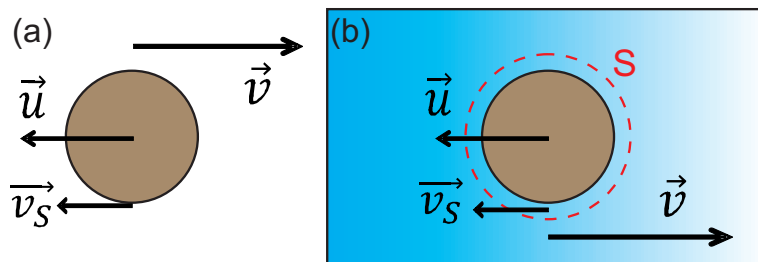
Figure 2.1: (a) Velocities balance upon "no-slip" boundary conditions at the interface particle-solvent. (a) Cartoon explaining the origin of phoretic forces. The interaction between the colloidal surface and the surrounding liquid within a small interfacial layer S leads to an apparent slip velocity v_s. v_s is globally larger than zero if the fluid is inhomogeneous as though in a gradient $\nabla\phi$.

In fields like fluid dynamics, the interface between two phase, e.g., a colloid and its surrounding medium, is often considered irrelevant; a "no slip" boundary condition is usually used to tackle, mathematically or numerically, the Navier-Stokes equation. In this case, the velocity of the particle $\overrightarrow{u}$, induced for instance by an external field, is equal to the counterflow $\overrightarrow{v}$. However, when the "no-slip" condition fails at the boundary between the particle and the fluid, the velocities balance (see also Fig.2.1(a)) needs to include an additional term $\overrightarrow{v_s}$ that embodies the slip, i.e.

$$\overrightarrow{u} + \overrightarrow{v_s} = \overrightarrow{v}. \tag{2.1}$$

Eq. (2.1) implies that a motion is possible even if $\overrightarrow{u} = 0$ as in the absence of external forces.

The interface particle-solvent plays a crucial role in dynamical effects such as *phoresis*. The surface and the liquid hereby interact within a small but finite (few nm) interfacial layer S schematically drawn (not in scale) with the red dashed line in Fig.2.1(b). Nevertheless, if the surrounding were homogeneous the mean force acting on the particle because of this interaction would be zero due to the isotropy. Instead, when the interface is characterized by an asymmetric particle-solvent interaction over the particle's surface, e.g., if a surrounding gradient is imposed (Fig.2.1(b)), a global effective force comes into play. From the point of view of a micron-sized particle, this global interaction acts like an *apparent slip velocity* $\overrightarrow{v_s}$ as shown in Fig.2.1(a). In the presence of an applied field gradient $\nabla\phi$, $\overrightarrow{v_s}$ is therefore larger than zero inducing the so-called a phoretic drift.

As mentioned before, a phoretic migration has been observed under an electrical potential, a temperature field or a solute concentration in the fluid; these phenomena are linear, therefore the phoretic-induced velocity has to be proportional to the gradient of the external field, i.e.:
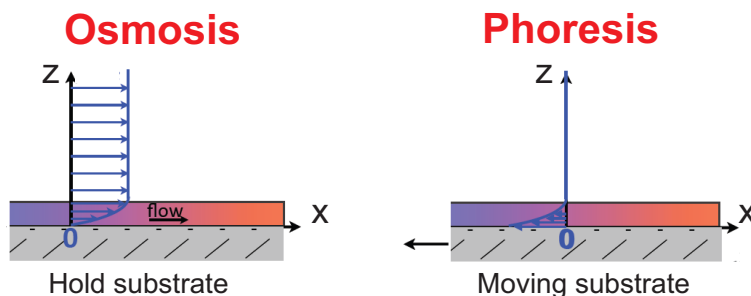
Figure 2.2: A schematic representation of the induced flow field during *osmosis* (left) and *phoresis* (right).

$$v_{phoretic} = \mu \nabla \phi \tag{2.2}$$

where μ stands for the *phoretic mobility* of the particle.

In conclusion, the origin of phoretic drift is conceptually very different from any other force-driven motion. During any phoretic migration no net force is applied and the driving is purely due to an additional hydrodynamic effect, i.e., the appearance of a slip velocity[2].

This model, based on the appearance of a slip velocity, is also helpful to explain osmotic phenomena, e.g., electroosmosis [34, 35] or diffusioosmosis [36, 37], in the presence of an external gradient. Osmotic flows generate when the solid phase is fixed in contrast with phoresis where the suspended particle is free to move. The different boundary conditions affect the flow field as shown in Fig.2.2: the anchoring of the substrate induces a flow both inside and outside the interfacial region since a continuity of the stress has to be fulfilled. On the other hand, when the particle is allowed to move towards favorite areas the fluid within the interface "follows" the motion and swiftly decays to zero outside.

From now on, I will address exclusively the phoretic motion of rigid particles suspended in a fluid under an applied field. In particular, I will focus on how Eq.(2.2) reads in the three specific cases mentioned so far: electrophoresis, diffusiophoresis and thermophoresis. Of course, these three situation differ in terms of the type of external field as well as in terms of particle-solvent interaction. After a description of the three effects I will sum up and compare their main features.

---

[2]An alternative but essentially equivalent description considers a variation of *surface tension* across the interface [32, 33]. In these models a generic phoretic drift can be written as $v_s = -l\nabla\gamma/\eta$, where l is the typical length-scale of the interfacial layer. Although all the phoretic effects can be made to collapse onto this description, I personally find it rather overblown since the rich variety of particle-solvent interactions is dumped into one very generic parameter (the interfacial tension).

2.1.1 Electrophoresis

Amongst the phoretic phenomena introduced so far, *electrophoresis* is the more straightforward and definitely the better understood. Let us consider a colloid immersed in an ionic solution as shown in Fig.2.3(a). Due to chemical absorbtion, the composition of the colloidal surface is altered by the presence of electrolytes in its vicinity, resulting in a net surface charge (positive or negative). As a consequence, the charged colloidal surface attracts a tiny layer of counterions (Stern layer) followed by a larger diffuse region where the concentration decays slowly to the bulk value, i.e., to the equilibrium between positive and negative ions. The strength of this interaction can be extracted analytically from the Poisson-Boltzmann equation for the excess charge density; under the assumption of weakly charged electrolytes [38], the potential $\psi(r)$ was shown to obey the following exponential law (see also inset of Fig.2.3(a)):

$$\psi(r) = \psi(0)e^{-kr} \tag{2.3}$$

where r is the distance from the colloidal surface and $\psi(0)$ is the surface potential. The thickness of this double shell, also called *electric double layer*, is conventionally given by the inverse of the coefficient k:

$$k^{-1} = \left(\frac{\varepsilon k_B T}{e^2 \sum c_i z_i^2} \right)^{1/2}. \tag{2.4}$$

k^{-1} is called *Debye screening length* and depends on the properties of the solution, i.e., the permittivity ε and the concentration (and valence) of ions $c_i z_i^2$. The thickness of this layer can vary from few up to hundreds nm and the potential corresponding to the Debye length is known as *Zeta potential*.

The ionic cloud provides an electrostatic screen around the colloid, i.e., if an electric field $\overrightarrow{E}$ is applied the colloids behave as they were uncharged. Therefore, according to the simple Coulombic description, no net motion is expected. On the other hand, the electrolytes are either attracted or repelled by $\overrightarrow{E}$ depending on their charge.

Anyways, the electric double layer acts as a finite interface, where the colloid still interacts electrostatically with the ions of the medium. Therefore, when the ions belonging to the double layer are dragged by the external field, this force propagates all the way to the colloidal surface. In other words, the Coulomb force is only exerted on the ion, but it gets anyways transferred to the colloid because of the ions-particle interaction within the finite interface. This force, often called *retardation force* because of its indirect nature, is responsible of the phoretic migration. With this qualitative picture in mind, the colloid can be represented as a rigid bead equipped with a slip velocity that is actuated by the retardation (or phoretic) force as shown in Fig.2.3(b).
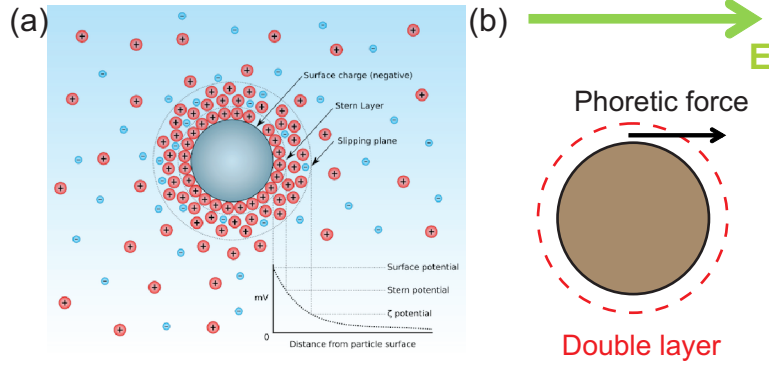
Figure 2.3: (a) Electrical double layer model for a colloid in an electrolyte solution (picture taken from http://www.zetawest.com/science.html). The inset shows the interaction potential related to the excessive charge in the double layer. (b) Schematic representation of the electrophoretic force, aka retardation force. An effective force is exerted only on the ions contained in the double layer and is transferred to the colloid through the interaction potential.

Of course the electrophoretic migration can be investigated on a more quantitative level in order to come up an expression for the phoretic mobility. A first simplified model was developed in 1903 by Smoluchowsky [39, 40] and is based on the assumption of point-like ions. When an electric field is applied across the channel, the velocity profile inside the finite interface can be calculated by solving the Stokes equation (2.5)[3]

$$\eta \nabla^2 v + \rho_e E_\infty = 0 \qquad (2.5)$$

coupled with the following Poisson relation for the charge density inside the double layer:

$$\rho_e = -\frac{\varepsilon}{4\pi} \nabla^2 \psi \qquad (2.6)$$

.

Under the hypothesis that the radius R of the colloid is much larger than the Debye length, the resulting slip velocity, defined at infinite distance from the particle, reads as:

$$v_s = -\frac{\varepsilon \zeta}{4\pi \eta} E_\infty \qquad (2.7)$$

where ζ is the zeta potential introduced above and E_∞ is the unperturbed external electric field. This result underlines two important conclusions:

---

[3]Note that the pressure gradient is considered negligible in the limit of point-like objects.

- The slip velocity and, thus, the phoretic force increase linearly with the external field, as already mentioned during the general description of phoretic phenomena.

- Depending on the sign of the zeta potential, i.e., depending on the surface charge of the particle, the colloid moves either in the direction of the electric field or in the opposite direction.

- The pre-factor $(\varepsilon\zeta)/(4\pi\eta)$ stands for the *electrophoretic mobility* of the particle and is independent of its size.

Of course, during the years, more refined theories have been developed in order to get rid of some of the above-listed assumptions [41, 28, 31]. For instance, O'Brien and White computed the electrophoretic mobility also for ranges of k^{-1} and R where the Smoluchowsky's formula does no longer hold [42]. However these models are far beyond the take-home message of this paragraph.

2.1.2   Diffusiophoresis

In the former Section the ions dispersed in the solution have been always addressed as point-like charges. The phoretic mobility was thereby induced by the pure electrostatic interactions occurring throughout the finite interface, i.e., the electric double layer. Nevertheless, the distribution of an hypothetical solute around a colloid may also affect the phoretic mobility. This effect is known as *diffusiophoresis* and happens when gradients of charged or uncharged solutes surround a particle. Even though solutes often have a charge as in the case of ionic solution, for the sake of clarity, I will first focus on diffusiophoretic phenomena caused by uncharged solutes in order to highlight additional interactions, other than electrostatic. For completeness, I will then briefly mention the complex situation where diffusiophoresis is superimposed to electrophoresis in electrolytes solutions.

A colloid always interacts with the compounds of a surrounding neutral solution mainly through van der Waals forces. This interaction is short-ranged, i.e., it occurrs within a tiny, but finite, interface called *adsorption layer* [43, 31]. Its strength is given by the *binding energy* of the adsorbed species with respect to the colloidal substrate, i.e., the interaction is weak if the components of the fluid "do not like" the colloidal surface and *vice versa*. A *potential of mean force* ϕ, that decays with the distance from the colloidal surface, is generally associated to this energy value. In analogy with electrophoretic phenomena, a force applied to a solute floating at the edge of the interface propagates to the solid surface of the colloid through the van der Waals potential.

Let us consider a colloid fluctuating in a solution characterized by a gradient of a given solute in the x-direction, as shown in Fig.2.4. For simplicity

18
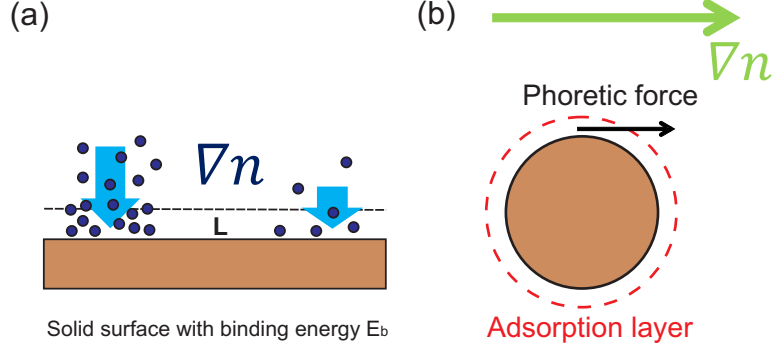
Figure 2.4: (a) Sketch explaining the origin of osmotic pressure differences across a solid substrate in an external concentration gradient. The gradient is illustrated with small blue beads. (a) Schematic representation of the phoretic force acting on the adsorption layer.

the colloidal surface is drawn as it were flat. The presence of a solute concentration gradient, schematically represented with the small blue beads, carries along a difference in osmotic pressure, given by [36]:

$$\nabla P = k_B T (n - n_0) = k_B T \nabla n, \tag{2.8}$$

where n_0 is the bulk concentration.

The osmotic pressure drop (2.9) is usually equilibrated in bulk according to the following pressure balance:

$$P - k_B T n = P_0 - k_B T n_0 \tag{2.9}$$

However, near the surface the pressure gradient (2.9) generates a force that is conveyed all the way to physical substrate via the potential of mean force. The macroscopic effect is identical to the one observed in the electrophoretic case, with the emergence of an apparent slip velocity due to retardation (phoretic) forces at the interface (see Fig.2.4(b)).

Once the type of colloid-fluid interaction is understood, the *diffusiophoretic mobility* can be easily derived [31]. The concentration of solute obeys the Boltzmann distribution, i.e.,

$$n = n_0 e^{-\frac{\phi}{k_B T}}, \tag{2.10}$$

where ϕ is again the potential of mean force, mostly related to van der Waals interaction between the solute and the colloid. Plugging this expression into the Stokes equation, it is possible to extract the velocity profile at the interface and, thus, the slip velocity:

$$v_s = -\frac{k_B T}{\eta} K L^* \nabla n \tag{2.11}$$

where K is the adsorption length and L^* is the first moment of the solute distribution at the interface. Therefore, both K and L^* entirely depend on the interfacial potential (the potential of mean force) and are known if and only if the solute profile is totally traceable.

In conclusion, in tight analogy with the electrophoretic migrations:

- The slip velocity and, consequently, the phoretic force increase linearly with the external field, i.e., with the solute concentration gradient

- The diffusiophoretic mobility is given by $(k_B T K L^*)/\eta$ and, since L^* can be either positive or negative depending on the energy profile, the phoretic motion can go after or against ∇n.

Finally, the whole scenario becomes very complicated when the solutes are actually electrolytes [26, 28, 27]. Alongside an extremely elaborated interfacial potential, additional electrophoretic effects hereby appear due to the electric field associated with the different diffusion coefficients of the ions. Hence, predicting the phoretic mobility becomes very challenging and does not particularly concerns the objectives of this manuscript.

2.1.3   Thermophoresis

The last phoretic phenomenon is called *thermophoresis* or *Soret effect* and has been receiving a large attention among theoreticians and experimentalists during the past years. Despite this, a self-consistent predictive model is still lacking.

Thermophoresis, i.e., the drift of particles inside temperature gradients, is strictly related to the above-discussed diffusiophoresis, even though thermophoretic effects are often considered negligible in the absence of steep temperature slopes. Nonetheless, the interaction between a colloid and the surrounding solvent/solutes remain the key-ingredient and is mandatory to achieve a migration. Without this interaction, no phoretic drift will be indeed observed, even if $\nabla T \neq 0$. Therefore, the thickness of the interfacial layer, i.e., the region where the interaction solvent-colloid plays a role, is reasonably assumed to be the same as for diffusiophoretic phenomena.

When we consider a colloid in a liquid characterized by a temperature gradient along the x-direction (see Fig.2.5), the thermodynamic heterogeneity of the solvent contained in the finite interface provides an apparent slip velocity and, thus, a phoretic force acting on the colloidal surface. The propagation of the phoretic "kick" from the edge of the interface to the physical surface of the colloid follows the same mechanism illustrated for electrophoresis and diffusiophoresis.

The theoretical background behind thermophoretic effects is based on the principles of non-equilibrium thermodynamics. In short, due to the
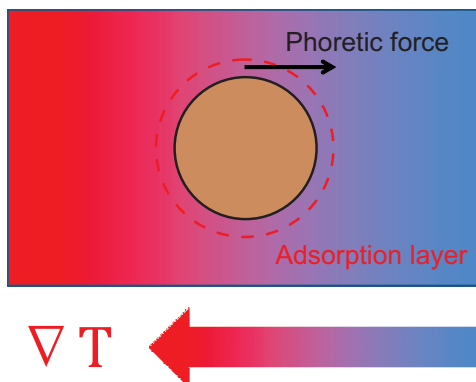
Figure 2.5: Schematic representation of the thermophoretic (or Soret) effect. A colloid in a temperature gradient experiences a phoretic force acting at the interface.

Osnager's reciprocal theorem, a heat flow is always associated with a momentum flux [44]. Using this momentum flux, it is possible to derive a theoretical expression for the slip velocity [31, 24].

$$v_s = -\frac{2H^e}{\eta T}\nabla T \tag{2.12}$$

where H^e indicates the first moment for the excess entalphy at the interface and is therefore calculated integrating over the whole interfacial layer. In analogy with diffusiophoretic and electrophoretic migrations, the thermophoretic mobility is given by $(2H^e)/(\eta T)$.

Nevertheless, the determination of the coefficient H^e is experimentally an herculean task. For this reason, the thermophoretic problem has been tackled from another point of view, i.e., considering a suspension of several particles and motoring the concentration profile, e.g., through microscopy or scattering techniques, when a linear temperature gradient is applied. This approach allows to write the following steady-state equation (2.13) for the density distribution [45]:

$$\frac{dn}{dx} = -n S_T \frac{dT}{dx}, \tag{2.13}$$

valid as long as the temperature gradient is linear along the x-axis. The equality (2.13) defines the so-called Soret coefficient, which is conventionally positive when the colloid drifts to the cold. For a fixed colloids/solvent system, knowing the applied temperature profile and measuring the corresponding concentrations, the Soret coefficient can be experimentally extracted [46, 47, 48, 49]. In case of common mixtures, S_T is only of the order of 10^{-3} K^{-1}, confirming that the Soret effect is relatively small [45]. The general trend suggests that colloidal systems usually migrate towards the cold side, i.e., the Soret coefficient is positive. However this statement is far

from being the universal truth as it has been observed that some suspensions can show a crossover to a negative S_T increasing the temperature [50].

To recap, the phoretic slip velocity is a consequence of non-equilibrium effects happening in a tiny but finite interfacial region. Under the reasonable assumption of linearity, the phoretic speed is proportional to the field gradient (see Eq.(2.2)) where the pre-factor is the so-called phoretic mobility μ. The phoretic mobilty condenses the type and the strength of the particle-solvent interaction and, in particular, determines the direction of motion. The formulae to extract μ in case of electrophoresic, diffusiophoretic and thermophoretic are compared in the following Table.

	External Field Gradient	Phoretic Mobility
Electrophoresis	E	$(\varepsilon\zeta)/(4\pi\eta)$
Diffusiophoresis (non-ionic)	∇n	$(k_B T K L^*)/\eta$
Thermophoresis	∇T	$(2H^e)/(\eta T)$

Table 2.1: Mobility coefficients for the three phoretic migrations.

2.2 Swimmers self-propelled by phoretic effects

As described in §2.1, when surrounded by an non-uniform environment, colloids feel a phoretic force that acts on the fluid-solid interface as an effective slip velocity. Therefore, even though *de facto* no external force accompanies the motion, the symmetry break, due to, for example, a concentration or a temperature gradient, is enough to provide the particle with a directed propulsion.

Self-propelled phoretic swimmers exploit this effect to navigate in a liquid at low Reynolds number. In particular, to be defined "self-propelled", these particles need to manage and modify independently as well as locally the properties of the fluid. Therefore, in contrast with the situations reported in §2.1, gradients are hereby only local and move together with the particle (see sketches in Fig.2.6(a)).

In order to create neighboring gradients, the colloids have to be equipped with some sort of surface asymmetry to differently interact with the fluid and, thus, generate inhomogeneities. The theoretical example shown in Fig.2.6(b) is very instructive and helpful to understand the mechanism [51]. Golestanian and coworkers modelled an hypothetical self-propelled device made of a colloid supplied with a an enzymatic patch. This enzymatic side is supposed to promote a chemical reaction in its vicinity and, in this way, to generate an excess of product particles which are schematically drawn in Fig.2.6(b) as small blue beads. As a consequence an asymmetric distribu-
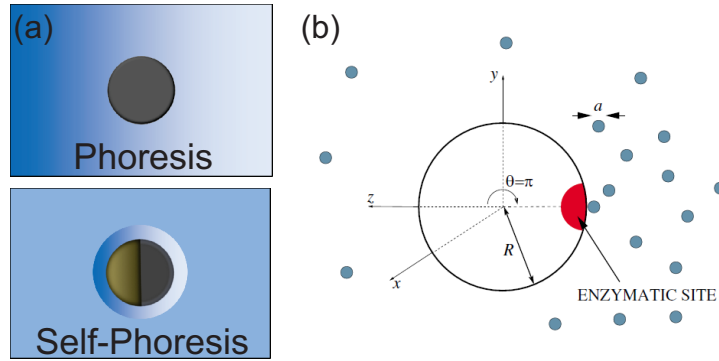
Figure 2.6: (a) Cartoon explaining the qualitative difference between phoresis and self-phoresis. (b) The Golestanian's swimmer. The device is driven by self-diffusiophoresis [51].

tion of product particles characterizes the area where the catalytic reaction is taking place. The solute concentration gradient, self-generated by the particle, triggers a phoretic motion of the colloids as extensively discussed in §2.1. Under the hypothesis that the product particles are non-ionic, this motion is utterly induced by the *diffusiophoretic* forces that act within the adsorption layer mainly because of osmotic pressure.

Colloids possessing a spotted surface are generally addressed as *patchy particles* and are indeed suitable tools to design micro-devices propelled by phoretic effects. If the patch covers half of the particle's surface, colloids are alternatively defined as *Janus*[4]. The way these particles achieve the propulsion is in line with Golestanian's model, although complicated by additional experimental peculiarities. Within the rest of this Section, I will introduce some techniques used to fabricate patchy colloids as well as few experimental systems of patchy particles phoretically self-propelled. Although the goal is certainly not to cover the whole literature of Janus and patchy colloids, these examples will help the reader to get familiar with phoretic microswimmers, as the systems employed in this work is based on a similar propulsive mechanism.

2.2.1   Fabrication of patchy and Janus colloids

During his Nobel Prize speech in 1991, P.-G. de Gennes proposed for the first time the realization of colloids with a different chemical functionalization on two hemispheres [52]. Starting from this lecture the concept of "Janus particle" spread rapidly in the field of theoretical and experimental colloidal physics, insomuch as, from a simple albeit far-sighted idea, we face nowa-

---

[4]Janus was the Roman God of beginnings and transitions, usually portrayed with two faces, looking at the past and at the future, respectively.
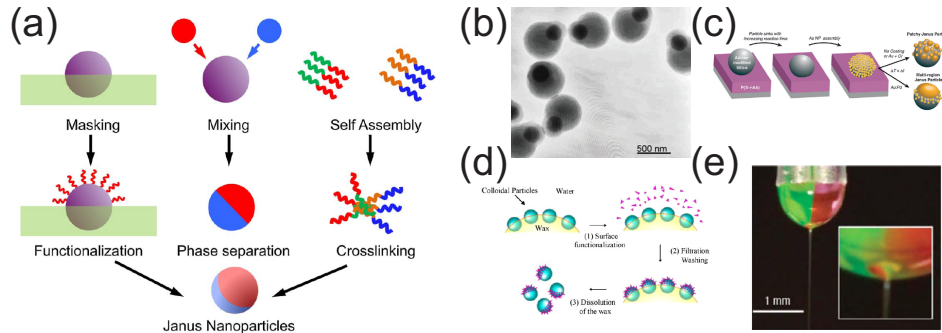
Figure 2.7: (a) Main strategies used to fabricate patchy colloids [63]. (b) Self-assembly: $Ps-SiO_2$ dumbbells obtained *via* assembly and subsequent growing [64, 65]. (c) Masking: patchy colloids prepared by linking gold nanoparticles onto one hemisphere of an embedded colloid. [66, 65]. (d) Masking: fabrication of patchy colloids through controlled Pickering emulsions of wax droplets in water [67]. (d) Phase separation: biphasic particles engineered through microfluidic jetting of two non-miscible phases [68, 63].

days a real mass production of such heterogeneous colloids. Although Janus particles are used in this manuscript as micro-motors, the broad interest around these novel colloids was initially motivated by self-assembly goals. In fact, the use of microparticles with an anisotropic interaction as building blocks leads to the assembly of material with fascinating new properties [53, 54, 55, 56, 57]. Thanks to the development of more and more powerful computational algorithms, the particle-particle interaction as well as the phase behavior of dense suspension of patchy colloids have been also extensively studied during the past years, enlightening novel structural features [58, 59, 60, 61, 62].

The preparation of Janus and patchy particles aims to fulfill some basic requirements [52]: first and foremost, the accuracy regarding the degree of coverage has to be as high as possible to guarantee the full understanding of the particle's behavior. At the same time, high density studies require a production of large numbers of particles. The techniques recently developed to address these needs can be essentially grouped in three categories [63]: self-assembly, masking and phase separation (see Fig.2.7(a)).

Self-assembly techniques rely either on the creation of block copolymers or on other types of chemical bonds. To pursue this strategy an excellent knowledge of chemistry is essential. Fig.2.7(b) shows, for instance, some $Ps-SiO_2$ dumbbells realized by growing polymer beads after tethering SiO_2 particles to a monomer through acid-base interactions [64, 65]. Alternative linking methods are largely available in literature and a detailed list can be found in Refs. [65, 63].

A second approach is based on functionalizing selectively one side of the

colloidal surface by masking (or shadowing) the other side. Deposition, evaporation and sputtering are definitely the most widely-used methods amongst this category. Homogeneous colloidal beads are hereby dried on top of a flat surface and the obtained substrate is then coated, e.g., with metallic vapors, in high vacuum chambers. The spherical shape of the colloids provides automatically the desired shadow; as a consequence, the degree of coverage can be easily tuned by tweaking the angle between the substrate and the stream of material that is being deposited. Combining masking and self-assembly schemes, it is also possible to link nanoparticles to a selected area of the colloid (see Fig.2.7(c)) provided that the particle is partially sunk into a soft material [66, 65]. Despite the handiness of the above-mentioned methods, the use of planar solid substrates restricts the number of colloids that can be coated during one single process. It is trivial to understand that a monolayer of particles is strictly needed. To overcome this problem and move towards the fabrication through masking of very large quantities of Janus particles, S. Granick and his group recently developed a novel masking method based on the concept of Pickering emulsions [52, 69]. In short, microparticles are trapped at the interface of a wax/water emulsion, preventing the droplets to coalesce[5]. The degree of sinking can be easily controlled according to the Young's law. Once the colloids seat at the wax-water interface, the outer region is functionalized by, e.g., adding additives to the continuous phase as shown in Fig.2.7(d). Compared to deposition on planar surfaces, the spherical geometry hereby increases tremendously the interfacial areas and, therefore, the amount of producible patchy particles.

Another method to fabricate *in situ* heterogeneous colloids consists in combining two immiscible components. A typical example is illustrated in Fig.2.7(e) [68]: two immiscible polymer solutions are thermally cross-linked after electrodynamic jetting through micro-capillaries. In Fig.2.7(e) one solution is labelled with a dye to demonstrate the effectiveness of this building procedure.

2.2.2 Examples of self-phoretic swimmers

As mentioned before, despite the appealing topic of self-assembly, this thesis will be focused on employing Janus and patchy particles as self-propelling engines rather than as building blocks. I have also stressed enough that breaking the symmetry of the surrounding fluid is crucial to raise phoretic forces and achieve, thus, an effective propulsion. The Golestanian's swimmer, shown in Fig.2.6(b), clarifies how a patch, that chemically interacts with the fluid, could provide non-homogeneous environmental features. Following this paradigmatic example, a reaction rate between patches and fluid

---

[5]This kind of stabilization of emulsion through particles is well know in literature as *Pickering emulsions* and credits the scientist who first described the phenomenon [70]
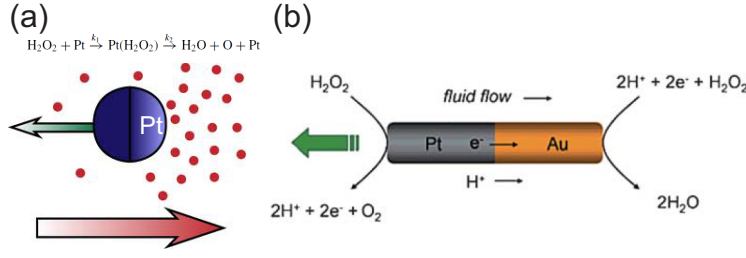
Figure 2.8: Catalytic swimmers. (a) Decomposition of H_2O_2 nearby the Pt coating (cartoon taken from Ref.[15]). (b) Redox reaction across a $Pt - Au$ rod suspended in an hydrogen peroxide solution [15].

can be also realized experimentally.

The catalytic decomposition of hydrogen peroxide is, with no doubt, the most exploited chemical reaction to device successful phoretic microswimmers. The effectiveness of this driving mechanisms has been demonstrated on particles with diverse shapes and coatings [15, 71]. Nonetheless, the simplest example involves commercial spherical colloids half-coated with Pt and subsequently diluted in an aqueous solution of H_2O_2 [72, 73, 74, 75]. Purified water is used to avoid the presence of additional ions. When in contact with fluid, the Pt catalyzes the breakup of H_2O_2 according to the two steps chemical reaction (2.14) [75, 71].

$$H_2O_2 \rightarrow Pt(H_2O_2) \rightarrow H_2O + \frac{1}{2}O_2 + Pt \qquad (2.14)$$
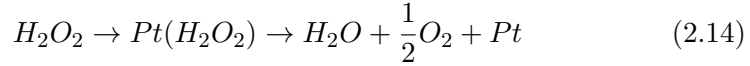
with kinetic coefficients k_1 and k_2, respectively. The chemical dismutation obviously leads to the consumption of H_2O_2 and to the production of O_2. This happens selectively close to the Pt-coated hemisphere (see sketch in Fig.2.8(a)), whilst the other side of the colloid is initially surrounded by bulk conditions, i.e., $\nabla^2[H_2O_2] = 0$ and $\nabla^2[O_2] = 0$. Of course, the situation evolves in time due to diffusion of the species. Naively, we expect the typical pure diffusiophoretic migration, where $v_s \propto \nabla[fuel]$; the pre-factor representing the phoretic mobility is theoretically only biased by the properties of the interface (see §2.1 for more details). Electrophoresis does not enter the description because no ions are present. Hence, once the fuel concentration is known, the phoretic slip velocity can be calculated using Eq. (2.12).

As a matter of fact, the fuel distribution $[fuel]$ can be precisely derived solving the reaction-diffusion of the fuels involved in the propulsion: H_2O_2 and O_2. On top of this, $[H_2O_2]$ and $[O_2]$ need to satisfy the following balance:

$$D_{hp}[H_2O_2] + D_{ox}[O_2] = D_{hp}n_\infty \qquad (2.15)$$

where D_{hp} and D_{ox} are the diffusion coefficients of the two species and n_∞ is the bulk concentration. Taking into account all these considerations,

Golestanian and coauthors solved the problem and found three characteristic regimes, depending on the reaction rates and the size R of the colloid [75]. I am going to present them only on a very qualitative level.

1. If $k_1 \gg k_2$, i.e., if the second step of (2.14) is much faster than the first, the overall reaction is controlled by the concentration of H_2O_2. If this is true, the concentration gradient ∇n of Eq. (2.12) is directly given by $[H_2O_2]$, yielding a linear increase of v_s with the concentration of hydrogen peroxide [74].

2. At high $[H_2O_2]$ the first step saturates and ∇n becomes proportional to the rate k_2 of the second reaction. The linear relation between v_s and $[H_2O_2]$ vanishes.

3. If both the reaction rates k_1 and k_2 are fast or the size R of the colloid is sufficiently large, the reaction-diffusion problem is dominated by the flux of reactants towards the Pt coating, leading to a slip velocity that scales as a $1/R$ [75].

Chronologically, Pt-coated colloids were not the first to employ the catalytic reaction as propulsion mechanism. A similar directed motion was earlier observed with bi-metallic rods dispersed in the same hydrogen peroxide solution [76, 77, 78]. In their trailbreaking work, Paxton and collaborators studied the self-propulsion of nano-rods, half made of Pt and half of Au as illustrated in Fig.2.8(b). The Pt side is still routinely used as catalyzer, although similar effects have been later reported using other metals, such as Ni [79, 80], or enzymes [81]. Very recently Palacci *et al.* demonstrated that the decomposition of H_2O_2 can be also obtained through hematite cubes upon light exposure [82].

Nonetheless, compared to the single Pt-coated particles described before (Fig.2.8(a)), the presence of a second metallic side, usually made of Au, largely complicates the scenario. In fact, as shown in Fig.2.8(b) a redox reaction takes also place, i.e., the Pt and the Au side are reduced and oxidized, respectively. This reaction proceeds with a flux of e^- inside the particle balanced with a migration of ions in the electric double layer. If we recall the notions introduced in §2.1 the flux of ions inside the interfacial region is the precondition for any sort of electrophoretic drift. Therefore, the propulsion is hereby biased not only by diffusiophoretic force but also by the interfacial electrophoretic slip.

Even though microswimmers driven by the catalytic dismutation of hydrogen peroxide are doubtless the most widely used, the past years registered the development of other types of phoretic propellers. Amongst them, it is worth to spend some words about recent advances in the fabrication of purely thermophoretic microswimmers [83, 84].
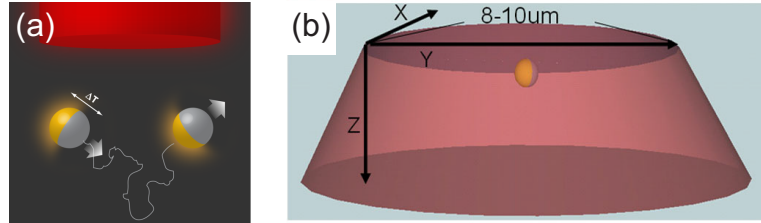
Figure 2.9: (a) Cartoon showing the motion of propellers driven by self-thermophoresis [84]. (b) Schematic illustration of the experimental method used to achieve a self-thermophoretic motion. Au coated colloids, floating in water, are illuminated by a rather focused laser beam [83].

As extensively discussed in §2.1, a directed drift can be obtained even without any gradient of chemical species as long as a temperature profile surrounds the probe (*thermophoresis*). In analogy with the examples of self-propelled particles provided above, when the temperature gradient is generated by the colloid itself, the motion is address as self-thermophoretic (see Fig.2.9(a)).

A local temperature gradient around a micrometric colloid is achievable by heating selectively a patch. M. Sano and coworkers showed that this can be done by coating one hemisphere of a spherical SiO_2 colloid with a light-absorbing material, such as gold, as schematically illustrated in Fig.2.9(b). These Janus particles are then diluted in deionized water to rule out the influence of other phoretic phenomena, alias electrophoresis and diffusio-phoresis.

Under illumination with green light, the SiO_2 side behaves as transparent whereas the Au hemisphere is heated due to absorption. The heat propagates into the fluid establishing a temperature gradient in the proximity of the colloid as nicely shown in Fig.2.9(a). The problem becomes analogous to the diffusiophoretic one, provided that we replace the diffusion equation by the heat transfer and the diffusiophoretic mobility by the Soret coefficient [84].

Nevertheless, thermophoretic migrations are always very small unless a steep temperature gradient is applied. For this reason the illuminating beam must be rather powerful (40 mW) and focused: as shown in Fig.2.9(c) the laser spots a very limited area around the particle. This prevents the investigation of large displacements, which the main drawback of the system.

Chapter 3

Active Brownian Motion

In Chapters 1 and 2 I focused the attention on how micron-sized probes, either natural or manmade, can propel themselves in a liquid. I described how internal driving forces can be achieved with particular geometrical configurations (bio-inspired microswimmers) or through the local modification of the environment (phoretic microswimmers). In both cases, self-propelled particles become equipped with a ballistic speed that constantly points in the direction of the driving force.

In this Chapter, which is partially inspired by Refs. [85, 86], I will consider the effect of a directed propulsion onto the motion of micro- or nano-metric particles. Because of their small size, such particles already possess an intrinsic motion, due to thermal fluctuations, when suspended in a liquid. This motion is well-known as Brownian diffusion and describes the agitation (both translational and rotational) of objects in equilibrium in a fluid at $T \neq 0$ K. When these thermal fluctuations are coupled with an internal ballistic propulsion, we observe a novel type of motion that naively inherits the properties of both contributions. To underline this double nature people commonly address this behavior as *Active Brownian motion.*

I will first present the features of classical Brownian diffusion, from a physical as well as from a more mathematical point of view. I will then extend the notions to the behavior of Brownian objects supplied with some sort of activity. In the latter case the literature is not as advanced as for Brownian particles; I will therefore introduce two well-established approximated models that lead to a good description of the system and, in particular, to a helpful interpretation of the experimental trajectories. Finally, I will briefly go through some basics about hydrodynamics of self-propelled particles.

3.1 Brownian motion

To acknowledge the first observation of what is nowadays called Brownian motion we need to travel back to the beginning of the 19th century. In 1827,

Robert Brown, a well-regarded Scottish botanist, reported that pollen grains with a size of few microns, while floating in water, have a motion that arises "neither from the current of the fluid, nor from its gradual evaporation, but belongs to the particle itself" [87].

It then took about 80 years until physicists started being intrigued by this phenomenon, providing some sort of explanation for it. In the beginning of 20th century, the problem was tackled almost simultaneously by two renowned scientists: Albert Einstein and Marian von Smoluchowski.

In 1905, Einstein published the first physics paper about Brownian motion [88]. He revisited the problem in terms of osmotic pressure arguing that a particle suspended in the fluid behaves as particles dissolved in it [89]. By matching osmotic pressure forces with the resistance of the fluid due to friction he ended up with his famous relation for the diffusion coefficient, i.e.

$$D_0 = \frac{kT}{m\gamma_0}, \tag{3.1}$$

where, according to Stokes' theory, $m\gamma_0 = 6\pi\eta R$, for a spherical particle with radius R immersed in a fluid of viscosity η.

During the time Einstein published his remarkable work, Smoluchowski was working on the same topic with a different point of view. He published his results [90] one year after Einstein's paper (we could refer to this as "bad timing"). Smoluchowski had a more mechanistic approach to the problem: he formulated a detailed kinetic model based on the collisions of light and heavy hard spheres that mimic the solvent and the probe, respectively. In spite of a large number of approximations, the resulting diffusion coefficient differed from (3.1) only by a factor 32/27.

3.1.1 The Langevin equation

In 1908, P. Langevin, in the attempt of overcoming Smoluchwski's approximations, found a link between Einstein's and Smoluchowski's theories [91]. Langevin's approach is very straightforward as it is based on one of the benchmarks of phyisics: the Newton's law. Because of its simplicity, his model is very pedagogical and still largely used during basic lectures about Brownian motion.

In short, if we consider a particle with mass m suspended in a fluid of viscosity η, the 1D force balance reads as follows:

$$m\frac{dv}{dt} = -\gamma_0 v + \xi(t) \tag{3.2}$$

γ_0 is again the friction coefficient and ξ is an additional force introduced to include in the description the interaction between the particle and the

molecules of the solvent. Since ξ is artificially added to Eq. (3.2), we can anchor some restrictions inspired by its fluctuating nature.

- ξ must be isotropic, i.e., $\langle \xi(t) \rangle = 0$.

- ξ is assumed to be Gaussian white noise, *ergo* it neither shows time autocorrelation for $t' \neq t$ nor is correlated with the position and the velocity of the particle, i.e.

$$\langle \xi_i(t)\xi_j(t') \rangle = \delta_{tt'}\delta_{ij} \tag{3.3}$$

$$\langle \xi(t)x(s) \rangle = 0 \tag{3.4}$$

$$\langle \xi(t)v(s) \rangle = 0 \tag{3.5}$$

The Gaussian assumption is motivated Central Limit Theorem since $\xi(t)$ is the sum of several independent forces.

Eq. (3.2) cannot be solved exactly because of the unknown force $\xi(t)$, on which only few statistical requirements have been made. However, the derivation of some averaged quantities is still possible.

In particular, applying the equipartition theorem $\langle v^2(t) \rangle = kt/m$ and taking into account the properties of $\xi(t)$ defined above, one can analytically derive the 1D mean square displacement $\langle x^2(t) \rangle$[1].

$$\langle x^2(t) \rangle = \frac{2kT}{\gamma_0}t + K \cdot e^{-\frac{\gamma_0}{m}t}. \tag{3.6}$$

where K is an integration constant. The ratio m/γ_0 is the relaxation time of the particle and, for typical situation, is orders of magnitude shorter than 1 s. Although the result (3.6) seizes even very small time scales, for practical applications, the exponential term is usually neglected[2], yielding

$$\frac{d\langle x^2(t) \rangle}{dt} = \frac{2kT}{\gamma_0} = 2D_0 \tag{3.8}$$

The generalization to the 3D case is trivial and leads to

---

[1]Even though I only report explicitly the 1D mean square displacement, the whole derivation can be easily extended to the 3D case since the equipartition theorem in 3D reads as $\langle v^2(t) \rangle = 3kt/m$.

[2]At low Re number the systems are inertia-free, so we can alternatively solve

$$0 = -\gamma v + \xi(t). \tag{3.7}$$

$$\frac{d\left\langle \mathbf{r}^2(t) \right\rangle}{dt} = 6D_0 \tag{3.9}$$

Therefore, the mean square displacement of a Brownian particle scales linearly with time and the slope of the line is directly related to the diffusion coefficient D_0 of the particle.

Finally, using the Langevin equation and similar arguments, one can also extract some information about the mean velocity. Amongst them, it is certainly worth to remark that, if the particle is initially in equilibrium, its mean velocity $\langle v(t) \rangle$ is zero for each following time step t.

3.1.2 A stochastic approach: the Fokker-Plank equation

The Langevin equation provides access to mean quantities in the $(\overrightarrow{r}, \overrightarrow{v})$ phase space. Despite the importance of these parameters, the Brownian behavior of a particle contains much more information. For instance, how do the probability distributions look like? This is key-question in statistical physics where we are usually interested in understanding the probability that a particle i at time t is in a certain position $\overrightarrow{r}$ with velocity $\overrightarrow{v}$. In order to grasp this additional knowledge, it is necessary to look deeply into the properties of the fluctuating force $\xi(t)$.

The stochastic calculus, which became popular in the beginning of the 20th century, is a powerful tool to treat non-deterministic phenomena. The random fluctuation of Brownian particles obviously belongs to this category. It is however important to remark that, although the stochastic description provides additional statistical information, the Langevin equation is still needed to identify the suitable parameters that have to be used in the stochastic calculus.

Let us review how the probability distributions $p(x, v, t)$ can be easily derived from the Fokker-Plank equation A.13[3] in the 1D[4] case of a single Brownian particles immersed in a liquid. If the systems is overdamped, the Langevin equation corresponding to such system is:

$$0 = -\gamma_0 v + \xi(t) \tag{3.10}$$

with $\dot{x} = v$. Extracting the transitions moments from A.7 and A.8, the drift and the diffusion coefficients ($b(x, v, t)$ and $\sigma(x, v, t)$, respectively) are:

$$\begin{cases} b(v) = -\gamma_0^{-1} v \\ \sigma = \frac{kT}{\gamma_0} \equiv D_0 \end{cases} \tag{3.11}$$

---

[3]Readers that wish to have a hint about the mathematical features of this equation can refer to the Appendix of this thesis.

[4]3D systems are described conceptually in the same way but the notation is tougher.

We can now rewrite the Fokker-Plank equation for the x variable alone. In this case $p(x, t)$ becomes a density distribution $\rho(x, t)$ and satisfies the following differential equation:

$$\frac{\partial \rho}{\partial t} = D_0 \frac{\partial^2 \rho}{\partial x^2}. \tag{3.12}$$

(3.12) is well-known as Fick's (or diffusion) equation and yields a Gaussian distribution of the displacements.

On the other hand, considering the Fokker-Plank equation for the whole phase space (x, v), we obtain, for the probability distribution $p(x, v, t)$:

$$\frac{\partial p}{\partial t} = \frac{\partial}{\partial v} \left(\gamma_0 v p + D \frac{\partial p}{\partial v} \right) - v \frac{\partial p}{\partial x} \tag{3.13}$$

Eq. (3.13) is known as *Kramers-Klein equation* and leads to a Maxwell distribution of the velocities.

For completeness, the scenario is only slightly more complicated when an external field $U(x)$ is present. Following identical arguments one can easily show that:

- The density distribution obeys the so-called Smoluchowski equation, i.e.

$$\frac{\partial \rho}{\partial t} + \frac{1}{\gamma_0} \frac{\partial U(x) \rho}{\partial x} = D \frac{\partial^2 \rho}{\partial x^2} \tag{3.14}$$

- $p(x, v, t)$ is distributed according to the famous Maxwell-Bolzmann statistics, i.e.

$$p(x, v) = cost \cdot e^{-\frac{U(r)}{kT}} \cdot e^{-\frac{\gamma_0 v^2}{2D_0}} \tag{3.15}$$

3.1.3   The unrestricted random walk

So far, I have discussed how some quantities (e.g., the mean displacement or the probability distributions) can be extracted using both a classical and a stochastic description of Brownian motion. But how shall we characterize the trajectories of Brownian particles?

The evolution of the positions is usually modelled using random steps of finite length in a a lattice, as displayed in Fig.3.1. This type of motion is known as *unrestricted random walk* since the reorientation angle is drawn completely at random.

Is there a mathematical way to seize the properties of these paths? The answer is yes. Just as Einstein and Smoluchowski were formulating their theories of Brownian motion, a statistician, named Karl Pearson, proposed a different approach to the problem of diffusion [92]. The Brownian particle is hereby traced as a random walker, travelling in a 1D lattice (again the 3D case is not qualitatively different) with steps of length l at times $0, \tau, 2\tau, ...$
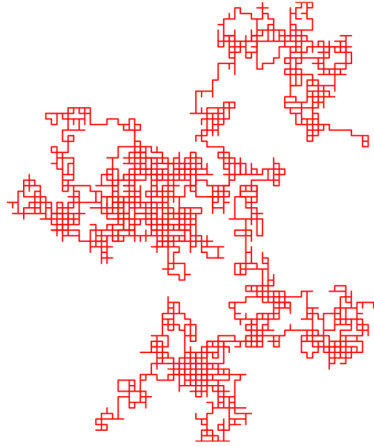
Figure 3.1: An unrestricted random walk on a 2D lattice (picture taken from Wikipedia).

The probability that the particle is at a distance ml after a time $n\tau$ is given by a binomial distribution with mean 0 and variance n, i.e.

$$p(m,n) = \frac{n!}{2^n \left(\frac{n+m}{2}\right)! \left(\frac{n-m}{2}\right)!} \tag{3.16}$$

After enough time, the probability distribution (3.16) converges to a Gaussian due to the Central Limit Theorem. In particular, it can be shown that the position of the particles becomes normally distributed with mean 0 and variance $l^2 t/\tau$ [85]. Therefore, in the continuous limit ($\tau \to 0$) and defining the diffusion coefficient D as $l^2/2\tau$, the probability distribution $p(m,n)$ satisfies the Fick's equation (3.12). In conclusion, the positional properties of a Brownian diffuser can be easily described in a purely mathematical way considering a walker that randomly reorients at each time step.

3.2   Active Brownian motion

Let us go back for a while to the system of self-propelled we wish to understand. Micrometric colloids are small enough to possess the Brownian features highlighted in §3.1 when dipped into a liquid. However, their motion cannot be oversimplified as an unrestricted random walk since an internal propulsive force always comes in play along with the classical diffusion. Hence, the motion of these active particles is way more complex...

Janus particles can be driven in (or in the opposite) direction of the coating by means of self-generated phoretic forces, as extensively described in §2.2. Because of rotational diffusion the particle's orientation and, as a consequence, the direction of the internal driving change in time. The resulting trajectory, schematically illustrated in Fig.3.2(a), shows therefore

Figure 3.2: (a) Schematic trajectory of self-propelled Janus colloids with persistence length l. (b) Sketch of a "run" and "tumble" motion with persistence length l. For *E.coli* the "runs" and the "tumbles" are achieved bundling or unbundling their flagella, respectively (see cartoons next to the trajectory). (c) Example of a persistent random search strategy on a 2D lattice [93].

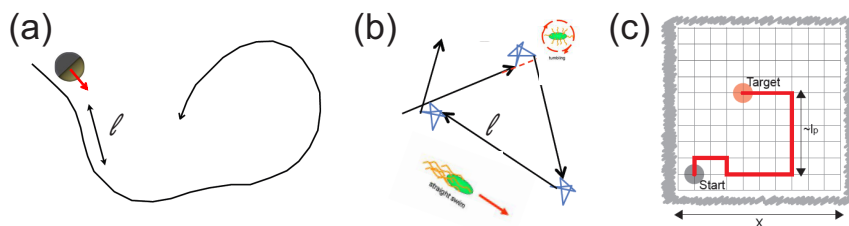a "persistence" that leads to characteristic length l of the motion. In plain words, an active particle has the tendency to keep a straight motion and this tendency is more and more pronounced the slower the colloid rotates.

The presence of a persistency characterizes also the motion of several biological organisms (bacteria and cells). "Run" and "tumble" bacteria, for instance, chase food performing persistent straight paths abruptly interrupted by random reorientations (tumbles), as previously mentioned in §1.2. The tumbling rate obviously defines the duration of the persistency (see Fig.3.2(b)). This "run" and "tumble' motion can be reproduced with self-propelled particles alike in a quasi-2D configuration: When the translational motion is constrained in 2D (for instance by glass slides) but the particle rotates freely in 3D, any driving force pointing out of the 2D plane is screened by the confinements. This results in an effective tumbling when the propulsive force happens to be perpendicular to the 2D plane.

The first attempt to incorporate a persistency into a classical "unrestricted random walk theory" gave birth to the so-called *Levy flights*. In short, the basic idea is to allow the presence of large "jumps" by drawing the spacial steps out of a long-tail exponential distribution. The resulting trajectories are thereby defined by very long segments alternated with short ones. This type of path has been extensively use to model food searching strategies of animals and microorganisms when the targets are sparse [94, 95, 96, 97].

Nevertheless, it is important to remark that this kind of walk keeps being unrestricted because reorientations still happen at random; therefore, Levy flights do **not** mimic correctly the persistency.

During an unrestricted random walk (read, Brownian motion) the position at time t is only given by the immediately previous state and the transition probability. Stochastically speaking, unrestricted random walks are Markov processes (see Appendix A for a proper definition of Markov processes). On the other hand, the active motion of self-propelled particles

and bacteria is strictly non-markovian since positions are also affected by the persistence of the orientation. In other words, whilst Brownian motion is fully uncorrelated, active trajectories show a short time correlation. For these reasons, random walk of active particles are usually addressed as *persistent (or correlated) random walks*. A typical example of correlated random search on a 2D lattice is shown in Fig.3.2(c).

Needless to say, uncorrelated random walks are mathematically far more complicated to handle and a feverish discussion is still in progress. Using numerical simulations we can partially overcome the impasse by coupling the Smoluchowski equation 3.14 with a particle's orientation that undergoes a free rotational diffusion. Hereafter, I will present an approximated model [86, 98, 99] that provides some useful information about active Brownian trajectories, e.g., mean square displacement as well as long and short time behavior, . In line with §3.1 I will discuss a physical approach first, followed by few hints regarding random walks theory.

3.2.1 The Langevin and the Fokker-Plank equations

When we write down the 2D Langevin equation (3.2) describing an active Brownian particle, an internal propulsive force needs to be added to the balance.

$$m\frac{d\mathbf{v}}{dt} = -\gamma_0 \mathbf{v} + f_{prop} + \xi(t) \tag{3.17}$$

Since the self-propelled particle takes up energy from the environment and converts it into directed motion, the contribution of the internal force can be included into drag coefficient that thereby becomes velocity-dependent, i.e.

$$m\frac{d\mathbf{v}}{dt} = -\gamma(\mathbf{v})\mathbf{v} + \xi(t) \tag{3.18}$$

This manageable approach is very powerful in its simplicity: a suitable choice for the function $\gamma(v)$ permits to seize rather variegated phenomena, where, for instance, the energy is stored (pumping) or dissipated. The main drawback is related to the fact that the choice of $\gamma(v)$ is arbitrary. To overcome this problem, Schweitzer and coworkers proposed the following general expression for $\gamma(v)$ based only on energetic observations [99]:

$$\gamma(v^2) = \gamma_0 - \frac{qd}{c + dv^2} \tag{3.19}$$

where γ_0 is the bare friction coefficient, and q, d, and c sketch the "pumping", the conversion into kinetic energy and the dissipation, respectively.

The velocity-dependent friction coefficient $\gamma(v)$ can be finally plugged into the Fokker-Plank equation (3.13) that describes the probability distribution $p(r, v, t)$, yielding

$$\frac{\partial p}{\partial t} = \frac{\partial}{\partial \mathbf{v}} \left(\gamma(\mathbf{v})\mathbf{v}p + D\frac{\partial p}{\partial \mathbf{v}} \right) - \mathbf{v}\frac{\partial p}{\partial \mathbf{r}} \qquad (3.20)$$

where D is defined in the velocity space[5]. Although general solutions can be extracted from (3.20), self-propelled colloids belong to the particular case in which the dissipation is negligible, i.e., the whole energy gets converted into kinetic motion. Under this assumption, it is possible to calculate precisely the 2D mean square displacement of the self-propelled particles in the real space [100].

$$\left\langle (r^2(t) - r^2(0) \right\rangle = 2D\tau_r^2 t + D\tau_r^3 \left[e^{-\frac{2t}{\tau_r}} - 1 \right] \qquad (3.21)$$

in which τ_r stands for the typical rotational time of the particles. Moreover, v^2 is linearly related to τ_r with a slope given by the diffusion coefficient in the velocity space, i.e., $v^2 = D\tau_r$. Moving back to the real space and considering the coupling between translation and rotation for a spherical geometry Eq. (3.21) becomes [74]:

$$\left\langle (r^2(t) - r^2(0) \right\rangle = 4D_0 t + \frac{v^2\tau_r^2}{2} \left[\frac{2t}{\tau_r} + e^{-\frac{2t}{\tau_r}} - 1 \right] \qquad (3.22)$$

with temporal limits

$$\begin{array}{ll} \left\langle (r^2(t) - r^2(0) \right\rangle = 4D_0 t + v^2 t^2 & \text{for } t \ll \tau_r \\ \left\langle (r^2(t) - r^2(0) \right\rangle = (4D_0 + v^2\tau_r)t & \text{for } t \gg \tau_r \end{array} \qquad (3.23)$$

Here D_0 is the bare diffusion coefficient in the real space. The form (3.22) of the mean square displacement describes well the particle's roaming when an internal force introduces a short time persistency. I will discuss the practical implications of (3.22) within the experimental Section of the thesis. For the time being, it is sufficient to remark that the motion of an active particle (small enough to be subjected to Brownian fluctuations) is defined by a ballistic behavior ($\left\langle (r^2(t) - r^2(0) \right\rangle \propto t^2$) at time scales short compared to its rotational diffusion. On the hand, longer times lead to a diffusive motion ($\left\langle (r^2(t) - r^2(0) \right\rangle \propto t$); comparing the second Eq. (3.23) with the classical 2D diffusive behavior where $\left\langle (r^2(t) - r^2(0) \right\rangle = 4D_0 t$ the diffusion stands out to be enhanced, i.e., an effective diffusion coefficient can be straightforwardly defined as:

$$D_{eff} = D_0 + \frac{1}{4}v^2\tau_r \qquad (3.24)$$

As side remark, it is worth to underline that Eq. (3.21) is more universal than appears: τ_r, although introduced as rotational diffusion time, indeed has the meaning of a generic reorientation rate of the particle. Therefore, Eq.

---

[5]The diffusion coefficient in the real space is simply given by D divided by γ^2.

(3.21) can be easily extended to "run" and "tumble" bacteria interpreting τ_r as a tumbling rate.

3.2.2   The persistent random walk

As shown above, the use of a velocity-depend friction is a smart technique to take into account the internal propulsions without loosing the Fokker-Plank formalism of Brownian diffusion. With this trick non-markovian process are stochastically treated as markonian.

Nonetheless, the same scaling of the mean square displacement can be obtained with a completely different approach: it consists in analyzing the random walk from a mathematical point of view in analogy with Pearson's arguments about unrestricted random walks (see §3.1.3). This way, the trajectories of active particles can be described with no need of "faking" their non-markovian nature.

As a reminder, unrestricted walks were characterized by random reorientations at each time step; in their continuous limit, they converged to the classical Fick's equation of diffusion. In contrast, when we deal with *correlated* or *persistent random walks* the orientation can be maintained for two or more time intervals. This implies that, keeping the same 1D formalism used in §3.1.3, at each time step τ_i the walkers can either change direction with probability $\varepsilon\tau$ or keep going in the same direction with probability $1 - \varepsilon\tau$ [101]. The velocity during each step is constant and trivially equal to the ratio between the length of the jumps l and the time interval τ.

Through simple probability arguments and with a pinch of math, it can be shown that, in the continuous limit, the probability for a walker to be in the position x at time t obeys the following differential equation [85, 101].

$$\frac{\partial^2 p}{\partial t^2} + 2\varepsilon\frac{\partial p}{\partial t} = v^2\frac{\partial^2 p}{\partial x^2} \tag{3.25}$$

Eq. (3.25) is known as *Telegraph equation*[6] and it is the one to one analogous of the diffusion equation since it is derived with the same probability arguments used in §3.1.3. Therefore, remarkably, random walks theory is a simple, self-consistent and efficient mathematical tool to treat a broad variety of physical phenomena, as long as we know how an object navigates in the liquid.

Once the form of the probability distribution is deduced from (3.25), the mean square displacement follows automatically as

$$\left\langle x^2(t)\right\rangle = \int x^2 p(x,t)dx \tag{3.26}$$

---

[6]The name *Telegraph equation* has historical reasons; Eq. (3.25) was in fact formulated by W. Thomson to model the propagation of telegraph signals [102].

The solution is astonishingly in agreement with what obtained in previous Section with a totally different method. It reads as

$$\langle x^2(t) \rangle = \frac{v^2}{\varepsilon} \left(t - \frac{1}{2\varepsilon}(1 - e^{-2\varepsilon t}) \right) \qquad (3.27)$$

where $1/\varepsilon$ generalizes the role of τ_r in Eq. (3.22). Again, for times small compared to $1/\varepsilon$ the mean square displacements has an approximated quadratic behavior, whereas large ts lead to an effective diffusion.

3.3 Hydrodynamics in active suspensions

The motion of active organisms in a fluid contains striking features also from an hydrodynamic point of view. The hydrodynamics of microswimmers has been extensively studied during the last decade leading to a "sea" of phenomena that are not observable in equilibrium, such as collective behaviors or interactions with confinements [103, 104, 105, 106, 107, 108, 109, 110, 3]. Notice to motorists: A deepen analysis of all these effects could provide enough material for a further thesis; the following paragraph only includes few breadcrumbs about active matter hydrodynamics and certainly does not aim to be exhaustive.

A noteworthy model to grasp the hydrodynamics of active swimmers is based on a far field approximation [71]. A colloid driven by an external force behaves as a force monopole, i.e., its flow field scales as with the inverse of the distance r. The situation is totally different when the force is internal as for self-propelling objects.

Self-phoretic swimmers show in fact a very fast ($\sim r^{-3}$) decay of the far field surrounding flow; hydrodynamically speaking, microswimmers that possess the above-mentioned r^{-3} decay are often address as *squirmers*.

Other active organisms rather behave as force dipoles; in particular, depending whether a swimmer moves using "arms" (*puller*) or "tails" (*pusher*), the far field flow can be respectively sketched as in Fig.3.3(a) or 3.3(b). A rear propulsion is typical of microorganisms equipped with long flagella as in the case of *E. coli* bacteria, whereas ciliates usually swim with front whip-like strokes (see §1.2 for details about these swimming mechanisms).

The take-home message is that the mechanism of propulsion strongly affects the behavior of the flow field and the hydrodynamics can thus be mapped if and only if the details of the driving force are fully known.

Nevertheless, a far field approximation sometimes is not enough to grasp the entire pictures: as I will show in the experimental section, propellers can get very close to each other, at distances where higher order terms need to be take into account. Although very recent works [111] managed to map the flow in the near field, at short distances the whole scenario is additionally complicated by the appearance of lubrication forces. Luckily, under the
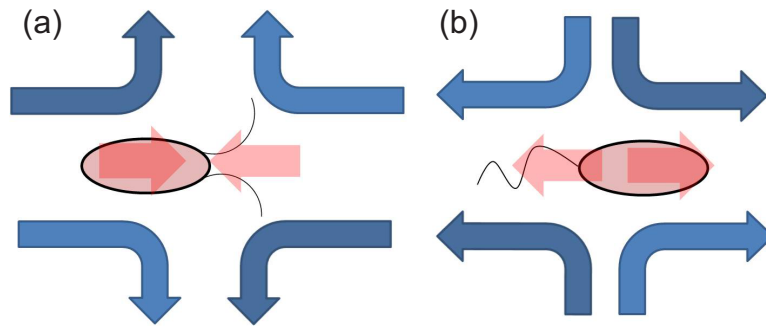
Figure 3.3: Far field hydrodynamics of (a) pullers (propelled from the front) and (b) pushers (propelled from the rear). The blue and the red arrows sketches the flow field and the force dipole, respectively.

experimental conditions that will be considered, hydrodynamics does not change dramatically the qualitative behavior of the system of self-propelled particles. In most of the experiments that I will present hydrodynamic effects are indeed proved to be negligible.

Part II

Experimental details

Chapter 4

Sample fabrication

The experimental system I will present in the following Chapters exploits a self-phoretic propulsion. Within §2.2 I've described several methods, available in the literature, to achieve a phoretic internal driving. All these techniques have in common the need of modifying asymmetrically the properties of the the particle's surrounding in order to create a gradient localized nearby the colloid. These non-homogeneities can either involve a chemical (e.g., ionic) distribution or a temperature profile.

Because of the asymmetric surface properties, Janus and patchy colloids are perfectly suitable for this goal and their fabrication has been supported by a large experimental effort during the past decades. In §2.2 I have illustrated that, choosing the right combination particle/solvent, Janus colloids can be propelled by electrophoretic, diffusiophoretic or thermophoretic forces. Although the self-propulsion mechanism used in this work has several novel features, it fits well in this background.

In this Chapter, I will introduce the ingredients that have been employed to perform the experiments. I will not focus on the propulsion, i.e., I will do nothing but listing each element that characterizes the experimental systems. In short, I am basically going to refer to three ingredients:

1. The Janus particles, i.e., silica colloids coated using evaporation methods.

2. The solvent, i.e., a binary mixture kept at the critical concentration and heated beyond its critical point.

3. The illumination which provides a selective heating onto the light-absorbing side of the colloids.

Finally, I will spend few words on how the recorded videos are analyzed; in particular, I will briefly explain how the colloids are tracked in order to reconstruct their trajectories and, therefore, to understand the properties of their motion.
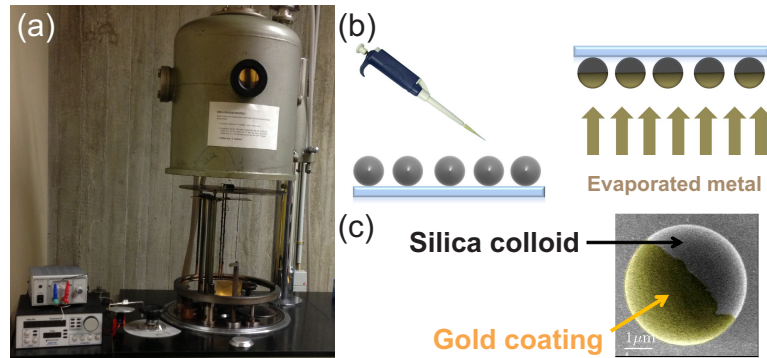
Figure 4.1: (a) The evaporation unit. (b) Cartoon of the two steps carried out during the evaporation. Left: a suspension of SiO_2 is spread on a glass slide. Right: a metallic layer is evaporated onto the exposed hemisphere. (c) A scanning electron microscopy image [115] of a colloidal particle with a 20 nm thick gold cap (highlighted).

4.1 The particles

4.1.1 Fabrication of Janus colloids via evaporation methods

In order to produce the Janus colloids that will subsequently serve as self-propelling phoretic particles we employ a standard evaporation method. This technique has been largely used in recent experiments due to its relative handiness [52, 65, 74, 72, 83, 112, 113, 114].

The protocol is rather straightforward: homogeneous SiO_2 colloids, purchased in aqueous solution from Microparticles GmbH, are poured on top of a glass substrate as shown in Fig.4.1(b) (left).

After drying, the slide is place upside down inside an evaporation unit (Fig.4.1(a)). The boats located at the bottom of the chamber are then loaded with the material that will be later evaporated. The chamber is finally closed and brought to high vacuum conditions by means of two neighboring pumps. The low pressure assures the right cleanness of the sample as well as it maximizes the mean free path of the evaporated particulate, which can therefore hit directly the target as shown schematically in Fig.4.1(b) (right).

To trigger the evaporation, the frame that holds the source material is heated by an electric filament at a suitable current. The melting point of the material sets of course the value of the current, whilst the evaporating time defines the thickness of the coating. Finally, the evaporation angle determines the ratio of patchiness; in particular, the half coverage is obtained by evaporating at 90 degrees.

Once the process is completed the patchy colloids are shaken out of the colloidal substrate using an ultrasonic bath and diluted in a chosen solvent.

The single particle experiments presented in the next Chapters are performed using Au-coated colloids (see SEM-picture in Fig.4.1(c)). The thickness of the Au layer is usually set to 20 nm. An additional thin layer of Cr (2 nm) is added underneath the gold to provide a good adhesion. As we will see in details throughout the following Chapters, the role of the gold coating consists in being selectively heated up when illuminated with green light in contrast with the uncoated SiO_2 hemisphere that remains transparent to it. This way, a local temperature profile, necessary for the self-propulsion, is achieved.

The gold coating can be replaced by a layer made of a different material, provided that it absorbs enough light. With the same evaporation unit (Fig.4.1 (a)) we have realized Al, Cu and Ag coatings and all of them guarantee the light absorption needed for the propulsion. However, metals have sometimes disadvantages as coating materials; for instance, we observe a large attraction between gold-coated hemispheres due to Van der Waals forces leading to a significant sticking.

4.1.2   Stability of multiple particles suspensions

If we work with multiple particles systems, such as dense suspensions of Janus colloids, we need to take care that the coating is not going to affect the overall colloidal stability, i.e., that the additional layer does not induce attraction-driven aggregation.

Homogeneous SiO_2 colloids are stable in aqueous solutions thanks to the OH^- ions that get bound to the silica atoms and, therefore, accumulate at the colloidal surface. This cloud of ions provides an electrostatic screening against aggregation. However, when an attractive force is added the situation might abruptly change and the colloidal suspension can collapse into larger clusters.

For large enough attraction, the gain of energy overcomes the loss of entropy and the suspension separates into a dense liquid or solid, and a dilute gas phase. This behavior has been studied both theoretically [116, 117] and experimentally with colloids characterized by tunable attractions [118, 119, 120, 121]. In my view, the most self-explanatory example (albeit not the first in time) is the experiment performed in the Weitz's group in Harvard [121, 122]: a short-range attraction is hereby induced by the presence of depletion agents in solution[1]. The strength of the attractive potential is determined by the concentration of depletants. Long-range repulsions can be screened by adding salt to the solution [121]. Real space snapshots are taken using confocal microscopy (see Fig.4.2(a),(b),(c),(d)).

---

[1]Depletion forces comes into play when colloids are immersed, e.g., in a polymer solution. The attractive potential is triggered by the excluded volume between two neighboring colloids [38].

When the depletion forces are weak, the suspension remains homogeneous as in the absence of depletants (Fig.4.2(a)). Increasing slightly the polymer concentration the colloidal beads start aggregating into small clusters (Fig.4.2(c)) that, anyways, do not growth beyond a characteristic size. This phase is commonly known as *cluster fluid* and has been experimentally observed with or without additional repulsive potentials [121], although it has been theoretically predicted only in the presence of long-range repulsions [116]. Finally, higher attractions lead to the coalescence of the small cluster into a large aggregate, i.e., to the phase separation of the suspension (Fig.4.2(b)). For completeness, during this transition the dynamics can eventually arrest yielding a non-percolating worm-like structure as shown in Fig.4.2(d). This arrested state is know as *gel phase*, although this "phase" is purely kinetic and does not have any thermodynamic meaning [122, 117, 123, 116].

Since SiO_2 homogeneous colloids do not show aggregation, in our experimental systems, attractive forces could be only due to the coated side. We realized that the origin of additional attractions is related to Van der Waals interactions between the coated hemispheres. While the full form the potential strongly depends on the geometries of the system, the strength of the attraction is essentially given by the so-called *Hamaker constant*. The Hamaker constant A is indeed the pre-factor of the Van der Waals potential and gathers all the relevant parameters (e.g., the index of refractions or the dielectric constants) that define the pair interaction mediated by a liquid. The larger is A, the stronger is attraction between the particles. Literature values are usually available for many common materials in aqueous media [124].

By glancing at these tables, one can immediately notice that, compared to other materials, A is particularly high in case of metallic surfaces. For this reason, gold-capped colloids have the tendency to stick to each other, as confirmed by experiments at high particles concentration. Hence, when dealing with multiple particles systems, we decided to employ carbon-coated colloids instead. The carbon is hereby deposited using a different apparatus, yet based on a similar evaporation protocol[2].

While the carbon layer remains as effective as the gold one in absorbing green light (I will repeatedly highlight the importance of this aspect in the next Sections), the Hamaker constant between two carbon surfaces immersed in water is roughly one order of magnitude smaller ($A_{Au} \cong 27 \times 10^{-20}\ J$ *vs* $A_C \cong 3.7 \times 10^{-20}\ J$). Consequently to this, we expect weaker Van der Waals attractions.

In fact, a qualitative look at a dense suspension of carbon-capped particles (see inset of Fig.4.2(b)) already proves the absence of significant aggrega-

---

[2]We are grateful to the biology institute of the University of Stuttgart for granting us with the use of their facility.
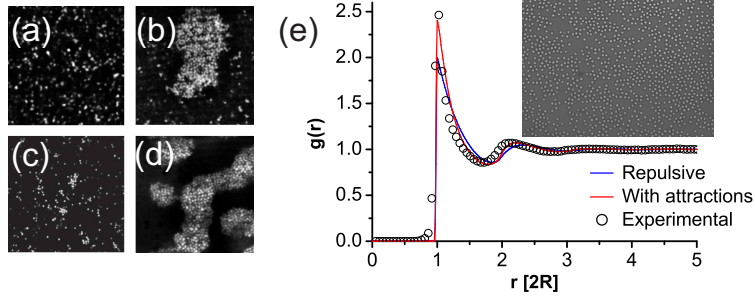
Figure 4.2: Confocal pictures [121] of: (a) Homogeneous colloidal fluid. (b) Phase separated suspension. (c) Cluster fluid. (d) Gel-like phase. (e) Structure of the passive suspension in equilibrium [125]: Experimental pair distribution function $g(r)$ at packing fraction 0.37 and simulation results employing the a purely repulsive (blue line) or a slighly attractive (red line) potential. The inset shows a microscope image of the system of carbon-coated colloids ($R = 2.13 \ \mu m$, the coating is not visible at the 50X magnification used to take the snapshot). The suspension is confined in 2D.

tions. The suspension appears homogeneous and, in time, we do not observe the formation of clusters under equilibrium conditions. To justify this statement on a more quantitative level we decided to plot the pair correlation function of the highlighted suspension in order to estimate the attractive potential [125]. The pair correlation (or radial distribution) function $g(r)$ describes indeed the density distributions in terms of relative position between the particles. In equilibrium and for dilute systems, it can be related to the pair potential $U(r)$ as follows:

$$g(r) = e^{-\frac{U(r)}{kT}} \tag{4.1}$$

In Fig.4.2(b) the experimental $g(r)$ (black circles) is compared with numerical simulations recovered with different attractive potentials. The blue curve considers purely repulsive hard spheres, whereas the red line also includes small attractive forces of the order of $0.5k_BT$. Therefore, a weak attraction is still present but $0.5k_BT$ is not sufficient to induce attraction-driven aggregation which comes into play with values above the k_BT threshold, instead [121, 116]. For this reason the colloids will be often reasonably approximated with repulsive spheres, described by the following pair Yukawa potential:

$$U_Y(r) = p_1 \frac{e^{-r/p_2}}{r/p_2} \tag{4.2}$$

where p_1 and p_2 are parameters chosen to match the physical values.

4.2 The solvent

4.2.1 The sample cell

After the evaporation/deposition step the Janus particles are ready to be dissolved in a chosen liquid. As a solvent, for reasons that will be clear in the next Chapters, we use a critical binary mixture of water and 2,6-lutidine, an aromatic organic compound. The Janus colloids are added, at a desired concentration, to the critical mixture and the resulting suspension is then poured onto a glass slide.

In equilibrium, due to gravity, the colloids sediment to the bottom slide with only a tiny spacing caused by the electrostatic repulsions between the particles and the glass substrate. However, when the particles become self-propelled a motion along the z-direction is also possible; to avoid this 3D displacement and investigate the sole 2D motion of the colloids the sample is sandwiched by a further cover slip and the edges are sealed with a solvent resistant glue (see Fig.4.3(a)).

In order to prevent drift towards the edges, a further x, y-confinement is added as shown in Fig.4.3(a). This cavity has an area roughly twice as large as the field of view and a thickness equal to the diameter of the Janus colloids. Such thin additional layer is prepared by spin-coating a photorestist (SU-8, purchased from Microchem Corp.) on the bottom glass slide. The cavity is then realized through standard lithography techniques [126]. Under illumination with UV-light, the polymer is crosslinked and cannot be rinsed away by conventional solvents, e.g., isopropanol. The cavity is therefore "printed" if a suitable mask casts a shadow during the illumination process. We employ the same technique to imprint more complicated structures, such as obstacles with various geometries. The viscosity of the SU-8 and the spin velocity determine the thickness of the layer.

4.2.2 Properties of the critical binary mixture

The binary mixture (water-2,6-lutidine) in which the colloids are immersed has very unique properties. A simple fluid is usually characterized by *first order phase transitions*, typically liquid-gas, liquid-solid etc. The name "first order" is due to the fact that the free energy displays a discontinuity in its first derivative with respect to some thermodynamic variable. In liquid-solid transitions, for instance, this discontinuity shows up in the derivative with respect to the chemical potential, i.e., in the density [128].

Critical binary mixtures of two fluids, such as water/2,6-lutidine, still posses a first order criticality. The two liquids can either coexist in a homogenous phase or become immiscible forming an unstable emulsion of one fluid into the other; the transition between these two states occurs, at a fixed concentration of the species, increasing (or decreasing) the temperature. A
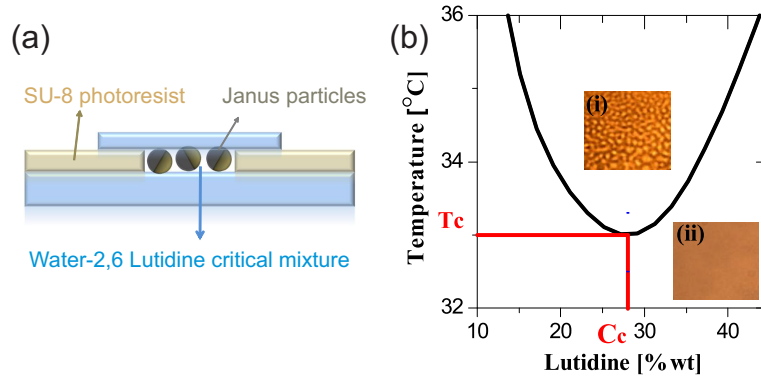
Figure 4.3: (a) Cartoon illustrating a typical sample cell used in the experiments. (b) A schematic phase diagram for water and 2,6-lutidine. The insets are bright-field microscopy pictures of the mixed (i) and the demixed (ii) phase at the critical concentration [127].

phase diagram is usually plotted as a function of the mass concentration ratio between the two species (x-axis) and temperature (y-axis). The curve obtained setting to zero the first derivative of the free energy with respect to density is called *binodal*: it separates the mixed and the heterogeneous phases and has approximatively the shape of a parabola (Fig.4.3(b)). Depending on the concavity, the mixture is defined by either an *upper* or a *lower critical point*. In the two cases the demixed phase is thus achieved by decreasing or increasing the temperature, respectively.

On top of this binodal decomposition, critical mixtures are also characterized, in the proximity of their critical point, by an additional feature. At the critical point, also the second derivative of the free energy is zero and this implies that the transition happens without any thermodynamic barrier (*spinodal decomposition*). The large localized fluctuations due to nucleation are thereby replaced by a continuous of clusters of the two species [128]. Thus the demixed phase shows, instead of the coalescence of droplets, a worm-like structure (see inset (ii) of Fig.4.3(b)) with a correlation length growing in time [129]. Novel soft material, called *bijels*, can be fabricated arresting the growth through colloidal particles that sits at the interface [130, 131]. Last but not least, the transition is utterly reversible, i.e., the two fluids remix crossing back the critical point .

Fig.4.3(b) illustrates a schematic phase diagram of the critical binary mixture of water and 2,6-lutidine employed in the experiments [127]. The mixture has a lower critical point, i.e., water and lutine phase separate in the area above the parabola. As mentioned above, the transition occurs via nucleation and growth everywhere but in the proximity of the critical point ($T_c = 307\ K$, 0.286 mass fraction of lutidine). In order to exploit the thermodynamic reversibility we always work at the critical concentration
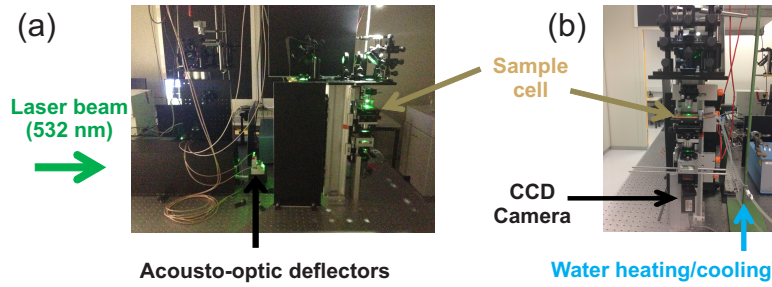
Figure 4.4: (a) Side and (b) front view of the experimental setup. The sample is illuminated from above and watched from below.

varying the temperature across its critical value: At the critical composition and below $307\ K$ the mixture is homogeneous, as shown by the bright-field picture in inset (i) of Fig.4.3(b). Increasing the temperature above T_c, the mixture separates via spinodal decomposition as described in the former paragraph. The worm-like demixed phase appears as shown in inset (ii). The physical properties of the mixture for different temperatures are nicely listed in Ref. [132].

4.3   The experimental setup

The home-built setup used to perform most of the experiments is shown in Fig.4.4(a) and (b) from two different angles. It basically consists in three parts:

1. A monochromatic illumination implemented using a green laser beam. The beam is first scanned by two Acousto-Optic Deflectors (Fig.4.4(a)) before hitting the sample from above (Fig.4.4(b)). The role of the illumination is to heat selectively the coated hemisphere of the Janus colloids, breaking, therefore, the symmetry of the system.

2. A water bath (connected to the sample cell with pipes as shown in Fig.4.4(b)) that provides an homogeneous heating of the sample (p.n., the bath is not shown in the picture).

3. A long distance 50x objective and a CCD camera connected to a PC (Fig.4.4(b)) in order to record real space videos of the colloidal suspension.

For the study of asymmetric self-propelled particles (see Chapter 7) we used a different apparatus, shown in Fig.4.5. It includes a commercial inverse microscope Nikon Eclipse TE2000-U equipped with a 100X immersion oil objective. The microscope is coupled to a mercury lamp X-Cite 120

Figure 4.5: The apparatus employed for measurements of asymmetric microswimmers (Chapter 7). The mercury lamp X-Cite 120 is not visible but illuminates the sample from below.
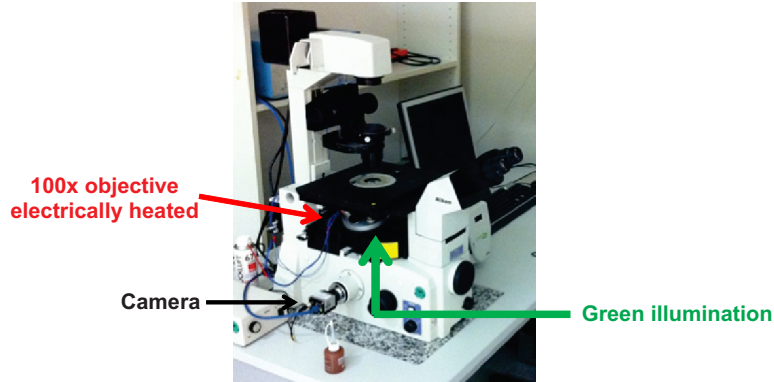
that has various light emission peaks at different wavelengths. The peak in the green is usually singled out through a bandpass filter 550/100 to maximize the absorption of the gold coating of the Janus colloids. Compared to a laser illumination, the power per area injected by the mercury lamp into the system is much lower. Since the self-propulsion is effective only if we work across the critical point the objective is also supplied with an electrical heating that operates alongside a thermal bath to adjust the base temperature.

In the following Sections I will only focus on the first setup (Fig.4.4(a) and (b)).

4.3.1   Heating and illumination with green light

In the self-propulsion mechanism I will present in Chapter 5, the illumination is responsible of breaking the symmetry. The incident light is in fact optimized to be uniquely absorbed by the coating of the particles, generating thereby a local temperature gradient across the colloid.

Thus, we decided to utilize a monochromatic light beam with a frequency centered within a high-absorption region of gold (the coating material). In particular, we use the light ($\lambda = 532\ nm$) generated by a 2.2 W (maximum power) of a green laser (Verdi, Coherent). After passing through some mirrors the light hits the sample from above as shown in Fig.4.4(a) and (b).

To achieve a large illuminated area, typically around $400 \times 400\ \mu m^2$, the laser beam is also first scanned using two Acousto-Optic deflectors (see Fig.4.4(a)). These devices are made of a TeO_2 crystal that deflects the incident beam as schematically illustrated in Fig.4.6(a). The physical principle is the following: a TeO_2 crystal has the ability to change its refractive properties when actuated by an acoustic transducer. The acoustic frequency
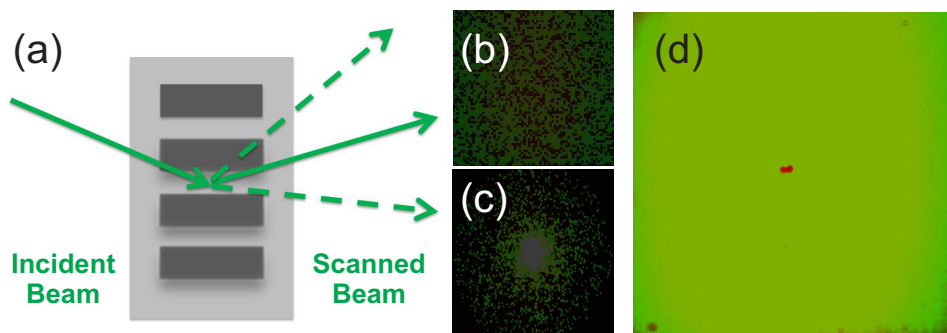
Figure 4.6: (a) Cartoon explaining the working principle of an Acousto-Optic Deflector (AOD). (b) Focused square light pattern obtained using two AOD. (c) Focused radial gradient pattern. (d) Homogenous illumination achieved by defocusing the square pattern shown in (b).

hereby determines the scattering angle. A laser beam that travels throughout the crystal can be therefore scattered with a controlled angle. In order to scan the x and the y directions the beam is often guided by a pair of Acousto-Optic deflectors (AOD).

AODs are often used for optical manipulation purposes, e.g., optical tweezing. However, in our experimental system, we exploit the fact that each deflection can be performed in a very short time interval, i.e., with a jumping time up to 0.1 MHz. Due to this extraordinary high scanning frequency, we obtain *de facto* quasi-static 2D light patterns like the ones shown in Figs.4.6(b), (c). We usually employ patterns made of 4000 spots: at 0.1 MHz, this corresponds to a repetition time (the time between two consecutive scans of the same spot) of 40 ms. To confirm the quasi-static nature of the illumination, we note that in 40 ms an active particle typically travels a distance up to 0.2 μm which is smaller than the particle's radius. Since each spot is larger than the size of the colloids, we conclude that the swimmers indeed experience a static illumination in the range of velocities used in the experiments.

The AODs are controlled via PC by means of a commercial software called "Tweez". We typically make use of a simple square pattern (Fig.4.6(b)), roughly twice as large as the field view, to achieve an homogeneous illumination throughout the sample. Nonetheless, AOD provide us with the possibility of making more complicated light fields such as the radial gradient displayed in Fig.4.6(c).

Nonetheless, the highly focused light patterns shown in Figs.4.6(b) and (c) exerts remarkable optical forces onto the colloid dispersed in solution. Since we aim to have a smooth illumination, lacking such optical implications, the light that hits the colloidal suspension is finally strongly defocused (spot radius $\approx$ 30 μm), leading to the homogeneous light field of Fig.4.6(d).
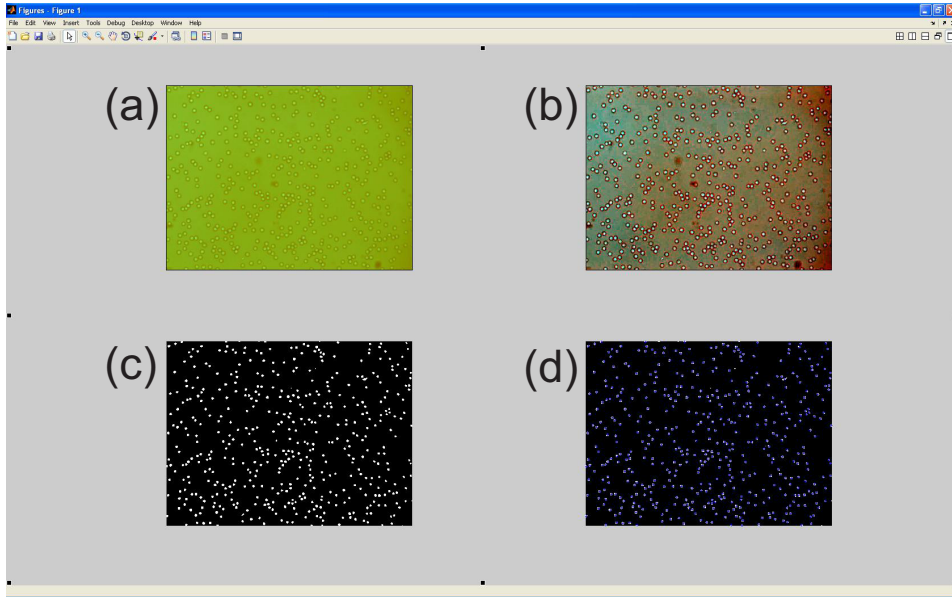
Figure 4.7: Main steps of the tracking Matlab routine. (a) Original image. (b) Stretched image. (c) Binary image obtained after applying the brightness threshold. (d) Detection of the centers of mass of the colloids.

Calculating the power density, we estimated illumination intensities from few up to roughly 10 $\mu W \mu m^{-2}$ [127]. These values allow us to rule completely out optical forces which are typically relevant only for intensities at least an order of magnitude larger [133].

The laser power is usually enough to heat, by absorption, the coating of the particles from room temperature up to the critical point ($T_c = 307\ K$) of the surrounding binary fluid. However, smaller illumination intensities can be also employed, provided that the whole sample is homogeneously heated and kept at, typically, few degrees below the critical temperature. To do so, in some experiments we did this connecting a water bath to the sample cell (Fig.4.4(b)). This allowed us to access higher swimming speeds (details will be provided within Chapter 5).

4.3.2 Video acquisition and analysis

Once a colloidal suspension is sealed inside a 2D confinement as previously shown in Fig.4.3(a), its behavior (with and without illumination) is finally watched and recorded in transmission using a CCD camera placed underneath the sample (see Fig.4.4(b)). The cavity is $400 \times 400\ \mu m^2$ large (p.n., the cavity has the same size of the illuminated area). We record the behavior of the suspension in an area of $290 \times 218\ \mu m^2$, located approximately in the middle of the cavity, using a resolution of 1280×960 pixels and a

52

recording frequency of 7.5 frames per second.

In order to extract the trajectories of the colloids, we have implemented in Matlab a customized tracking routine. It is essentially based on brightness threshold levels, i.e., the particles are recognized when they appear brighter (or darker) than the background. The main steps are illustrated in Fig.4.7. The original image (Fig.4.7(a)) is first stretched to increase the contrast with the background (Fig.4.7(b)). The RBG picture is then converted into a binary image (Fig.4.7(c)), i.e., pixels brighter than a certain threshold are converted into white, whereas the others turn black. The threshold is optimized to detect the colloids. The center of mass of the white spots, corresponding to the colloids, is finally detected and followed frame by frame (Fig.4.7(d)). Additional filters can be introduced to address dense colloidal suspension or situation where the background is not homogeneous, e.g., due to the presence of obstacles.

Part III

Experimental results

Chapter 5

Light-driven microswimmers

With this Chapter, I finally come to the core of the manuscript, matching together all the concepts I introduced so far. To recap, in the former Chapters we have seen that an artificial micrometric object (microswimmer) can propelled itself in a liquid if and only if is able to break the time reversal symmetry. A clever solution to do so consists in modifying asymmetrically the local properties (e.g., chemical composition, ion density, temperature) of the surrounding medium. This leads to an heterogeneous interaction between the surface of the particle and the molecules of the liquid, occurring within a tiny superficial layer. An internal force (*phoretic force*) is directly associated to this interaction. Thus, the particle acts as an autonomous engine, capable of producing its own "fuel". When the propulsion is combined with the classical Brownian motion of a micro- or nano-metric particles, the resulting motion (*active Brownian motion*) possesses very anomalous features that are yet not fully understood.

Moreover, I've described several propulsive mechanisms that have been recently developed to phoretically drive a colloid inside a liquid environment. For instance, Janus particles show self-propulsion when they are able to generate either a local chemical gradient (e.g., through the decomposition of H_2O_2) or some kind of temperature slope.

In the next Sections, I will put together all the ingredients I have introduced within Chapter 4 to devise a novel propulsion mechanism: we use a laser illumination to heat up by light absorption the coated hemispheres of Janus colloids. Particles are immersed in a critical mixture of water and 2,6-lutidine which is kept close to its critical point. Upon a suitable illumination, the binary mixtures located in the proximity of the heated hemispheres undergoes a phase transition. When this happens, we observe that the colloids start performing active Brownian motion.

At first glance, the asymmetric heating suggests a propulsion induced by self-thermophoretic; however, I will point out that this is not the case. Our colloids are driven by **self-diffusiophoretic forces** due to the criti-
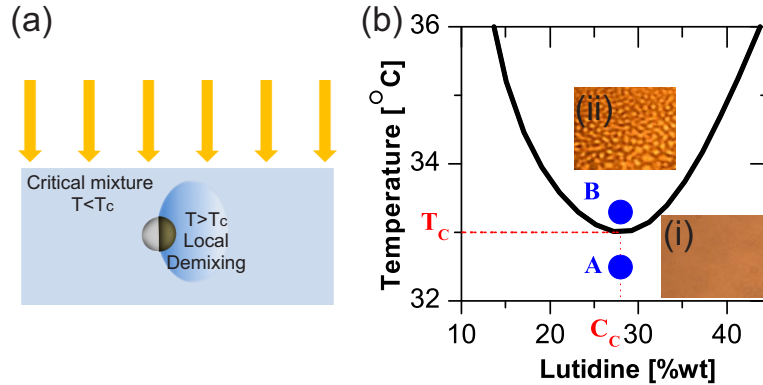
Figure 5.1: Active Brownian micro-swimmers in a critical binary mixture. (a) Schematic cartoon explaining the self-propulsion mechanism: a Janus particle is illuminated and the cap is heated above T_c inducing a local demixing that eventually propels the particle [127]. (b) Phase diagram and bright-microscopy snapshots of the critical mixture of water and 2,6-lutidine. The points A and B stand for the thermodynamic states when the laser is "off" and "on", respectively [127].

cal decomposition of the binary solvent. I will also stress the advantages and drawbacks of this driving method in contrast with other mechanisms available in the literature.

5.1 The propulsion: self-diffusiophoresis

We observe that Janus colloids fabricated according to the protocol of §4.1.1 behave as active swimmers when are both immersed in a critical binary mixture of water-2,6-lutidine and illuminated with green light.

To demonstrate the effectiveness of the propulsion and to elucidate the principles behind it, we prepared a dilute sample of Janus colloids following the method described in §4.2.1. We used silica spheres with radius $R = 2.13$ μm half-coated with 20 nm thick gold caps. The surrounding mixture is at the critical concentration (0.286 mass of lutidine) and the sample cell is 7 μm high [115].

The base temperature of the system is controlled by a thermostat and adjusted roughly one degree below the critical point $T_c = 307\ K$. Therefore, at the beginning of the experiment the whole sample is in equilibrium and the solvent is described by the point A of the reported water-lutidine phase diagram (Fig.5.1(b)). In particular, the mixture is everywhere homogeneous, i.e., the two phases (water and lutidine) are mixed together as shown by the bright-field picture in inset (i) of Fig.5.1(b).

The whole field of view is then illuminated with a green ($\lambda = 532\ nm$) laser light coming from above (see Fig.5.1(a)). As discussed in §4.3.1, the

green light is chosen because it is located near the plasmonic absorption peak of gold [134]. The laser beam is also scanned by two Acousto-Optic Deflectors (AOD) and strongly defocused before hitting the sample (again, refer §4.3.1 for details). The light intensity is always kept lower than $\approx$ 10 μW μm^{-2} to rule completely out optical forces, that come in play with values at least one order of magnitude larger.

Due to light absorption, the gold caps are heated above T_c. On the other hand, the temperature at the silica side does not change because silica does not absorb green light. The heating of the caps propagates all the way to the neighboring liquid and triggers the local decomposition of the critical mixture (Fig.5.1(a)). Inasmuch as we work at the critical concentration, this transition occurs via spinodal decomposition: jumping from the point A to the point B the solvent undertakes the bicontinuous worm-like structure of inset (ii). Since the spinodal decomposition occurs without thermodynamic barriers, the transition is utterly reversible, i.e., when the laser light is turned off again, the binary fluid goes back to the mixed state (point A and inset (i)).

If the laser is off the Janus particles simply perform classical Brownian diffusion. On the contrary, when the light absorption triggers a local demixing nearby the coated hemisphere, we observe that the colloids become self-propelling undergoing a directed motion. The reason behind the propulsion is embedded in the phoretic forces that arise when the liquid nearby the particle has asymmetric physical properties, such as in the case of a gradient. Depending on which kind of gradient surrounds the colloids the propulsion can be caused by electrophoretic, thermophoretic or diffusiophoretic forces (see Chapter 2).

To clarify the main mechanism responsible of the driving, we took a deeper look at the propulsion and we compared it with other phoretic swimmers recently devised.

On one hand, it is trivial that when only half of the particles is heated by light absorption a thermal gradient naturally comes into play. Thus, thermophoresis is naively the first "suspect". Our experiment is, in fact, very similar in spirit to the one carried out by Sano and coworkers [83] (§2.2.2) where a thermophoretic propulsion was observed. In both case a gold-coated colloid is illuminated with green light to generate a local temperature gradient. The differences are the solvent (we use a critical mixture instead of water) and the illumination intensities employed.

In Sano's experiment, gold-coated colloids, dispersed in water, are driven by thermophoretic internal forces when illuminated by the (slightly) defocused green laser light. The illuminated spot is hereby rather small (10 μm in diameter) and this leads to a power density larger than 100 μW μm^{-2}. In our case, due to a much wider illumination field, the light intensity is about two orders of magnitude smaller. This implies that the temperature difference and, thus, the thermophoretic driving are expected to be much weaker.
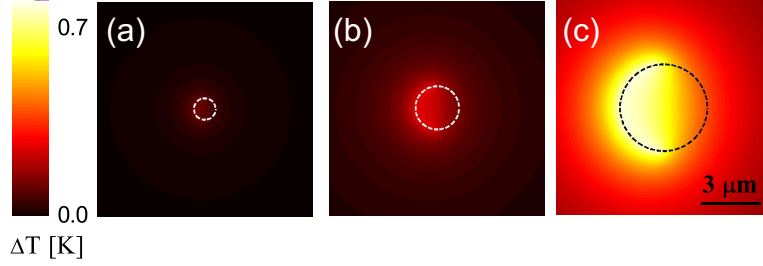
Figure 5.2: Light-induced heating. Temperature increase ΔT in the equatorial plane of a Janus particle with $R =$ (a) 0.5, (b) 1 and (c) 2 μm. In all cases, the dashed line profiles the contour of the particle, the cap is on the left side and the light intensity I is 1 $\mu W \ \mu m^{-2}$ [127].

However, operating with a binary mixture across the critical point does not allow us to isolate the thermophoretic contribute from effects caused by the redistribution of the solvents (diffusiophoresis).

In order to confirm our feeling about the negligibility of thermophoretic forces we performed the experiment illustrated in Fig.5.1(a) with bare water at the same conditions of light intensity. In other words, we reproduced Sano's experiment with a far weaker illumination. No active motion is hereby observed. We therefore conclude that, in contrast with Ref. [83], thermophoretic forces are not the main contribute to the propulsion in our system.

To better understand the heating process induced by the illumination, we have numerically estimated the temperature increase ΔT for an incident light intensity comparable with the experimental values. Heat is generated only in the cap because of the absorption associated to the imaginary component of the dielectric constant of gold, and then diffuses in the surrounding materials, i.e., the silica sphere and the water-2,6-lutidine medium, according to the Poisson heat equation [127].

We followed the green dyadic method [135, 136] with the goal of simulating the light absorption of the gold coating. This method has the remarkable advantage of focusing on morphology features while discarding volume effects. In short, this approach is based on the evaluation of the absorption cross section σ_{abs}; under a uniform plane-wave illumination, this quantifier has the following expression [135]:

$$\sigma_{abs} = \frac{k}{\varepsilon_0 \left| \mathbf{E}_0 \right|^2} \int_{NP} Im(\varepsilon_w) \left| \mathbf{E(r)} \right|^2 d\mathbf{r} \tag{5.1}$$

where k is the wave-vector of the incident light, ε_w is the permittivity of the material and $\mathbf{E}_0$ and $\mathbf{E(r)}$ are the electric field of the incoming light and the total electric field, respectively. The latter is calculated propagating $\mathbf{E}_0$ by means of an operator that is a function of the physical parameter of the

illuminated material, i.e.,

$$|\mathbf{E}(\mathbf{r})| = \int \mathbf{K}(\mathbf{r}, \mathbf{r'}, w)\mathbf{E}_0(\mathbf{r'})d\mathbf{r'} \tag{5.2}$$

Once the absorption cross section is known the heat produced on the metallic coating is simply given by its product with the irradiance of the incoming light.

$$Q = \sigma_{abs} \cdot I = \frac{nc\varepsilon_0}{2}|\mathbf{E}_0|^2 \tag{5.3}$$

where n is the optical index of the liquid.

Finally, the heat Q diffuses, according the classical Poisson heat equation, into the surrounding medium yielding the full temperature profile.

Considering the physical properties of the materials involved in the process (gold, silica and water-2,6-lutidine), we derived, for different radii R (0.5, 1 and 2.13 μm) of the Janus colloid, the results displayed in Fig.5.2. The snapshots are obtained for a linearly polarized green illumination with intensity 1 μW μm^{-2}. The coated hemisphere is located on the left side of the particle, whose contour is marked with the white dashed line; brighter colors correspond to larger ΔT.

We notice a sharp temperature transition at the edge between the capped and uncapped sides of the particle which validates the assumption that the light is uniquely absorbed by the gold coating. Moreover, as the particle size increases, ΔT becomes larger, because of the higher heat dissipation at the metallic cap. Last but foremost, the temperature difference is in all cases smaller than 0.7 K. This value, weighted across a distance of few microns (the size of the colloid, is too small to provoke a noteworthy thermophoretic migration[1]. We noted that these results are independent of the the base temperature.

Rather than in thermophoretic forces we found a reasonable justification for the directed motion in the local concentration gradient that comes along with the decomposition of the mixture once the critical point is crossed.

When the heat generated by the illuminated coating is enough to lead to the local spinodal demixing (Fig.5.1(a) and (b)), water and lutidine rearrange around the particle according to its surface properties. In particular, since Au and SiO_2 are obviously two different material, they never possess the same degree of hydrophilicity. When no functionalization of the surface is made, the evaporated Au is usually more hydrophobic than the colloidal SiO_2. Therefore, as soon as the phase separation happens, water and lutidine tend to accumulate nearby the material they have more affinity with.

---

[1]The strength of a phoretic force is given by the steepness of the gradient rather than by its absolute value.

To clarify this point we performed the paradigmatic experiment shown in Fig.5.3. We basically repeated the single particle experiment highlighted in Fig.5.1 with a further control over the surface properties of the evaporated layer of gold. Before dispersing the Janus particles in the critical mixture we spread a thiol solution on the particles and let it dry. The thiolate groups strongly bond with the gold surface, thereby modifying its surface preference. In particular, we render the gold cap strongly hydrophilic or hydrophobic through the functionalization with 11-Mercaptoundecanoic acid and 1-Octadecanethiol, respectively [127]. To distinguish the two phases (water and lutidine) after the decomposition, we also labelled the organic one with a dye (Rhodamine 6G). We finally turned on the illumination with rather high light intensity ($I = 10\ \mu W\ \mu m^{-2}$) and observed the directed motion of the Janus colloid as well as the rearrangement of the two phases after the local demixing.

In Figs.5.3(b) and (d), we show the fluorescence intensity encoded in color: yellow and red correspond to a rich-lutidine and a rich-water region, respectively. In particular, Fig.5.3(b) shows the concentration of lutidine around a Janus particle with a hydrophilic cap. The cap is easily identified as the bright half-moon shape at the center of the picture. Upon illumination, the lutidine becomes depleted from the area near the cap (red), while it accumulates at the silica side (yellow), which is hydrophobic (in comparison to the hydrophilic-functionalized cap), thus resulting in a concentration gradient around the particle. The particle moves within this gradient in the direction of the lutidine-rich phase as indicated by the red arrow. The cartoon of Fig.5.3(a) sketches the view from side and underlines that the cap is the rear of the particle. Contrariwise, Fig.5.3(d) shows the lutidine concentration around a Janus particle with a hydrophobic cap. In this case, the lutidine-rich phase (yellow) accumulates at the cap, while the water-rich (red) phase populates the silica side, the latter being more hydrophilic than the cap. Again, the particle moves within the resulting gradient towards the lutidine-rich phase (arrow). The coating is now the head of the colloid during the active motion (Fig.5.3(c)).

This experiment proves that the Janus colloids are propelled by **self-diffusiophoresis**, i.e., by a local concentration gradient of the two phases in the surrounding. The word "self" emphasizes that the particles themselves generate these gradients by triggering the spinodal decomposition when illuminated with light. The snapshots shown in Figs.5.3(b) and (d) are also an incontestable proof that thermophoresis is not the main mechanism of propulsion; in fact, if this was the case, no change of direction would be observed depending on the cap functionalization. The particle would always move towards the hot or the cold side, no matter where the lutidine-rich phase is.

The strength of the propulsion is given by the steepness of these concentration gradients (see §2.1.2); it can be tuned easily by tweaking the illu-
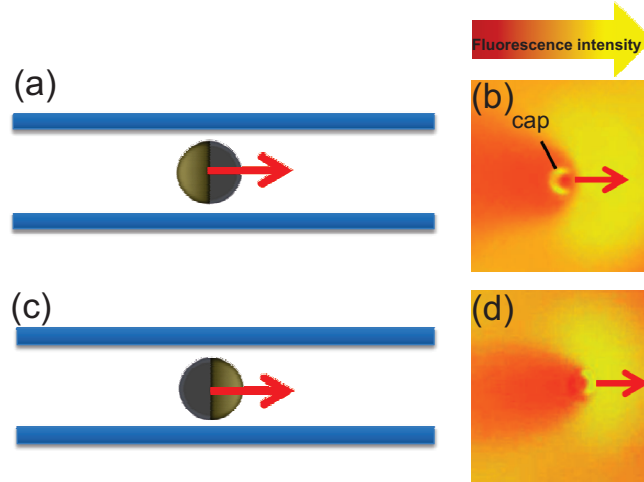
Figure 5.3: Direction of the propulsion when the cap is hydrophilic ((a) and (b)) or hydrophobic ((c) and (d)). (a) and (c) schematically reproduce the side view of the sample whereas (b) and (d) are fluorescence experimental snapshots. The lutidine phase is labelled with a hydrophobic dye (Rhodamine 6G) that in the picture appears yellow. The gold cap correspond to the bright half-moon shape. Since the size of the demixed regions depends on the illumination intensity, the latter is set significantly high in order to visualize the gradient better (10 μW μm^{-2}) [127].

mination power injected into systems. Higher light intensities imply a more pronounced decomposition and, therefore, wider and steeper concentration profiles nearby the colloid. It is important to remark that the pictures 5.3(b) and (d) have been taken under a rather extreme regime of light intensity ($I = 10 \, \mu W \, \mu m^{-2}$, value much larger than the typical power employed in all the other experiments) in order to visualize the surrounding gradient. Typically, the demixed area is not visible with conventional bright microscopy since it involves only a tiny region around the particle.

The self-diffusiophoretic driving mechanism we propose is complementary to the system of Janus particles in H_2O_2 solution, presented in §2.2.2. Colloidal particles self-propelled in H_2O_2 have been recently widely employed to investigate the active motion of micrometric beads [72, 73, 74, 75, 82]. In short, colloids coated with a catalyst (e.g., Pt) can locally decompose the hydrogen peroxide and, thereby, generate a local concentration gradient that propels diffusiophoretically the particle. Such system is well-conceived since the bulk concentration of H_2O_2 determines the strength of the propulsion.

However, the catalytic reaction of H_2O_2 also carries along some limitations: first of all, the peroxide acts as a "fuel" and is therefore consumed every time the particle gets propelled. A constant fuel supply has to be real-
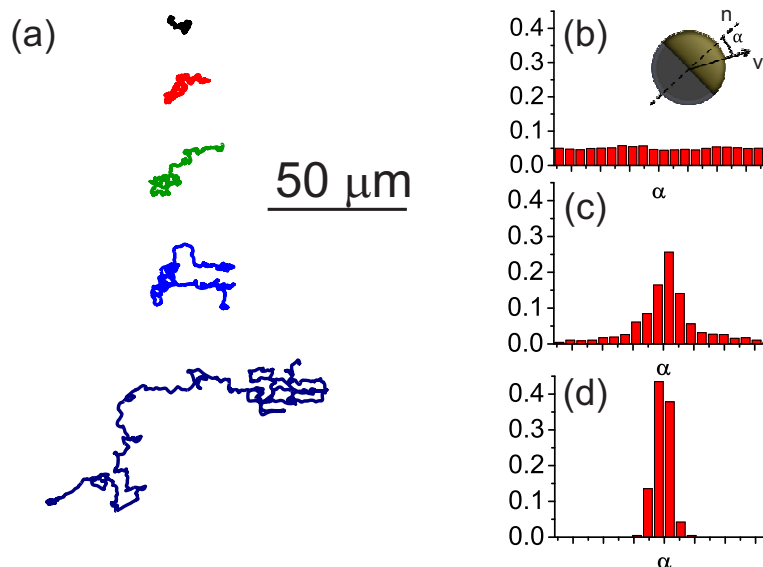
Figure 5.4: Active trajectories. (a) 2D trajectories (1000 s) of a Janus particle for illumination intensities (from top to bottom) $I = 0, 69, 92, 115, 161$ nW μm^{-2} [115]. (b) Probability distribution of the angle α (inset) between the cap and the particle velocity for (from top to bottom) $I = 0, 69,$ and 138 nW μm^{-2} [115].

ized, e.g., by using a microfluidic chamber [72]. This energy supply becomes tricky when the colloidal suspension is rather dense, since the reservoir of H_2O_2 cannot keep up with the consumption made by the particles. I am not aware of experiments with self-propelling colloids in hydrogen peroxide solution with particle density (read in 2D, area fraction) larger that 0.2 [73, 82]. In our case, since the demixing of the critical mixture is only local, the water and the lutidine phases remixe as soon as the colloids has travelled past, i.e., the "fuel" that drives the microswimmer regenerates once the particle has moved to a different region of the sample.

Furthermore, the use of the laser light as trigger for the self-propulsion allows us to have an external control over the propulsion strength, that can be freely turned off/on or adjusted *in situ*. This degree of freedom was only achieved very recently on H_2O_2 systems by employing an hematite cube, attached to the colloid, as a catalyst [82]; the hematite, in fact, decomposes the H_2O_2 only if illuminated with UV light. However, due to the chemical synthesis of the colloids, the degree of patchyness is fairly polydisperse.

The downside of our driving method consists in the fact that, for how the illumination is designed, it is limited to 2D systems, whereas the propulsion driven by H_2O_2 is effective in 3D samples, alike.

5.2   Active trajectories

When a Janus particle is equipped with an internal propelling force, its motion becomes directed and any random reorientation is only due to rotational diffusion. In other words, the translational motion change radically while the rotational diffusion D_R remains unaffected. Since the colloidal suspension is constrained in 2D by two glass slides (Fig.5.1), the translation occurs only in the x, y whereas the rotation is still 3D. The motion is, thus, *quasi*-2D.

The Janus colloids can be propelled either in or in the opposite direction of the coating, but, anyhow, the motion always follows the direction of the asymmetry. The latter of course varies, continuously and randomly, owing to the rotational motion. In particular, when the driving force gets oriented towards the glass confinements, the directed motion is arrested by the walls and the effective 2D translational motion is solely given by Brownian diffusion.

If we fix the radius R of the particles, the typical reorientation time $\tau_R = D_R^{-1}$ does not vary and the shape of the 2D trajectories is only given by the strength of the propulsive events, which is, in turn, determined by the illumination power. Fig.5.4(a) shows the trajectories of particles with $R = 2.13\ \mu m$ when confined a 7 μm thick cavity and illuminated at different laser intensities. While the rotational diffusion D_R is the same for all cases, the different propulsion strength leads to fairly distinguishable trajectories. In particular, the black one corresponds to $I = 0$, i.e., to classical Brownian diffusion; increasing the laser power, the trajectories become characterized, at short time scale, by ballistic segments, whose length grows with the laser power.

These straight segments confirm the tendency of the active particle to proceed with a fixed orientation for some time, until rotational diffusion comes into play. This orientation coincides with the direction of the particle asymmetry. To demonstrate this last statement we plotted in Figs.5.4(b),(c), and (d) the distributions of the angle α between propulsion direction $\mathbf{v}$ and the cap orientation $\mathbf{n}$ (see inset of Fig.5.4(b)) for increasing illumination intensities. When the particles is just Brownian ($I = 0$, Fig.5.4(b)), the distribution is uniform since the colloid jiggles randomly in the whole 2D space. On the other hand, the distribution becomes strongly peaked around $\alpha = 0$ with growing I (Figs.5.4(c) and (d)), which demonstrates that the propulsion force acts in the direction of the asymmetry. In particular, since the gold cap is strongly hydrophilic (see §5.1) the ballistic velocity points in the direction opposite to the coating.
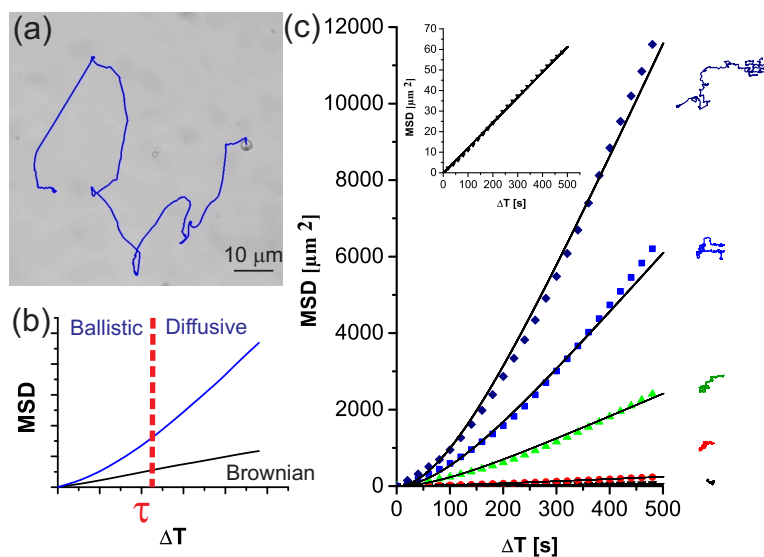
Figure 5.5: Displacement properties of the active motion of self-propelled particles. (a) Trajectory of an active Brownian particle ($R = 2.13$ μm) drawn on top of a bright microscopy snapshot. (b) Sketch explaining the information contained in the MSD of a self-propelling particle. (c) Experimental mean square displacement of active Janus particles ($R = 2.13$ μm) for $I = 0$ (black), 69 (red), 92 (green), 115 (light blue), 161 (dark blue) $nW\mu m^{-2}$. The inset shows the zoom of the black curve. The corresponding trajectories are drawn aside each curve with the same color [115].

5.3   Properties of the active motion

Let us analyze more in detail the trajectory properties introduced in the last Section. The physical motion where a diffusive component (rotational and translational) is combined with a ballistic propulsion is usually addressed as *active Brownian motion*. In Chapter 3 I've presented few ways to describe precisely this type of motion. In the following paragraphs I am going to contextualize in these description the behavior of the self-propelling colloids.

As we have have seen in §3.2.2, the active Brownian motion of biological or artificial microswimmers is modelled as a random walk equipped with a persistency (*correlated or persistent random walk*). When an object takes up energy from the environment and converted into kinetic motion, it shows a tendency to persist towards specific direction, although the reorientations still remain random. For "run" and "tumble" bacteria this persistency is given by the travelling space between two consecutive tumbling events. In case of self-propelling particles, such as the ones presented in the last Sections, the reorientation happens smoothly since the rotational diffusion is a continuous process.

Fig.5.5(a) illustrates the trajectory of a self-propelling Janus particle,

plotted on top of the corresponding bright microscopy picture of the sample. The active motion of the colloid clearly displays the property of a persistent random walk: The particle has a ballistic behavior until a significant reorientation steers the motion. In other words, at short time scales the motion is ballistic, as confirmed by the straight paths of the trajectory of Fig.5.5(a), while it becomes diffusive again at time large compared to the typical rotational diffusion. This mean that if we look at the trajectory of Fig.5.5(a) after enough time, it will appear as it were Brownian.

The competition between ballistic and diffusive behavior is tracked down very well by the behavior in time of the mean square displacement (MSD). A first sketch is shown in Fig.5.5(b)[2].

The MSD of a self-propelling particle is clearly characterized by two distinguishable regimes: the ballistic behavior at short-time scales with a quadratic growth of the MSD in time and the diffusive one at large t where the increase is linear. The crossover τ between the two regimes defines the persistency of the motion, i.e., the *average persistence timescale* over which the trajectory direction is maintained. We do expect this timescale to coincide with the typical rotation time $\tau_R = D_R^{-1}$ of the particle. The definition of *persistence* or *swimming length l* follows automatically as the product between τ and the ballistic velocity v of the active particle. Moreover, the long-time diffusive behavior is describe by an enhanced diffusion coefficient, given by the slope of the line. This effective diffusion D_{eff} is sometimes sketched with an effective temperature T_{eff}, according to the Einstein's definition (3.1) of the diffusion coefficient and assuming that the system reaches a steady state at large t.

In Chapter 3, I have demonstrate how the behavior of the MSD of self-propelling colloids shown in Fig.5.5(b) can be fitted by the following relation:

$$MSD(t) = 4\left(D_0 + \frac{1}{4}\frac{l^2}{\tau}\right)t + \frac{l^2}{\tau}\left[e^{-\frac{2t}{\tau}} - 1\right] \qquad (5.4)$$

where τ is again the characteristic timescale shown in Fig.5.5(b), $l = v\tau$ is the persistence length defined above and D_0 is the bare diffusion coefficient of the particle when the illumination is off, i.e., when the bead is just Brownian. Due to the 2D confinement D_0 does not coincide with the Einstein's value $D_0 = (k_B T)/(6\pi\eta R)$ for a sphere of radius R in bulk. Instead, we calculate D_0 from the linear fitting of the experimental MSD of the particle in the absence of illumination, i.e.

$$MSD(t)_{I=0} = 4D_0 t. \qquad (5.5)$$

Eq. (5.4) contains the information about the two regimes illustrated in Fig.5.5(b). The asymptotic behavior for $t \gg \tau$ (*large time scales*) leads to

---

[2]Fig.5.5(b) is meant as a tutorial cartoon. No experimental data correspond to this plot and units are omitted.

an effective diffusive linear behavior:

$$MSD(t) = 4D_{eff}t \tag{5.6}$$

with an enhanced diffusion coefficient D_{eff} equal to

$$D_{eff} = D_0 + \frac{1}{4}\frac{l^2}{\tau}. \tag{5.7}$$

On the other hand, *at short time scales* ($t \ll \tau$), the expression (5.4) has the limiting form:

$$MSD(t) = 4D_0t + \frac{l^2}{\tau^2}t^2, \tag{5.8}$$

i.e., the motion is ballistic and the displacement is proportional to the swimming (or persistence) length l.

Fig.5.5(c) displays the experimental data obtained for $R = 2.13$ μm Janus particles dispersed in a 7 μm thick sample cell and illuminated at different laser intensities [115]. The plotted MSDs correspond to the trajectories presented in §5.2 (Fig.5.4(a)) and reported, for sake of clarity, next to each curve. The inset is nothing but the zoom of the black curve which, in turn, shows the displacement at $I = 0$ $nW\mu m^{-2}$ (Brownian particle). The dashed line are the fittings of the experimental data made with Eq. (5.4). As expected, high laser intensities lead to larger mean square displacements since the colloid becomes more and more "alive".

We first extracted D_0 from the linear fitting of the black curve (Eq. (5.5)) obtaining $D_0 = 0.031 \pm 0.006$ μm^2s^{-1}. Afterwards, we calculated the parameters τ (average persistence timescale) and l (persistence length) by fitting the data with (5.4). Finally, we derived the swimming speeds from the linear relation $l = v\tau$ and the effective diffusion from Eq. (5.7). The results are summarized in Tab. 5.1.

I ($nW\mu m^{-2}$)	τ (s)	v (nms^{-1})	l (μm)	D_{eff} (μm^2s^{-1})
0	–	–	–	0.031 ± 0.006
46	220 ± 20	46 ± 5	10 ± 2	0.147 ± 0.029
69	190 ± 20	85 ± 7	16 ± 3	0.370 ± 0.069
92	190 ± 20	175 ± 20	33 ± 8	1.49 ± 0.42
115	220 ± 30	265 ± 33	58 ± 14	3.89 ± 1.01
138	240 ± 40	310 ± 28	74 ± 13	5.80 ± 1.49
161	230 ± 40	360 ± 27	83 ± 12	7.48 ± 1.86

Table 5.1: Characterization of the self-propulsion of Janus colloids with radius $R = 2.13$ μm. Parameters obtained from the fitting of the measured MSD (Fig.5.5(c)). The errors correspond to standard deviations.
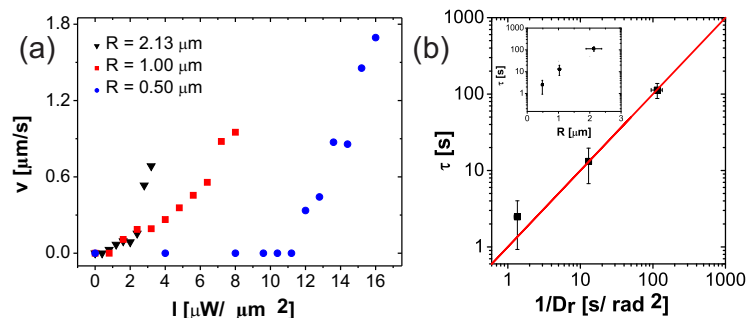
Figure 5.6: Swimming parameters for different particle's sizes [127]. (a) Velocity (v) of self-propelled Janus particles, with $R = 2.13$ (black), 1.0 (red) and 0.5 (blue) μm, as a function of the illumination intensity I. (b) Average persistence time τ plotted as a function of the rotational diffusion time $\tau_R = D_R^{-1}$ over two orders of magnitude. The inset shows τ plotted as a function of the particle radius. The error bars are obtained from the measurements at different I.

From Tab. 5.1 it becomes obvious that, as soon as the light intensity I is enough to trigger the decomposition of the binary mixture, l and v increase linearly with the I. In contrast, no significant variation of τ with I is observed. Hence, the typical transition from the ballistic to the diffusive regime does not depend on the strength of the propulsion. This observation was somehow expected since for an active Janus particle the average persistence time τ is given by the rotational diffusion which is unaffected by the driving force. In support of this argument, it's worth to notice that the value $\tau \approx 200$ s for which best agreement with the experimental data is obtained is close to the timescale of rotational diffusion $\tau_R = D_R^{-1}$. For a spherical colloid D_R is given by the following expression

$$D_R = \frac{3D_0}{4R^2} \tag{5.9}$$

which leads, for $R = 2.13$ μm, to $\tau_R = 188$ s. This value is indeed close to the experimental τ. We have therefore verified experimentally that for self-propelling Janus colloids the average persistence time is determined by the rotational diffusion. We also note that the decoupling of rotational and translational motion largely simplifies corresponding numerical simulations of the system.

5.4 Dependence on the particle's size

To investigate the effects of the particle's size on the propulsion, we made the same single particle experiment described in the former Sections with

67

gold-coated particles of different radii. The evaporated layer is again 20 nm thick but, instead of using a 7 μm cavity, we dispersed the colloid in a higher sample cell (100 μm). Due to gravity as well as to the rather weak swimming speeds (smaller than 2 $\mu m s^{-1}$), the active motion is still effectively constrained to two dimensions. However, some physical parameters (e.g., D_0) are not comparable with the results of §5.3 because of the influence of the glass slides over the particle's diffusion.

That being said, Fig.5.6(a) shows the swimming speed v as a function of the illumination intensity I for particles of different size ($R = 0.5$, 1.0 and 2.13 μm). The velocities v are calculated by fitting the MSDs as explained in §5.3. From the three curves becomes evident that there is always an intensity threshold below which v is approximately 0, i.e., the particle is simply Brownian. This threshold is motivated by the fact that, in order to see active motion, the illumination intensities has to be powerful enough to heat the liquid surrounding the gold coating above the critical temperature. The experimental data of Fig.5.6(a) suggest that the critical light intensity is larger for smaller colloids. This observation makes actually sense in view of the fact that big Janus particles provide a larger light-absorbing area (the gold-coated hemisphere) from which the heat propagates into the neighboring liquid (see also Fig.5.2). Once the particle becomes active, we again observe the linear increase of the swimming speed with the light intensity in agreement with the results of §5.3 (Tab.5.1).

We also checked the robustness of the equality between the average persistence time τ and the rotational diffusion time $\tau_R = D_R^{-1}$. It's worth to remark once more that the relation $\tau = \tau_R$ has a powerful meaning inasmuch as it implies that the sole rotational diffusion rules the persistency of the trajectories, no matter how "active" the particles are. The data summarized in Tab. 5.1 showed a good match for large particle ($R = 2.13$ μm). Fig.5.6(b) also includes the experimental τ for $R = 1.0$ and 0.5 μm and proves that the equality $\tau = \tau_R$ holds for smaller colloids either. Moreover, we again find no variation with the light intensity. Please note that the rotational diffusion time scales with R^3 (small particles reorients far more often), therefore Fig.5.6(b) covers a wide range of times.

5.5   Active motion in a light gradient

The possibility of tuning the active Brownian motion of the micro-swimmers can be employed in various contexts. For example, we harnessed the dependence of the swimming strength on the illumination intensity to investigate the behavior of a microswimmer in a spatial light gradient[3], where its swimming properties are space-dependent; these conditions resemble the situation

---

[3]It's important not to confuse the spatial light gradient (externally imposed) with the local concentration gradient (generated internally by the colloids).
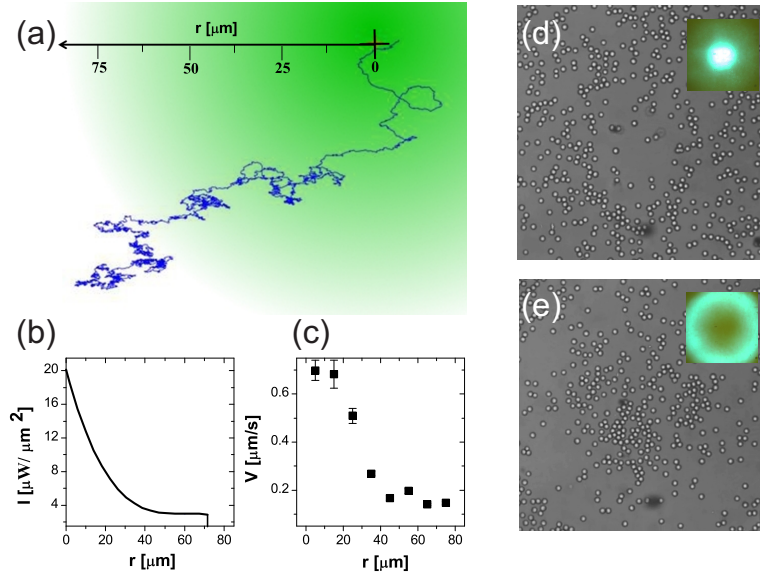
Figure 5.7: Motion of Janus particles in a light gradient [127]. (a) Trajectory of a self-propelled particle in a radial gradient. (b) Light intensity as a function of the radial position r. (c) Average swimming velocity v as a function of r. (d), (e) Density rearrangement of a self-propelled colloidal suspension (area fraction ≈ 0.1) in a radial (d) and in a concavity-like gradient (e). The insets show the defocused light patterns.

of bacteria moving inside a chemical gradient.

In §1.2 I highlighted that bacteria and cells have the ability of swimming up a food gradient (*chemotaxis*) in search of a more advantageous environment [7, 8, 137, 138, 139, 140]. In order to make this migration more effective, the persistence length is adjusted along the way, becoming longer and longer as the high concentration region is approached.

Our system of self-propelling colloids is powered by the green illumination rather than by nutrients profiles. We can therefore simulate the gradient of food by illuminating the sample with a radial gradient of light, illustrated in Fig.5.7(a) as a background and obtained exploiting the AODs of our setup (see §4.3.1).

Fig.5.7(a) also includes the trajectory of a microswimmer moving inside such gradient; the radial dependence of the intensity is depicted in Fig.5.7(b). The particle starts from the lower left corner, where, since there is almost no light, it undergoes standard Brownian motion. As soon as it randomly moves closer to the center, it starts to perform active Brownian motion with increasingly high v and l as it approaches the high-intensity center of the gradient; the radial dependence of v is plotted in Fig.5.7(c). The trajectory becomes more directed and less rough as the active motion increases. The blue curve in Fig.5.7(a) therefore resembles the motion of

biological swimmers inside food gradients, showing a continuous growth of its persistence length l. However, synthetic colloids are not equipped with chemotactic sensors and no effective migration is in average observed: the Janus colloids have the same chance to move towards or against the light gradient.

We finally checked how the concentration of a multiple particle suspension (area fraction $\phi \approx 0.1$) varies upon illumination with a radial light gradient. Fig.5.7(d) shows the distribution of the particles after the illumination (gradient shown in the inset) has been on for 5 minutes. The central region characterized by high intensities gets depleted since the particles are faster there. Likewise, if we reverse the gradient, i.e., if we use a concavity-like illumination such as the one in the inset of Fig.5.7(e), the colloids accumulates in the inner region (Fig.5.7(e)).

5.6   Summary

In conclusion, I presented a novel method to obtained Janus self-propelling colloids inside a critical binary mixture with a lower critical point. The propulsion is caused by self-diffusiophoretic forces when the fluid phase separates due to a local heating. The demixing occurs when the metallic coating of the particles is heated by green light. The internal driving can be easily tuned by controlling the illumination power given to the system.

I also showed that the active Brownian motion of the colloids is characterized by few key-parameters, i.e., the persistence length l and the average persistence time τ, which define the interplay between ballistic and diffusive behavior. Above a critical threshold needed to achieve the phase separation, l is directly proportional to the light intensity, whereas τ is independent of it and only given by the rotational diffusion time τ_R of the colloids.

Finally, I stressed this dependence of the swimming strength on the illumination intensity to investigate the behavior of a microswimmer in a spatial light gradient, where the swimming properties are space-dependent.

Chapter 6

Swimmers in confinements

In the very beginning of this thesis I highlighted that artificial microswimmers, such as Janus particles self-driven by phoretic forces, aimed at fulfilling two very broad goals. On one hand manmade microswimmers could be employed to transport and deliver drugs throughout the human body for medical treatments. Secondly, these autonomous motors are model systems used to emulate the active motion of more complex biological microorganisms like bacteria, cells or algae.

Either ways the motion of a single particle in bulk, described in the past Chapter, does not address realistic conditions. A microswimmers that navigates throughout human tissues does not deal with an environment free of obstacles: blood vessels, skin capillaries and porous membranes are only few examples of the rich structure of the human body. The typical sizes of these habitats go often down to the micro-metric scale affecting directly the basic features of the active motion of the swimmers.

Likewise, natural microswimmers, such as "run" and "tumble" bacteria, often move in patterned environments, e.g., inside the intestinal tract, which provides the natural ecosystem of *E. coli*, or during bioremediation, where chemotactic bacteria spread through porous polluted soils. Moreover, it's very unlikely to find these microorganisms isolated and sparse; bacteria and cells often gather in dense colonies because of confined geometries or in order to cooperate upon starvation conditions.

Due to the tunable properties of their driving mechanisms, the phoretic microswimmer I described in the former Chapter are a perfect tool to investigate these puzzling issues on a very fundamental level. With the help of lab-on-a-chip devices, we can in fact resemble complex events that would be tough to track otherwise.

This Chapter is divided in two main Sections: the first will be focused on the interaction between a single self-propelled colloid and some fixed obstacles whose size is comparable with the typical lengths of the active trajectory. Instead, the second part will address the topic of clusters formation

in dense active suspensions.

The numerical simulations of the multiple particle system, used to corroborate the experimental observations, have been made by T. Speck, J. Bialkè and H. Löwen at the Heinrich-Heine-Universität in Düsseldorf.

6.1 Microswimmers across confinements

6.1.1 Biological swimmers in confined geometries

Biological microswimmers, such as bacteria, are ubiquitous in our everyday life. Their active motion in bulk has been fairly understood during the past century thanks to the advances in video microscopy and micro-particle imaging; for instance, wild *E. coli* bacteria are known to undergo a "run" and "tumble" motion in search of nutrients (see also §1.2) [7, 8].

Very little is however known about their behavior in complex habitats, in spite of the fact that biological microswimmers live and proliferate in a wide range of environments presenting complex surfaces and obstacles [141]. The interaction of bacteria with surfaces is, for instance, the first stage towards the formation of biofilms [142]. Bacteria also play an important role in regulating the ecosystem of soils and rocks up to the point that they are often artificially spread over farmlands to remove pollutants (*bioremediation*) [143]. In addition, *E. coli* bacteria populate the membranes of the intestinal tract causing, sometimes, annoying infections [144].

All these environments are characterized by pores whose size is on the order of the typical persistence length of the bacterial active motion (few microns) [141]. A classical "run" and "tumble" trajectory (Fig.6.1(a)) is therefore constrained inside such porous materials and some directions are hindered by the presence of confinements (Fig.6.1(b)) [145].

Nevertheless, despite the relevance of these phenomena, systematic studies *in situ* not doable for practical reasons. The remarkable progresses in the field of lithography [126] has afforded the opportunity to reproduce in the laboratory the above-mentioned experimental condition by fabricating micron-sized constraining structures such as micro-channels or porous media.

Before examining the behavior of biological swimmers inside such complicated media, let us begin with the easiest form of confinement one can think of: flat straight wall. The 3D motion of an *E. coli* bacterium approaching and hitting a surface has been tracked in Ref. [108]. Fig.6.1(c) shows one of the recorded experimental trajectories: The bacterium collides against the substrate, changes its orientation and finally swarm along the surface until it moves eventually away. Hence, the swimmer maintains its persistency by sliding along the wall for a while after the collision. A similar result was obtained with bacteria confined in narrow (few microns wide)
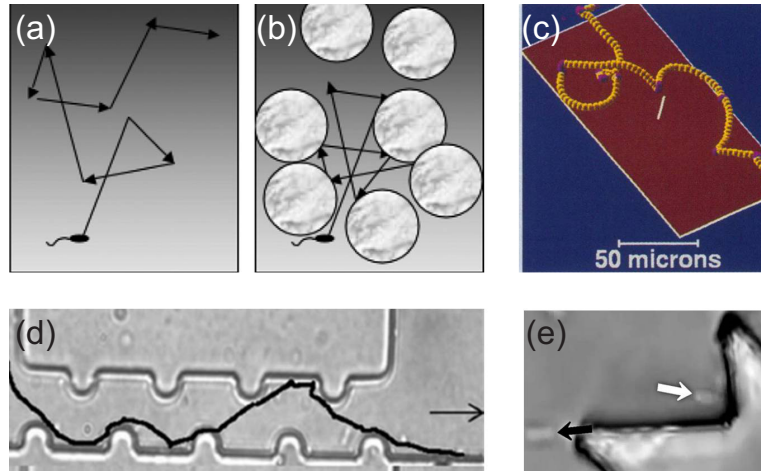
Figure 6.1: (a) Schematic representation of the bacterial "run" and "tumble" in a bulk system [145]. (b) Same as in (a) but in presence of porous grains [145] (c) 3D tracking of a wild type bacterium near the surface [108]. (d) Microswimmer moving inside a narrow microfluidic channel [146]. (e) Bacteria hitting (white arrow) and leaving (black arrow) a micro-fabricated gear. The collisions induce a clockwise rotation of the wheel [147].

channels (Fig.6.1(d)) [146]: As shown by the trajectory in Fig.6.1(d) the microswimmer moves parallel to the wall for some time before detaching. This interaction between biological swimmers and walls can be also exploited in several applications: for instance, the collisions of bacteria against gears (white arrow of Fig.6.1(e)) can power the rotation of micro-fabricated wheels [147].

The coupling between the active Brownian motion and surfaces is also essential to understand the behavior inside more complex environments such as porous media. Despite the importance of this issue in many fields, e.g., bioremediation, the literature still lacks a thorough knowledge as well as a robust theoretical background. I am only aware of few models that have been proposed on a rather phenomenological level [145, 148]. Although these model rather address the environmental engineering community, the basic idea behind them is tightly related with the experiments I am going to present in next Sections and, thus, deserves specific attention.

When a bacterium swims through a porous medium, the ratio between the typical distance d_{pore} that spaces apart the obstacles and the average persistence length l of the bacterial motion determines whether the active trajectory (Fig.6.1(a)) is affected or not by the presence of grains (Fig.6.1(b)). Ref. [145] suggests the emergence of three regimes.

1. If $l \ll d_{pore}$ the active motion is unaltered by the porous surrounding.

2. If $l \gg d_{pore}$, i.e., when the bacteria are propelled over distances much
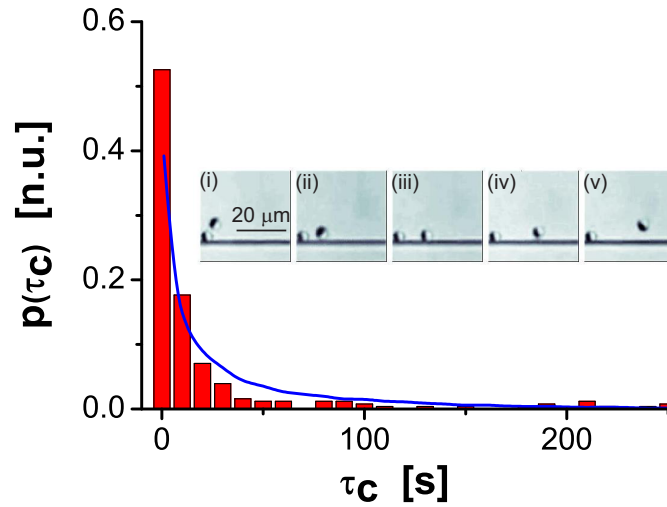
Figure 6.2: An encounter between a microswimmer and a wall. Experimentally measured (bars) distribution $p(\tau_c)$ of the contact time between a microswimmer and a wall ($I = 115 \, nW \, \mu m^{-2}$) for more than 250 encounter events. The line represents the result of a numerical simulation with L and τ_R taken from the experimental values. The insets are snapshots, taken at $t = 0$ (i), 0.7 (ii), 1.6 (iii), 2.8 (iv) and 3.6 (v) s, showing the approach, the contact and the detachment [115].

> larger that the average pore size, the long time effective diffusion D_{eff} (see §5.3) is essentially ruled by d_{pore}.

3. If $l \approx d_{pore}$, the behavior wobbles between the situations (1) and (2). In this case, the authors proposed a pragmatic way-out, i.e., to estimate the effective mobility as an harmonic average of the free-particle's and the strongly confined-particle's mobility.

In the oncoming Sections I will show how self-propelled particles can be employed to shine some light on the interaction between active trajectories and confinements.

6.1.2 Interaction of self-propelled colloids with walls

We use our self-propelled Janus particles (§5.1) driven by self-diffusiophoresis as model system to investigate how active Brownian motion (§5.2) is affected by the presence of more or less elaborated confinements.

By means of the classical lithography (see §4.2.1 for details) we directly imprint on the glass substrate a structure with the desired geometry. The colloidal suspension is then poured on the slide and sandwiched by a second glass in a sample cell 7 μm thick as extensively described in §4.2.1. We again use Janus colloids with radius $R = 2.13 \, \mu m$ half-coated with 20 nm of

Au. The colloidal suspension is very diluted in order to focus on the single particle behavior.

We first addressed the simplest form of confinement: a straight wall [115]. The insets of Fig.6.2 show the interaction with the wall of an active particle with persistence length $l = 58$ μm (corresponding laser intensity $I = 115$ $nW \mu m^{-2}$). First the particle approaches the wall (i) and gets in contact (ii). Then it slides along the surface (iii) until rotational diffusion realigns the particle so that its orientation vector **n** points away from the wall and leads to particle detachment (iv,v). Measuring the distribution of the particle-wall contact time τ_c for more than 250 encounters, we find a monotonic decrease as shown in Fig.6.2 (bars).

We also performed numerical Brownian dynamics simulations, where the motion of the Janus particle is modelled by a superposition of random diffusion and ballistic motion with velocity v. The parameters D_0 and v are taken to match the experimental values obtained in bulk (Tab. 5.1). The direction of v is determined by the free 3D diffusion of the particle's orientation. To account for the presence of confinements (top and bottom glass slides as well as the wall-like structure made of SU-8 and shown in the insets) the component of v perpendicular to the obstacles is set to zero. From the simulated particle trajectories we calculated the corresponding distribution $p(\tau_c)$ (blue line in Fig.6.2), which shows good agreement with the experimental data. In particular, in both cases the average τ_c is much smaller than τ_R due to the angular distribution of the incoming particle direction. This suggests that the particle-wall encounter mechanism is correctly described by this simple model and that the rotational diffusion remains largely unaffected by the proximity to the wall. We also note that, at least under our experimental condition, hydrodynamics effects (neglected in the simulations) are not needed to seize the particle-wall interaction.

We then decided to probe the coupling between the persistence length l of an active trajectory and the typical size of a pore by confining the particle in a circular cavity with radius $r = 38$ μm [115]. This approach follows the guidelines of Ref. [145] according to which the ratio between r and l determines to which amount a trajectory is affected by the confinement.

The experimental snapshot of Fig.6.3(a) qualitatively shows that a swimmer with $l > r$ keeps up with its persistency after the collision with the cavity's rim and, therefore, moves preferentially along the circular barrier. To elucidate more systematically this statement we repeated the experiment at different illumination intensities, i.e., with particles characterized by different persistence length. The red (experiments) and blue (simulations) lines of Figs.6.3(b-f) are typical trajectories when l is (b) 16, (c) 33, (d) 58, (e) 74 and (f) 83 μm, respectively. In Fig.6.3(b), the particle moves diffusively exploring all the pore uniformly, as a consequence of its ballistic length being much shorter than the pore characteristic length, i.e., $l = 16$ $\mu m \ll r$. Similar results hold for shorter l and in particular for a non-active Brownian
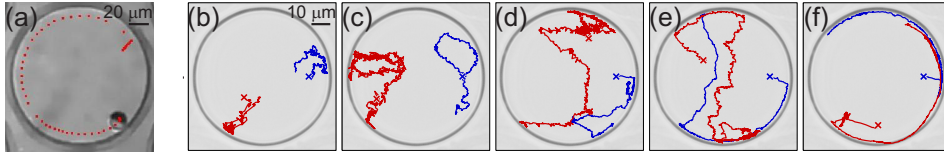
Figure 6.3: Microswimmers in a confined geometry. (a) Experimental snapshot displaying the trajectory (red dots) of an Janus particles inside a circular cavity. The persistence length l is larger than the diameter of the cavity. (b), (c), (d), (e) and (f) show measured (red lines) and simulated (blue lines) trajectory for for different illumination intensities corresponding to ballistic lengths (b) 16 μm, (c) 33 μm, (d) 58 μm, (e) 74 μm and (f) 83 μm. The radius r of the confinement is 38 μm. All trajectories were sampled over 600 s. [115].

particle for which l is due to the inertia of the particle and lays in the order of a few pm [149]. The chances that the particle encounters the cavity wall in one of its straight runs increase as l gets longer. Once the particle touches the wall, it starts sliding along the cavity perimeter until the rotational diffusion orients the cap towards the interior of the well, according with the process described in Fig.6.2. As expected, the probability of finding the particle at the confinement wall strongly increases when l is significantly larger than r, e.g., $l = 74$ μm (Fig.6.3(e)) and $l = 83$ μm (Fig.6.3(f)). As shown by the agreement between blue and red lines, experiments are well corroborated by numerical simulations. A similar behavior has been recently observed with *E. coli* confined in emulsion droplets: bacteria have indeed the tendency to move along the internal surface of the droplet[1].

6.1.3 Microswimmers in patterned environment

The interplay between the persistency of an active trajectory and the typical porous size can be exploited to design simple sorting devices. The strategies employed so far in order to sort out chemotactic bacteria is based on the creation of chemical gradients, which are obtained in turn through rather complicated microfluidic geometries [150, 151, 152, 153].

In the following paragraphs, we propose a novel device that allows us to sort our active self-propelled particles according to the properties of their motion, i.e., their persistence length l. To do so, we disperse the Janus particles inside a pattern of elliptical pillars, periodically arranged (Figs.6.4(a-e)) [115]. Again the periodic structure is imprinted on top of the glass substrate by means of classical lithography. The pillars are place in a triangular lattice and the lattice constant $L_c = 35$ μm defines the characteristic "pore size". Once more the persistence length l is adjusted by tuning the illumination power I injected into the system.
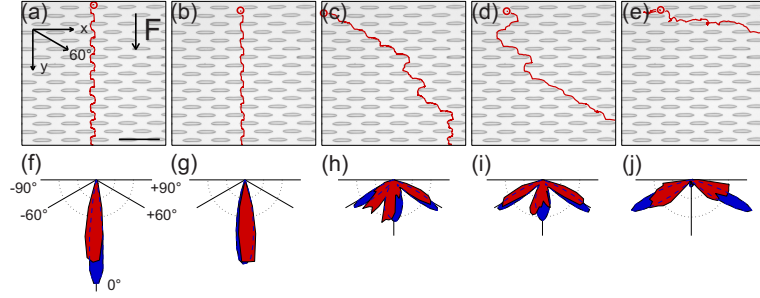
---

[1]Reference not available yet.

Figure 6.4: Microswimmers in a patterned environment. (a-e) Typical trajectories of self-propelled particles moving through a triangular lattice (lattice constant $L_c = 35\ \mu m$) of elliptical obstacles when a drift force $F = 0.12\ pN$ is applied along the y-direction. (a) Brownian particle (no propulsion), (b) $l = 16\ \mu m$, (c) $l = 24\ \mu m$, (d) $l = 33\ \mu m$ and (e) $l = 83\ \mu m$. (f-j) Corresponding histograms of the experimentally measured (red) and simulated (blue) directions of the particle trajectories as defined by two points in the trajectory separated by $100\ \mu m$. The experimental histograms were obtained considering more than 100 trajectories in each case. The parameters for the simulations are taken from the experimental values reported in Tab. 5.1 [115].

Within such structures, long swimming cycles are only possible along two main directions: at ± 60 and ± 90 degrees with respect to the y-axis. Otherwise the motion is strongly hindered due to collisions with the obstacles. This leads to strong differences in the particle trajectories depending on their swimming length. In the presence of an additionally applied drift force, this permits us to separate the microswimmers according to their swimming behavior. The drift force is obtained by employing Janus beads that are also paramagnetic and dragging them in the y-direction with a permanent magnet (Fig.6.4(a)). The magnet can be placed at different distances away from the sample to tune the strength of the drift force. We remark that this force is independent of the orientation of the particles because these are sufficiently isotropic.

We first consider a constant drift force $F = 0.12\ pN$; this value has been estimated from the average drift speed $v_d = 0.97\ \mu m s^{-1}$ of a Brownian particle ($I = 0\ nW \mu m^{-2}$). The typical trajectory of a Brownian particle is shown in Fig.6.4(a). Because of the Péclet number $Pe \approx 1000$, the effect of the diffusion is rather weak and the particle meanders almost deterministically through the structure in the direction of F.

For increasing swimming lengths (Figs.6.4(b-e), from left to right), however, significant changes in the shape of the trajectories are observed. This becomes particularly pronounced for $l > L_c$, where the particles perform swimming cycles of increasing length along the diagonal channels (Figs.6.4(c),
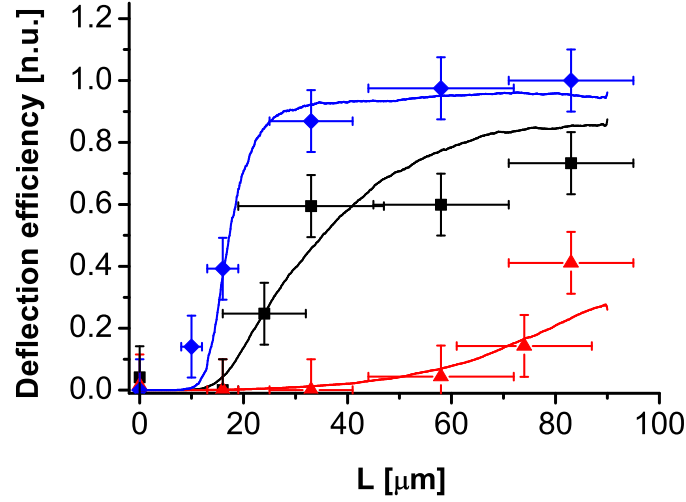
Figure 6.5: Deflection efficiency of microswimmers. Measured probability that particles are deflected by more than 30 degrees after a travelling length of 100 μm as a function of the swimming length l for various imposed magnetic drift forces $F = 0.06 \pm 0.02\ pN$ (diamonds), $0.12 \pm 0.05\ pN$ (squares) and 0.28 ± 0.12 pN (triangles). The solid lines are the results of numerical calculations. The experimental histograms were obtained considering more than 100 trajectories in each case. The parameters for the simulations are taken from the experimental values reported in Tab. 5.1. [115].

(d)). For $l = 83\ \mu m$ the propulsion becomes so strong that the particles partially move perpendicular to the drift force (Fig.6.4(e)); occasionally even motion against the drift force can be observed.

The particle motion through the structure is characterized by the direction (with respect to the y-axis) of the line connecting points of the trajectory separated by a distance of 100 μm. The probability distributions of these angles are shown by the red polar histograms in Figs.6.4(f-j). One clearly observes that with increasing l (again, from left to right) the propagation of particles along the direction of the applied drift becomes less likely, while trajectories along ± 60 degrees, i.e., along the directions that permit long swimming events, become more frequent. As shown in Fig.6.4(e), at very high illumination powers, i.e., when $l \gg L_c$, the swimmers manage to follow also the free channels at ± 90 degrees (with respect to the y-direction), "bending" the probability distribution towards angles larger than 60 degrees (Fig.6.4(j)). We again compared these results with numerical simulations (blue polar histograms in Figs.6.4(f-j)), which show good agreement with the experimental data.

With the additional possibility of varying the drift force by simply moving the magnet, these observations can be exploited to spatially separate self-propelled particles with small differences in their individual swimming

behavior. This is demonstrated in Fig.6.5, where we show the deflection effi-
ciency as a function of l, as defined by the probability that the mean particle
trajectory is deflected by more than 30 degrees after a travelling length of
100 μm. As symbols (lines) we have plotted experimental (simulation) data
obtained for different drift forces. The black data (squares) correspond to
$F = 0.12 \, pN$ (Fig.6.4). Here the deflection efficiency shows a strong increase
around $l \approx 30 \, \mu m$ and a flattening towards larger swimming lengths. The
blue (diamonds) and red (triangles) data are obtained for $F = 0.06$ and
$0.28 \, pN$, respectively, and demonstrate that the sorting efficiency strongly
responds to variations in F. Accordingly, the deflection (transmission) of
self-propelled particles while crossing a patterned structure can be easily
tuned by the appropriate choice of F.

In conclusion, the choice of a suitable pattern of obstacles is enough to
sort out microswimmers equipped with different persistence lengths, pro-
vided that a generic drift force is applied. Although for simplicity we used a
magnetic force, any other drift force could be applied, e.g., an electric field
or a solvent flow through the device.

6.2   Collective behavior of active suspensions

6.2.1   Clustering of active matter

As shown in §6.1 the motion of active objects is strongly altered by the
presence of confinements in its vicinity. So far, I have only discussed the
case of fixed obstacles, e.g., straight walls, circular cavities and arrays of
elliptical pillars. Nonetheless, microswimmers can also limit each other's
motion when dispersed in crowded suspensions: the collisions between the
swimmers play hereby a key-role and, together with other more complicated
interactions, strongly affect the collective behavior of the overall suspension.

The observation of collective phenomena involving "living active matter"
is as old as life itself. For instance, a naive glance up at the sky bestows
us with the spectacular view of graceful flocks (Fig.6.6(a)) that rearrange
ceaselessly [155]. Similar impressive phenomena occur in the seas (e.g.,
schools of fishes) and on solid ground (e.g., herds of sheep), alike. Down
to the micro-metric scale, bacteria are well-known to form colonies, such
as the one shown in Fig.6.6(b) [154], provided that the bacterial density is
large enough [156, 157, 158, 159, 160]. Colonization of surfaces is actually
the first step towards the growth of biofilms [161], although dense bacterial
solutions can also give birth to other appealing phenomena such as swarming
[162] or microbacterial turbulence [163]. Active clusters have been recently
observed also in suspension of colloids self-propelled by phoretic forces [73,
82]. Fig.6.6(c), e.g., shows the emergence of dynamic clusters in a rather
dense suspension (area fraction ≈ 0.1) of Pt-coated active colloids roaming
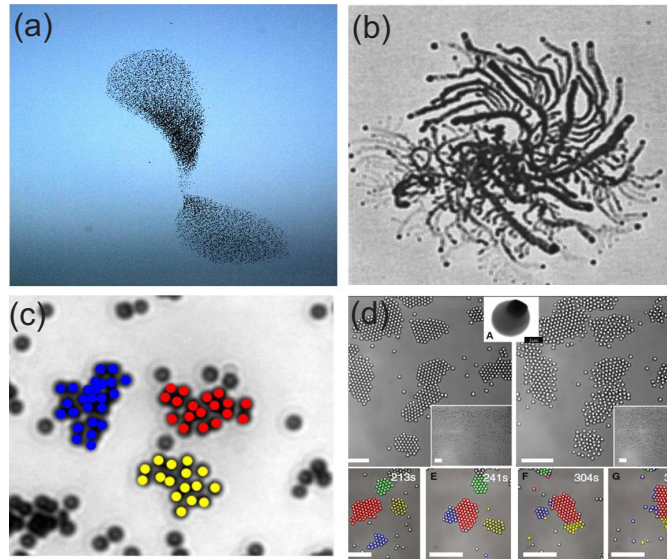
Figure 6.6: (a) A flock of starlings gracing the sky over Rome (picture taken from physicsword.com). (b) A typical colony of *Bacillus subtilis* bacteria [154]. (c) Dynamic clusters of sedimenting *Pt*-coated colloids. The particles are propelled by diffusiophoresis in an H_2O_2 solution [73]. (d) Living crystal of active surfers performing a 2D active Brownian motion onto a glass slide. The particles are propelled by diffusiophoresis in an H_2O_2 solution as long as illuminated by UV-light [82].

in an hydrogen peroxide solution (see §2.2.2) and undergoing sedimentation. Likewise, Fig.6.6(d) displays the formation of large dynamic aggregates, named "living crystals", in a 2D system of colloidal "surfers", equipped with a hematite cube that triggers the catalytic decomposition of H_2O_2 upon UV-illumination, thereby propelling the colloids by self-diffusiophoresis (see again §2.2.2 for details).

All the above-listed examples defy the physical intuition according to which the disorder increases with the temperature, i.e., with the noise. The most simple and paradigmatic example is the Ising model of interacting spins on a lattice, which, in two or more dimensions, displays a second-order phase transition from an ordered state to a disordered state as we raise the temperature [164]. Non-equilibrium driven systems, however, may show the opposite behavior [165, 166]: increasing the noise strength leads to the emergence of ordered states, e.g., flocks, colonies or clustering in general. As mentioned within Chapter 5 an active system can indeed be sketched, at large t, with an effective diffusion coefficient and, therefore, with an effective temperature: higher activities, given by high swimming velocities, correspond to larger T_{eff}, i.e., to noisier systems. Hence, the appearance of ordered aggregates (clusters) increasing, e.g., the swimming
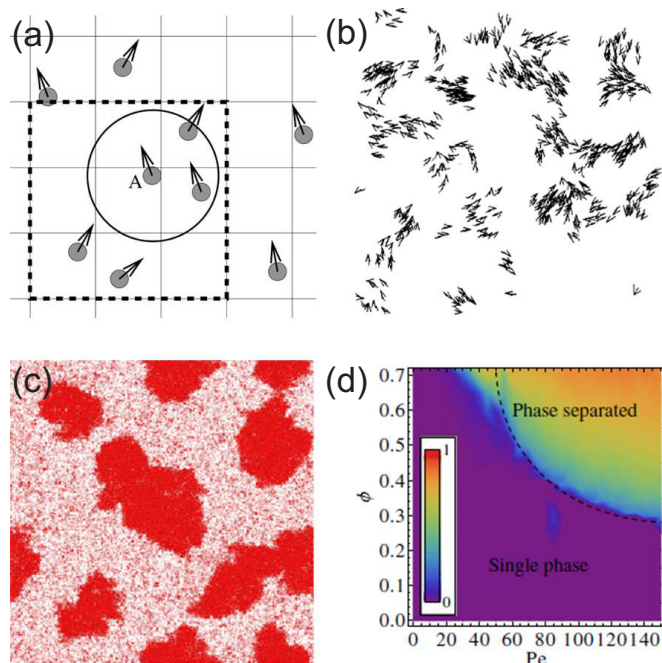
Figure 6.7: (a) Sketch of the Vicsek's model: a particle i undertakes the average orientation of the particles in its neighborhood $S(i)$, which can be either a circle or a square [168]. (b) Clusters formation, driven by the Vicsek's model, in system of self-propelled particles with an effective alignment. The arrows indicate the swimming velocities [162]. (c) Phase separated state obtained through numerical simulations of a suspension of self-propelled particles beyond the critical levels of activity and density [169]. (d) Phase diagram of a suspension of self-propelled particles plotted as a function of the Peclet number (activity) and the particles density. The dashed curve marks the approximate location of the binodal and the color bar indicates the degree of order [169].

speed is by all means an outstanding example of the so-called "freezing by heating" transitions [167].

What are the reasons behind the formation of clusters in non-equilibrium systems such as the ones shown in Figs.6.6(a-d)? The answer to this question is not ubiquitous and requires a deep understanding of the particular system under investigation. Nonetheless, in the past years theoreticians conceived few widespread models in the attempt of grasping the features that characterize all these out-of-equilibrium systems.

Clustering induced by alignments

The Vicsek's model is acknowledged as the benchmark to understand the collective motion of biological (or bio-inspired) organisms [168, 170]. This

model describes a system of identical active objects moving in the 2D space with a constant absolute speed v and subjected to a noise η of varying amplitude [170]. Thus, the control parameters of the simulations are the density ρ of active particles, the activity v and the strength of the noise term η. Moreover, a strong assumption is made: When the particle are close enough, they interact by changing their direction of motion, i.e., the system shows an effective alignment at short distances. If $S(i)$ is the neighborhood of the particle i where the interaction takes place (see Fig.6.7(a)), then the particle's orientation θ_i is derived from the average direction of the surrounding particles as follows [168]:

$$\theta_i(t + \Delta t) = \langle \theta(t) \rangle_{S(i)} + \xi \tag{6.1}$$

where ξ is the uncertainty determined by the noise amplitude η of the system. As shown in Fig.6.7(a) the neighborhood $S(i)$ of the simulation's lattice can be chosen either circular or squared without affecting qualitatively the results.

By implementing these simple assumptions in the simulations, Vicsek and coworkers found a non-equilibrium phase transition governed by the density and the activity of the system [162]. When the noise is not too large this transition occurs increasing the particle's density, i.e., higher ρ cause the formation of groups of particles that move together (see Fig.6.7(b)). In conclusion, due to the interaction shown in the Eq. (6.1), the active system gains order at high densities, i.e., when the particles happen to be often at close distances.

The hypothesis of an effective alignment is motivated by the behavior of organisms such as fishes (birds), which are known to assume the same orientation inside a school (flock). In colloidal systems the short-range alignment can be indirectly reproduced using rods [157, 171] or polar disks [172] interacting through volume exclusion.

Clustering induced by collisions

We note that, in the Vicsek's model, the noise annihilates the transition into ordered states. Surprisingly, a similar disorder-order transition has been recently predicted for active systems that are characterized by an increasing effective noise, instead. The effective noise (temperature) is given, as discussed above, by the activity (speed) of the particles: faster particles contribute to, effectively, noisier systems. Such transition does not require any assumption on the alignment. Therefore, even symmetrically shaped swimmers, like disks or spheres, can undergo the out-of-equilibrium phase separation. Specifically, simulations of a minimal model for a suspension of repulsive disks below the freezing transition [173] show phase separation into a dense large cluster and a dilute gas phase [174, 169]. Phase separation

due to a density-dependent mobility has been discussed theoretically in the context of run-and-tumble bacteria [175], and a link has been made recently to self-propelled Brownian particles [176].

The idea behind the aggregation of active particle in the absence of any alignment relies on a simple self-trapping mechanism. Since the orientation of the driving varies continuously according to the rotational diffusion, swimmers colliding head-on cannot free themselves until the rotational diffusion reorients the direction of the propulsion. This implies that, if the particles density and the swimming speed allow the swimmers to collide often enough, the clusters can grow up to the complete phase separation of the sample[2].

For instance, in Refs. [174, 169] the non-equilibrium phase transition of self-propelled disks is discussed. The disks are purely repulsive and supplied with both a rotational and a translational white noise. The self-propulsion is implemented by adding a constant speed whose orientation is governed by the free rotational diffusion. Above some critical densities and activities (velocities), the disks meet often enough to trap each others inside one or few large clusters. In fact, by the time a particle located at the rim of a cluster is redirecting its driving outwards, a new swimmer pushing inwards has joined the aggregate. Activity and particles density work jointly in this phase separating process, i.e., larger densities (activities) need smaller activities (densities) to produce a similar effect on the dynamics.

The results of this self-trapping mechanism are shown in Fig.6.7(c-d). If the parameters v and ρ are large enough to trap the swimmers inside a cluster accordingly to the description given above, the particles gather in very big aggregates as shown in Fig.6.7(c). These clusters are then predicted to slowly merge into one final large cluster surrounded by diluted gas phase of free particles. The separation occurs thereby via coarsening. Nevertheless, a phase transition via nucleation and growth may also happen upon a shallow quenching [169, 177][3]. The non-equilibrium phase transition is described by a phase diagram (Fig.6.7(d)) which is similar to that of a suspension of attractive colloids in equilibrium. The phase separation is indeed depicted by a binodal curve with the Peclet number Pe (i.e., the swimming speed) and the particles density ρ as control parameters [169]. In particular above a critical density the diagram of Fig.6.7(d) settles the minimum velocity required to reach the phase separated region. This critical activity becomes smaller and smaller at higher densities in agreement with the collision argument introduced above.

---

[2]I will take up again this self-trapping mechanism in the following Sections, where our experimental findings are discussed.

[3]A full interpretation of the dynamics of the phase separation is work-in-progress [169, 177].
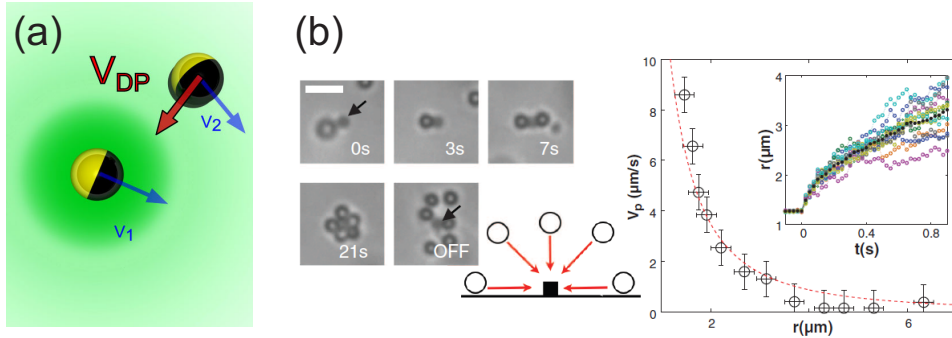
Figure 6.8: (a) Cartoon portraying the origin of phoretic attractions. v_1 and v_2 are the propulsion speeds. v_{DP} is the drift velocity of particle 2 caused by the gradient of particle 1 [73]. (b) Experimental measurement of the phoretic attractions caused by local gradient of H_2O_2 [82]. (Left) Snapshots showing the phoretic drift of tracer particles towards the catalytic source of hematite. (Right) Radial velocity V_p from the ensemble average of the tracer drift (inset, black symbols). The r^{-2} scaling agrees with the predictions for phoretic attractions.

Clustering induced by effective attractions

The assumption of purely repulsive swimmers might be unrealistic in several colloidal systems. In §4.1.2 I highlighted that colloids with a mutual attraction can show clustering and phase separation even in equilibrium [119, 120, 121]. Typically an aggregation is observable for attractions larger than $k_B T$. The strength of the mutual attractive potential can be minimized below this critical level with a clever choice of the colloidal beads. For instance, I showed that the replacement of the metallic coating of a Janus particle with a carbon layer leads to weaker Van der Waals attractions between the capped hemispheres (refer again to §4.1.2 for a detailed explanation).

Nonetheless, phoretic swimmers, such as the ones used as model systems in this manuscript, possess an additional source of attraction that is fully related to the driving mechanism. Let us consider two phoretic swimmers that move close to each other as shown in Fig.6.8(a) [73]. The propellers are constantly surrounded by their self-generated gradient that in turn powers the propulsion. The swimming speeds v_1 and v_2 are proportional to the strength of the corresponding gradients with a pre-factor that stands for the phoretic mobility (see Eq. (2.2) of §2.1). When the two particle are sufficiently close for their gradients to overlap, each swimmer responds not only to its own gradient but also to the one of the neighboring particle. Therefore, in addition to the propulsion, each swimmer feels a phoretic drift v_{DP} that leads to an effective attraction. The adjective "effective" emphasizes the fact that the drift pops in only when the particles are active (no gradient

would be there otherwise), i.e., when the system is out-of-equilibrium.

A similar effective attraction, induced by local overlapping gradients, has been predicted [178, 179] and subsequently observed [180, 181] in the context of chemotactic bacteria. In analogy with the phoretic propellers, bacteria respond to food gradients with a directed motion (chemotaxis) as extensively discussed in §1.2. Likewise, a bacterium creates in its local surrounding gradients of nutrients that can be chemotactically sensed by a second microorganism passing by.

Back to the phoretic propellers, although the mutual phoretic attraction characterizes any multiple particles system where a propeller generates its own gradient, the existence of this force has been experimentally proved for diffusiophoretic swimmers, which originate a local solute concentration gradient ∇c [73, 82]. For a net production/absorption of c per object, the c-field gradient was shown to decay as r^{-2} [182].

This theoretical prediction has been recently verified using catalytic swimmers immersed in an H_2O_2 aqueous solution (see also §2.2.2). The gradient is hereby given by the concentration of H_2O_2 that is continuously consumed/produced by the self-propelling colloids. In particular, Palacci and coworkers witnessed a quadratic behavior of the velocity of tracer colloids approaching a catalytic source [82]. This striking experiment is illustrated in Fig.6.8(b). In short, an hematite cube is embedded to a glass substrate and few colloidal tracers are dispersed around it. Under illumination with UV light the hematite acts as catalyst for the decomposition of H_2O_2, thus generating a concentration gradient in its vicinity. The profile of the gradient is then mapped by the motion of the tracers that are naturally attracted by the cube because of diffusiophoretic forces. The snapshots of Fig.6.8(b) (left) clearly show that the phoretic attraction is large enough to induce a drift towards the catalytic source. Likewise, the velocity of the colloids, plotted in Fig.6.8(b) (right) as function of the distance from the hematite cube, confirms the r^{-2} behavior expected for phoretic attractions.

Ergo, phoretic attraction can be responsible for the aggregation of self-propelling colloids [73, 82, 183].

We note that, since the phoretic attractive force appears if and only if the particles are active, it is hard to disentangle, without a careful preliminary check, the (effective) attraction-driven aggregation from the one that could be caused by the collisions. Although these two effects may lead to the same result, i.e., the clustering, it is worth underline that they are conceptually very different. Only the latter is in fact a purely dynamical effect. Unfortunately, in active suspensions of phoretic particles these two phenomena always appear in pair and it is thus up to the researcher to sort out which of them is contributing to the aggregation the most. As a general remark, a significative clustering induced by collisions usually requires large

particles densities (area fractions $\phi > 0.2$) , whereas clusters induced by phoretic attractions have been also observed at smaller densities [73, 82].

Very recently Baskaran *et al.* computed the full phase diagram of self-propelled particles featuring a mutual attraction as well [184]. This remarkable work in my opinion clarifies the competition/cohoperation of the two mechanisms responsible for the aggregation: the *self-trapping*, i.e., the collisions between the active colloids, and the *attractive forces*, such as the phoretic sensing. Three regimes are basically found:

- When the attractions are large and the activity (swimming speed) small the colloidal suspension phase separates as though it would do in equilibrium. The suspension forms gels that can arrest or slowly coarsen towards the complete phase transition.

- Increasing the propulsion, the activity annihilates the phase transition. The colloids now have the ability to escape from the cluster preventing them from merging.

- When the activity is large compared to the attractive potential the self-trapping mechanisms comes into play restoring the phase transition, although the latter is now triggered by the out-of-equilibrium dynamics of the particles rather than by attractive forces.

In summary, the phase diagram of this complex system is reentrant and affords some guidelines to tackle the issue of clustering of colloids that are both attractive and self-propelling. As I will show later, in contrast with Refs. [73, 82] where the aggregation is driven by (phoretic) attractions, we decided to work experimentally in a regime where the self-trapping dominates over the effective phoretic drift.

Last but not least, the numerical simulations presented so far do not take into account hydrodynamic interactions between the active colloids. Nevertheless, hydrodynamics is a feature that an experimental suspension of colloid always contains: When a particle navigates through a liquid, the surrounding flow field is altered by the motion. Therefore, two bodies that swim in the same region necessarily show a more or less pronounced interaction due to the superimposition of the respective flows.

The issue of the flow field produced by a single swimmers was successfully investigated during the past decade; as emphasized in §3.3 it is now understood that the flow surrounding a microswimmer can show either a r^{-2} (dipoles) or a r^{-3} decay depending on the driving mechanism. In particular, phoretic propellers belong to the second category and are often alternatively addressed as *squirmers*.

Nevertheless, the influence of hydrodynamic interaction on the collective behavior of active suspension remains an open topic. Very recent simulations
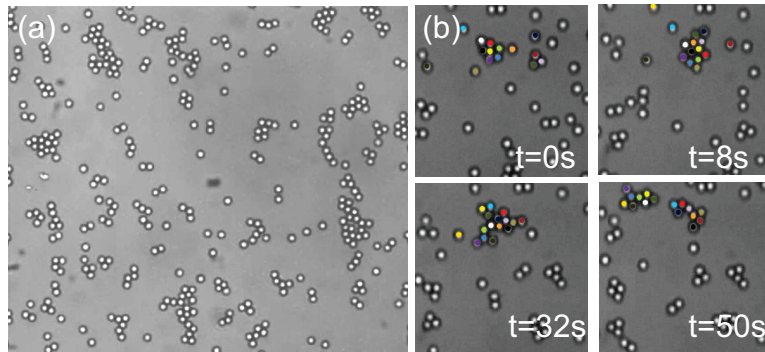
Figure 6.9: Clustering of self-propelled colloids at low densities. (a) Experimental snapshot for speed $v \approx 1.51$ μms^{-1} and area fraction $\phi \approx 0.1$. (b) Dynamical clustering of self-propelled colloidal particles at low densities ($\phi \approx 0.1$ and $v \approx 1.51$ μms^{-1}). Shown is the formation and breaking up of one cluster. Every particle that at one time has been a member of the cluster is colored differently [125].

(not yet published) show that the rotational diffusion is greatly enhanced in dense suspensions of pushers, i.e., dipoles propelled with a rear motor [185]. Further simulations reported the same increase of D_r in suspension of self-propelling colloids (squirmers) either [186]. The enhancement of D_r is expected to suppress the phase separation destroying the self-trapping mechanism: faster reorientations allow a colloid to leave a cluster before a new swimmer joins the aggregate. Other numerical simulations, that include the far-field hydrodynamics as well as the lubrication forces, showed the opposite effect: hydrodynamic interactions seem to facilitate the aggregation of the colloids [187].

I will show in the next Section that we do not observe experimentally a faster orientational diffusion of particles belonging to a cluster; D_r appears rather unaffected by the presence of neighboring swimmers under our experimental conditions.

In conclusion, it is fair to claim that the role of hydrodynamics in active dense suspension is still wrapped in mystery.

6.2.2 Experimental observation of clustering

From §6.2.1 we learnt that clustering in a dense suspension of self-propelled colloids might be a consequence of three main effects: alignment, collisions and attractions. The latter includes also the so-called "effective" attractions, i.e., attractive forces (e.g., phoretic sensing) that are present only when the colloids are active. None of these effects excludes the others.

We carefully designed a system of self-propelling particles that interact only through collision, thus behaving, to a first approximation, as hard spheres [125]. I will demonstrate throughout this Section that the other two
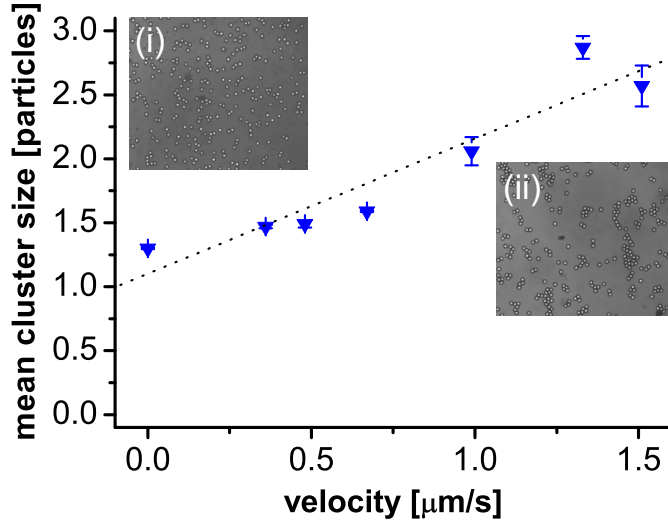
Figure 6.10: Mean cluster size at low densities ($\phi \approx 0.1$). Average number of particles per cluster plotted for different swimming velocities. The mean cluster size increases linearly as a function of speed v. The dashed line is the fit $1.1 + 1.1v$. Error bars indicate the statistical uncertainty. Each statistical error is estimated by splitting the data into 3 samples and calculating the standard deviation of the means. The insets show the experimental snapshots at (i) $v \approx 0.36\ \mu m s^{-1}$ and (ii) $v \approx 1.51\ \mu m s^{-1}$ [125].

mechanisms of clustering are negligible or even absent.

Janus particles are again prepared from SiO_2 beads with a radius of $R = 2.13\ \mu m$ by sputtering a thin layer ($10\ nm$) of graphite onto one hemisphere. These carbon-coated particles are then suspended in a water-2,6-lutidine mixture close to the critical concentration (0.28 mass lutidine) and a small amount of suspension is poured in a $400 \times 400\ \mu m^2$ cavity made by photolithography of SU-8 photoresist on a glass surface (please refer to §4.2.1 for the details about the sample preparation). The 2D area fraction ϕ is tuned up to 0.4 by adjusting the concentration of the initial suspension. The sample is finally sealed with a cover glass on top. Since the height of the cavity is about $6\ \mu m$, the motion of the particles is confined in 2D (albeit particles may move out of plane and slightly overlap in the recorded images). The spheres remain however free to rotate in 3D. The laser light is absorbed by the carbon-coated hemisphere which locally heats up the binary mixture above the critical temperature. The colloids are therefore propelled by self-diffusiophoresis as extensively described in Chapter 5.

In the following, the control parameters are the area fraction (or 2D particles density) ϕ and the laser intensity. In order to estimate the swimming speed v in dense suspensions for a given intensity, we determine the trajectories of isolated particles and fit their short-time mean-square displacement
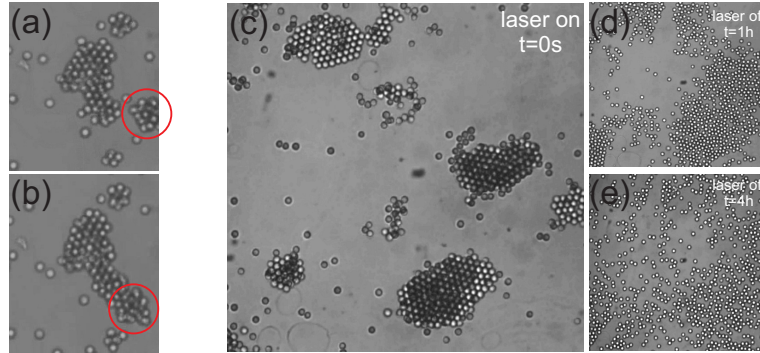
Figure 6.11: Phase transition of an active suspension at high densities. (a-b) Snapshots extracted from a movie showing two large clusters merging after collision. One of them is marked with a red circle. The area fraction and the swimming velocity are 0.25 and 1.45 $\mu m s^{-1}$, respectively. (c) Phase separated stage of an active suspension at $\phi \approx 0.27$ and $v \approx 1.63~\mu m s^{-1}$. Particles slightly out of focus appear darker than the others. The aggregation is completely reversible: The snapshots (d-e) show how the clusters dissolve after the illumination has been turned off. After 4 hours (e) the suspension looks homogenous as it was before turning on the illumination [125].

to the expansion $4D_0 t + (vt)^2$ of Eq. (5.4), where $D_0 = 0.029~\mu m^2 s^{-1}$ is the bare diffusion coefficient in equilibrium. The long-time effective diffusion does obviously not fit with Eq. (5.4): at large t the colloids collide more and more often, whereas (5.4) has been derived for free particles.

Under equilibrium conditions, i.e., with the illumination turned off, we observe a homogeneous suspension at all studied area fractions $\phi \approx 0.1-0.4$. After turning on the illumination, the particles are driven out of thermal equilibrium and are propelled along their orientation. We let the system relax into a steady state (for about 15 minutes) and then analyze trajectories with a length of about 5 minutes. We estimate cluster sizes through the enclosed area since within larger clusters it becomes difficult to reliably detect particle positions.

At low densities (e.g., $\phi \approx 0.1$), the system rapidly enters a steady state that can be described as a dynamical cluster fluid (Fig.6.9(a)), i.e., the suspension is characterized by small aggregates that, however, do not grow beyond a certain size. Fig.6.9(b) shows the temporal evolution of a small cluster. Each particle belonging at one to the cluster is marked with a different color. The sequence of snapshots clearly demonstrates that the aggregation is dynamical, i.e., particles join and leave the cluster, until in the last snapshot the cluster has finally broken into two smaller aggregates. Furthermore, we note that the mean cluster size (Fig.6.10), i.e., the average number of particles belonging to a cluster, increases approximately linearly as a function of the propulsion speed similar to what has been observed by

Theurkauff *et al.* [73]. Higher activities determine in fact larger probabilities of mutual collisions. The more often the colloids collide against each other, the larger is the typical size of the clusters.

At higher densities ($\phi > 0.2$), we observe a phase separation where clusters grow until the system consists of a few big aggregates surrounded by a dilute gas phase. The clusters continuously expand in size changing their shape and acquiring more and more particles. Averaged-sized clusters coarsen into a larger aggregate as soon as they get in touch. The coarsening mechanism is illustrated in Fig.(a) and (b): the cluster marked with a red circle mingles with the neighboring aggregate right after the collision. We presume that the final stage is the condensation into one final cluster. However, the slow dynamic of the large aggregates puts the direct observation of this final stage out of our current reach.

Therefore, we report experimentally for the first time a transition a transition from the initially disordered, homogeneous fluid into an ordered state driven by the change (increase) the swimming speed. The ordered state is comprised of a few big clusters surrounded by a dilute phase of single self-propelled particles (see Fig.6.2.2(c)). These clusters are once more not static but they constantly change their shape while particles are exchanged between the cluster and the diluted phase. Moreover, clustering occurs only when the laser light is turned on and thus is fully related to the activity. Figs.6.2.2(d-e) shows the temporal evolution of the suspension in Fig.6.2.2(c) after we turn off the illumination. The particle diffusion restores in this case the homogeneous density profile, indicating that also for large clusters the aggregation is reversible and solely induced by the propulsion of the colloidal particles.

To identify the phase transition, i.e., the emergence of an ordered state, we plot in Fig.6.12 a geometrical order parameter P for different values of ϕ and v. In particular, we evaluate the average number of particles in the largest cluster normalized by the total number of particles in the field of view, i.e.

$$P = \frac{\langle N_{lc} \rangle}{N} \qquad (6.2)$$

We actually add together the size of all clusters larger than $N/10$ particles since we expect all big clusters to finally merge. In fact, when the sample undergoes a phase transition, we only observe the coalescence of smaller clusters and not that a larger cluster breaks up.

When the active suspension is not dense enough ($\phi \approx 0.1$, blue circles) a cluster fluid phase is observed increasing the activity, but no phase transition is reported at any of the accessible swimming speeds. The suspension remains into the disordered state ($P \ll 1$) no matter how fast the colloids are. On the other hand a phase transition into an ordered state is found at larger densities ($\phi > 0.18$) and is confirmed by a rapid increase of P towards
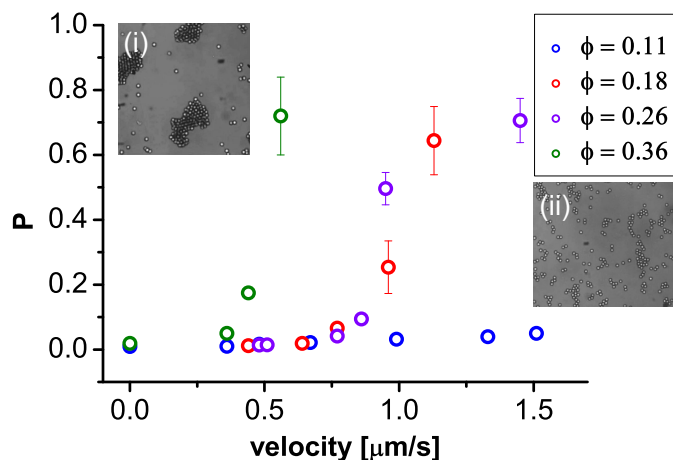
Figure 6.12: Disorder-order phase transition induced by the particles activity. Experimental relative mean size P of the largest cluster as a function of swimming speed v for $\phi = 0.11$ (blue), 0.18 (red), 0.26 (purple) and 0.36 (green). The inset show experimental snapshots of (i) a phase separated sample ($\phi \approx 0.25$ and $v \approx 1.45 \ \mu m s^{-1}$) and (ii) a (non-phase separated) cluster fluid phase ($v \approx 1.51 \ \mu m s^{-1}$ and $\phi \approx 0.1$) [125].

the unit (red, purple and green circles). In particular, the phase transition is achieved increasing the driving strength v beyond a critical value that depends, in turn, on ϕ. Larger densities undergo a phase transition at smaller activities: for instance, the active suspension at $\phi = 0.36$ (green) jumps into the ordered state at velocities that are approximately half compared to the ones found at $\phi = 0.26$ (purple). As a side remark, the order parameter P seems to ramp up with continuity, suggesting a phase transition of the 2nd order.

What is the mechanism of cluster formation? In the previous Section I highlighted the three main effects that contribute to the clustering in active suspensions of colloids propelled by self-generated phoretic forces: alignment, attraction (static and effective) and collision. Let us carefully check the role of each in our experimental system.

Clustering due to **alignments** is motivated by the Vicsek's model and occurs when the active particles have the same orientational order inside a large aggregate. In colloidal systems this usually happens with particles whose shape is somewhat asymmetric. The typical example are rods [157, 171] which, due to steric collisions, naturally assume a nematic configuration when densely packed. In the case of spherical colloids, such as the ones employed in this work, an effective alignment could be caused by hydrodynamics interactions or by short-ranged attraction between the coated hemispheres of the particles. Short-ranged interaction would have
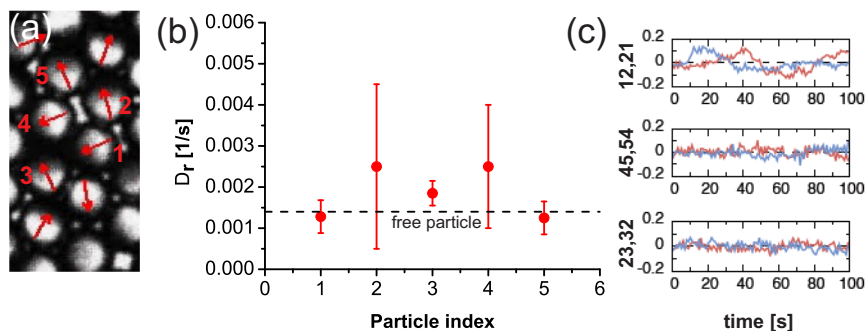
Figure 6.13: The absence of alignment inside large clusters. (a) Snapshot of the colloidal suspension. The measured projected orientations are marked by red arrows. The index of the particles that we have analyzed is labelled. (b) Estimated apparent rotational diffusion coefficient as a function of the particle index. The dashed line shows the estimated diffusion coefficient $3D_0/(2R)^2$ of a free particle. (c) Off-diagonal elements of the correlations $\rho_{ij}(t)$ for three particle pairs [125].

two distinguishable consequences: a systematic alignment of the swimming velocities and a change of the rotational diffusion in dense environments.

We do not observe the alignment of orientations. To address the above-mentioned issues in more detail we analyzed the orientations of few particles that are constrained inside a big active cluster. In particular, we prepared a dense sample of larger active particles with radius $R = 3.88~\mu m$ at illumination intensity $1.88~\mu W \mu m^{-2}$, which is comparable to the typical illumination powers employed in all the other measurements. In order to investigate the orientation for enough time we hold the active cluster in a concave cavity.

A first glimpse of the experimental snapshot in Fig.6.13(a) suggests that the angles are indeed oriented randomly. Unfortunately, we cannot resolve the full orientation of the particles. For a more quantitative analysis we have instead recorded, for the labelled particles, the projected angle $\varphi_i(t)$ with a time resolution of $1~s$. From the time series we estimate the angular velocity as

$$\dot{\varphi}_i(t) \approx \varphi_i(t+1) - \varphi_i(t). \tag{6.3}$$

The correlations as a function of time difference are thus given by

$$\sigma_{ij}^2(t) = \frac{1}{K} \sum_{k=0}^{K-1} \dot{\varphi}_i(k)\dot{\varphi}_j(k+t) \tag{6.4}$$

From these correlations we can extract a rough estimate $D_r \approx 1/2\sigma_{ii}^2(0)$ (Fig.6.13(b)) for the rotational diffusion coefficient for particle i. Error bars are estimated as the variance when splitting the data into three sets. Also shown is the rotational diffusion coefficient for a free particle $D_r =$

92

$3D_0/(2R)^2 \approx 1.3 \times 10^{-3} \ s^{-1}$ employing the no-slip boundary condition as appropriate for colloidal particles.

We find that the estimated rotational diffusion coefficients are reasonably close to that of a free particle. Particles 2 and 4 seem to rotate faster but also their statistical error is much larger. For an explanation note that we are only able to measure the projected angle φ whereas the particle rotates in three dimensions described by spherical coordinates φ and θ. For free rotation the stochastic equation read [188]:

$$\dot{\varphi} = \frac{\xi_\varphi}{sin(\theta)} \quad , \langle \xi_\varphi(t)\xi_\varphi(t') \rangle = 2D_r\delta(t - t') \qquad (6.5)$$

and

$$\dot{\theta} = \frac{1}{tan(\theta)} + \xi_\theta \quad , \langle \xi_\theta(t)\xi_\theta(t') \rangle = 2D_r\delta(t - t'). \qquad (6.6)$$

Our estimate for Dr is only accurate for $\theta \approx \pi/2$, i.e., the orientation of the particle is parallel to the top and bottom slides of the cell. If the orientation has moved out of this plane it will appear to rotate faster, which explains the data for particles 2 and 4.

To check for possible correlations, i.e., for evidence of mutual alignments, we calculate the normalized correlation coefficients ρ_{ij} between the generic particles i and j as

$$\rho_{ij}(t) = \frac{\sigma_{ij}^2(t)}{\sigma_{ii}(0)\sigma_{jj}(0)}. \qquad (6.7)$$

The resulting cross-correlations are plotted in Fig.6.13(c) for 3 pairs of particles: For particles 2 and 3 (bottom panel) as well as 4 and 5 (center panel), which are neighbors but with a larger separation, no correlations are found. Moreover, $\rho_{ij}(0) \approx 0$ for all particle pairs. There are, however, systematic oscillations for the neighboring particles 1 and 2 (top panel) in response to an earlier motion of the other particle.

The picture that emerges from this data is that there is no systematic alignment of particle orientations, which justifies their neglecting in the minimal model. However, some interactions are present especially at small particle separations.

A second possible reason for the clusters formation is the presence of **attractive forces**. We have first examined the role of *static attractions* that act independently of the activity of the colloids and are mainly due to van der Waals forces. In §4.1.2 I highlighted that the choice of the carbon coating largely reduce the attractions due to van der Waals forces between the colloids. We have verified that comparing with numerical results the experimental pair correlation function of a non-active suspension of Janus colloids with area fraction $\phi \approx 0.37$. Good agreement between experiment and simulations is achieved by adding a small attraction $(0.5k_BT)$ in the simulations (see Fig.4.2(e) of §4.1.2). Nonetheless, this value is small enough to
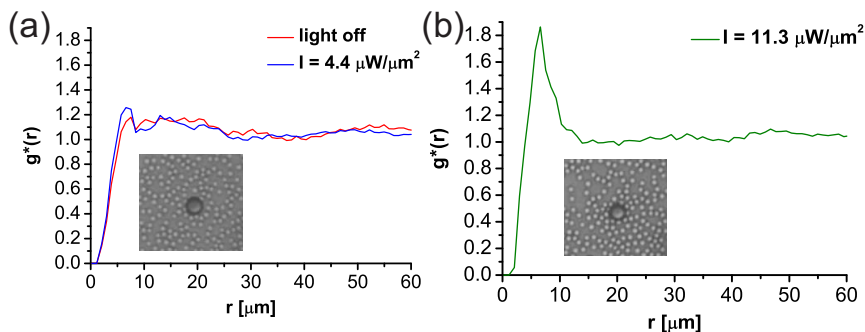
Figure 6.14: Experimental test for the strength of phoretic mutual drift. Pair distribution function of passive tracer particles in the presence of an active coated Janus particle fixed at the origin. (a) Without illumination and at moderate illumination intensity 4.4 $\mu W \mu m^{-2}$. (b) At high illumination intensity 111.3 $\mu W \mu m^{-2}$. The inset are the experimental snapshots taken at the end of the measurement [125].

exclude the static attraction as main mechanism of clustering. In addition, I've shown in Figs.6.2.2(c-e) that even large aggregates break off once the laser light is turned off. This observation pleads for a minor role of static attractions in the clusters formation.

Anyways, colloids propelled by self-phoresis experience further attractive contribute known as chemotactic sensing, i.e., a phoretic drift triggered by the overlap of the self-generated concentration gradients. These attraction are present only when the particles are active. As discussed in §6.2.1 active clusters driven by these kind of *effective attractions* have been recently reported in dense suspensions of patchy colloids propelled by the local decomposition of H_2O_2 [73, 82]. The strength and the range of the effective attraction are given by the size of the local concentration gradient weighted by the particle's mobility; since the surrounding gradient is directly related to the swimming speed (see Eq. (2.2)), the phoretic drift strongly depends on the activity: higher swimming velocities imply larger effective attractions.

In our experiments the propulsion force is due to a local demixing of the solvent (water)-molecular solute (lutidine) mixture. As first qualitative argument that phoretic interactions are weak, I stressed in §5.1 that the demixing zone is generally so small that cannot even be imaged with the microscope; we can thus naivly exclude chemotaxis as a possible long-ranged phoretic force. Other possibilities include hydrodynamic interactions and effective short-ranged interactions of the demixing zones.

To verify the presence/absence of significant phoretic effective attractions between the self-propelled colloids we have performed an experiment similar in spirit to the one described in Fig.6.8(b) [82]. To this end we have prepared a cell containing a suspension of passive tracer particles with radius $R = 1.3 \ \mu m$ and a few coated Janus particles with radius $R = 4 \ \mu m$. The

94
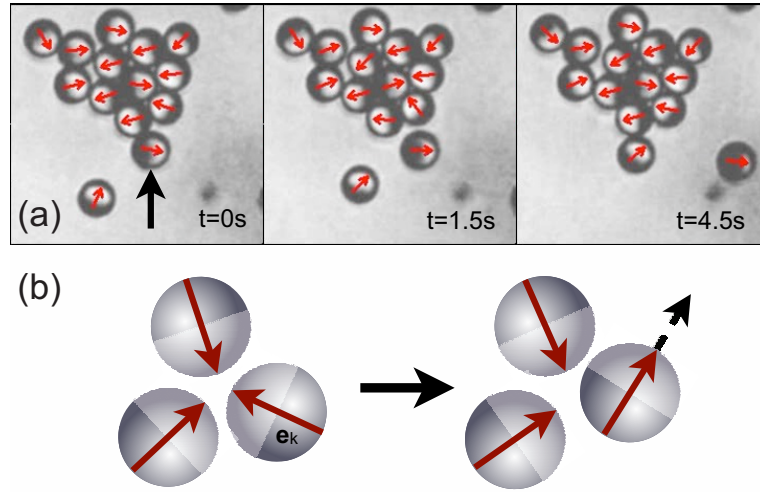
Figure 6.15: The self-trapping mechanism. (a) Consecutive close-ups of a cluster, where we resolve the projected orientations (arrows) of the caps. Particles along the rim mostly point inwards. The snapshots show how the indicated particle towards the bottom (left) leaves the cluster (center) and is replaced by another particle (right). (b) Sketch of the self-trapping mechanism: for colliding particles to become free, they have to wait for their orientations to change due to rotational diffusion and to point outwards [125].

area fraction of the passive particles is $\phi = 0.3$. We identified a region of the sample where by chance one of the coated particles sticks to the surface. To study whether attractive forces between active and passive particles occur, we then calculate the pair distribution function $g^*(r)$ of the passive particles with the active coated particle at the origin (Figs.6.14(a-b)). We have investigated three situations: illumination turned off (Fig.6.14(a), red line), illumination with moderate intensity 4.4 $\mu W \mu m^{-2}$ (Fig.6.14(a), blue line), and with high intensity 11.3 $\mu W \mu m^{-2}$ (Fig.6.14(b)). The swimming speeds measured using the method described in the main text are $v \approx 1.4~\mu m s^{-1}$ and $v \approx 9~\mu m s^{-1}$, respectively. Note that the maximal intensity used to gather the data presented in this Chapter is 5 $\mu W \mu m^{-2}$.

At high laser power we do indeed observe an aggregation of passive particles around the immobile coated particle indicating an effective phoretic attraction. However, at the lower laser power, corresponding to the actual experiments, we do not see any aggregation. We thus conclude that, at least for the illumination intensities used, the phoretic attractive forces can be neglected.

We rather ascribe the clustering shown in Figs.6.9 and 6.2.2 to a **self-trapping** mechanism caused by the collisions between particles equipped with a persistency. Particles that by chance bump against each other do not

free themselves immediately owing to the persistence of their orientations. To confirm experimentally this argument, we repeated the experiments using larger particles with radius $R = 4\,\mu m$, which allow us to resolve the caps and thus the projected orientations of particles (dynamics is also much slower, which is why for measurements we have employed smaller particles).

Fig.6.15(a) shows consecutive snapshots of a single cluster. Note that the orientations along the rim mostly point inwards. One particle with an outward orientation leaves the cluster while another particle attaches. The emerging physical picture is thus that of a simple self-trapping mechanism, see Fig.6.15(b): Two or more particles that collide head-on are blocked due to the persistence of their orientations. Hence, a particle situated in the rim of the cluster has to wait a time $\sim D_r^{-1}$ until rotational diffusion points its orientation outward to become free again. While the time to leave the cluster is independent of the swimming speed v, a larger swimming speed implies a larger probability for other particles to collide with the cluster, leading to its growth. The size of clusters is determined by the flux balance of incoming and outgoing particles. When the incoming flux is much larger than outgoing one the suspension phase separates (Fig.6.2.2) since the cluster do do longer have enough time to dissolve.

A deeper comparison with the results obtained in Refs. [73, 82] yields the following further important remarks.

- Clustering driven by attractions is expected to occur already at rather low area fractions. This prediction is confirmed by the experimental results at $\phi < 0.1$ of Refs. [73, 82]. On the other hand, our active suspension requires larger ϕ to show a relevant aggregation, in qualitative agreement with the phase diagram predicted for repulsive active colloids [169].

- We observe that, if the phase transition takes place, large clusters do not break-up, whereas in Refs. [73, 82] the aggregates only grow up to a characteristic size. In my view this substantial difference can be framed in the general theoretical description given by Baskaran *et al.* [184]. When the clustering is induced by attractions, as in Refs. [73, 82], the additional activity destabilizes the aggregates preventing the complete growth. In our case the clustering is caused by collisions and therefore clusters inevitably coarsen if the incoming flux of particles, determined by v and ϕ, dominates over the outgoing one.

6.2.3   Comparison with a minimal model

The robustness of our experimental discoveries (active clustering and phase transition) is corroborated by numerical simulations of purely repulsive disks performed by Thomas Speck *et al.* at the Heinrich-Heine-Universität in

Düsseldorf [125, 189]. In this Section I am going to summarize the benchmarks of the theoretical model; I will not focus on the details of the numerical simulations for which the reader can refer to Ref. [189]. Instead, I will underline the hypothesis behind the model and the experimental features that are not fully seized due to the bareness of these assumptions.

The instability that leads to the phase separation of an active suspension can be foreshadowed theoretically solving the many body Smoluchowski equation (6.8) for the joint probability distribution $\psi(\mathbf{r}_k, \varphi_k, t)$.

$$\partial_t \psi = \sum_{k=1}^{N} \nabla_k \cdot [(\nabla_k U) - f\mathbf{e}_k + T\nabla_k]\psi + D_r \sum_{k=1}^{N} \frac{\partial^2 \psi}{\partial \varphi_k^2}. \qquad (6.8)$$

The integration of (6.8) yields an equation for the projected density of a single particle ρ_1 that reads:

$$\partial_t \rho_1 = -\nabla \cdot [\mathbf{F} + f\mathbf{e}\rho_1 - T\nabla\rho_1] + D_r \partial_\varphi^2 \rho_1, \qquad (6.9)$$

where $\mathbf{F}$ is the force exerted by the surrounding onto the target particle and is a function of the two-body density distribution ρ_2 to find a particle at $\mathbf{r}'$ together with the tagged particle at $\mathbf{r}$ with orientation φ.

The closure of Eq. (6.9) is achieved noting that the force $\mathbf{F}$ can be decomposed along the driving force and density gradient, i.e.:

$$\mathbf{F} \approx -\zeta\bar{\rho}\mathbf{e}\rho_1 - (D_{eff} - T)\nabla\rho_1 \qquad (6.10)$$

where ζ is the effective force due to the neighboring particles. Hence, Eq. (6.9) for the single particle density is finally rewritten as

$$\partial_t \rho_1 = -\nabla \cdot [v_{eff}\mathbf{e} - D\nabla] + D_r \partial_\varphi^2 \rho_1, \qquad (6.11)$$

where the effective speed v_{eff} is the results of the propulsion mediated by the average density of the suspension, i.e.

$$v_{eff} \equiv f - \zeta\bar{\rho}. \qquad (6.12)$$

The solution of (6.11) shows a dynamical instability within a range of effective forces with limits ζ_+ and ζ_-. Hence, since ζ depends on both the mean particles density $\bar{\rho}$ and the activity f of the single particles, the phase separation is predicted to occur within very precise boundaries. In other words, the swimmers need to be fast and dense enough to undergo a out-of-equilibrium transition. This theory is in qualitative agreement with the experiments shown in §6.2.2.

In order to contextualize the experiments into the theory described above, the Düsseldorf's group has performed Brownian dynamics simulations. The experimental active suspension is sketched using disks that freely rotate in the 2D-plane. Although the experimental particles undergo a 3D

rotation, the 2D rotational diffusion coefficient is matched, for simplicity, with the experimental $D_r = 3D_0/(2R)^2$, where $R = 2.13\ \mu m$ and $D_0 = 0.029$ $\mu m^2 s^{-1}$ are again the particle's radius and the free translational diffusion coefficient, respectively. The activity is implemented supplying each particle k with a constant force f whose orientation $\mathbf{e}_k$ varies according to the rotational diffusion of the angle φ_k. Thus, the coupled equations of motions are:

$$\dot{r}_k = -\nabla_k U + f\mathbf{e}_k + \xi_k \qquad (6.13)$$

where ξ_k is the Gaussian noise and U is the total potential energy derived from the pair potential $u(r)$ as

$$U = \sum_{k<k'} u(|\mathbf{r}_k - \mathbf{r}_{k'}|). \qquad (6.14)$$

The pair interaction is adjusted to fit some experimental features. In particular, as shown in Fig.6.2.2(c), particles slightly overlap; we account for this (apparent) softness in the simulations, by picking the following pair potential:

$$u(r) = \begin{cases} \varepsilon u_{LJ}(r) + u_{\mathrm{LJ}}(2R)(\lambda - \varepsilon) & (r \le 2R) \\ \lambda u_{LJ}(r) & (r > 2R) \end{cases} \qquad (6.15)$$

with Lennard-Jones potential $u_{LJ}(r) = 4[(\sigma/r)^{12} - (\sigma/r)^6]$. λ is the depth of the attractive tail. The parameters ε and σ are fixed such that the potential minimum coincides with the particle diameter $2R$. As repeatedly stressed in §6.2.2 and 4.1.2, the best agreement between experiment and simulations is achieved by adding a small attraction with $\lambda = 0.5k_B T$; however, we focused on the purely repulsive pair potential with $\lambda = 0$ to show that, conceptually, the observed clustering does not depend on attractions.

The results of the simulations are shown in Fig.6.16. In the simulations clusters are determined from a simple overlap criterion: all particles with a separation smaller than their diameter share a "bond". A cluster is then the set of all particles that are mutually bonded.

The simulation outcomes, illustrated in Fig.6.16(a), demonstrate that a purely repulsive pair potential is sufficient to reproduce at $\phi = 0.3$ the increase of the mean cluster size with swimming speed. We remark that the data displayed in Fig.6.16(a) are obtained at ϕ where the phase transition does not occur yet. However, comparing with Fig.6.9(a), the increase of the cluster size is somewhat stronger in the experiments. The low-density snapshots of the simulations (Fig.6.16(b)) and experiments [Figs.6.9(a)] reveal another difference: while in the simulations a few large clusters dominate, the experimental snapshots show many clusters containing fewer particles.

Likewise, the numerical simulations seize the disorder-order phase transition as ϕ increases. Above a ϕ threshold, the ordered state is again achieved
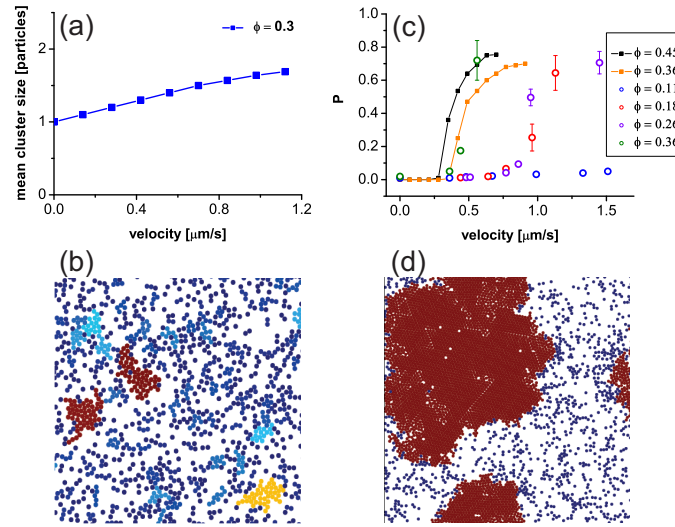
Figure 6.16: Clustering and phase separation in the numerical simulations. (a) Mean cluster size as a function of swimming speed v in a region where no phase separation occurs ($\phi = 0.3$). (b) Snapshot for $\phi = 0.3$ and speed $Pe = 140$ (corresponding to $v = 0.95 \; \mu m s^{-1}$). (c) Simulations results (closed symbols) compared with the experimental ones (open symbols). The experimental data are the same as shown in Fig.6.12. (d) Simulation snapshot of the separated system at $\phi = 0.5$ and speed $Pe = 100$ [125].

increasing the driving. Contrary to the experiments, where the dynamics is too slow to observe the coalescence of very large aggregates, the simulation are run for enough time to actually observe the formation of one final large cluster (Fig.6.16(d)). The order parameter P (closed symbols) is shown in Fig.6.16(c) alongside the experimental data (open symbols) already reported in Fig.6.12. The qualitative behavior of P is the same in both cases. When v crosses a critical value, P increases rapidly suggesting that an ordered state is reached. Increasing ϕ the transition takes place at lower v. However, the clustering seems to be more pronounced in the experiments, i.e., the transition occurs at lower densities ($\phi \approx 0.2$) whereas no phase separation is noted below $\phi \approx 0.4$ in the simulations. For the highest experimental density $\phi \approx 0.36$, the critical speed agrees quite well with the simulations.

In conclusion, numerical simulation and experiments show a very good qualitative agreement and both capture the main features of clustering and non-equilibrium phase transition of self-propelled colloids. Nonetheless, experimental results are shifted towards a situation with "more clustering". If we reason about the origin of such discrepancy, three main points immediately emerge.

1. The numerical simulation neglect any effect caused by hydrodynamics,

which is obviously present in the experimental system. In §6.2.1 we have seen that hydrodynamics certainly has an effect on the clustering, even though its precise influence is rather unclear.

2. The simulation are performed using purely repulsive disks. Instead, the colloids used in the experiment experience a weak attraction that we quantified around $0.5k_BT$. Although this attraction is too feeble to induce alone any clustering, it certainly helps in stabilizing aggregated that form due to self-trapping. Therefore, small attractions could definitely explain the observed disagreement.

3. The experimental system is quasi-2D, i.e., albeit the translational motion happens on the glass substrate, the particles rotate in 3D. When the orientation points up (or down) the driving force is blocked by the glass slides of the sample cell and the colloid behave as it were Brownian. The consequence of this "apparent passiveness" are not fully understood: on one hand it seems easier to trap particles if they become slower but, on the other hand, the driving force for the phase separation also becomes smaller. For sure, a mismatch with a purely 2D system (simulation) is not surprising.

4. Particles trapped inside a cluster are very packed. For the reason we expect that the demixing region of a swimmer located inside a cluster could be reduced by the presence of neighboring particles. This effect would effectively lead to weaker phoretic driving forces, providing thereby a possible qualitative argument for the higher clustering observed experimentally. In fact, slower swimmers do not break the clusters as effectively as the swifter ones.

6.3   Summary

The behavior of self-propelled particles or, more in general, active objects inside complex environments is definitely an appealing topic. The persistency these swimmers are equipped with leads to phenomenological effects that do not appear in classical Brownian suspensions. Confinements indeed tremendously modify the active motion and are therefore far more important for active systems than for Brownian ones.

In this Chapter, I have discussed two shining example: the confinement caused by fixed obstacles and the one induced by collisions in a dense active suspension. In the first case we have found that, when the persistence length of the active motion is sufficiently long compared to the typical distance between the obstacles, the active particles tend to spend more time by the confinement walls than their Brownian counterparts. This behavior can be exploited to implement novel sorting, classification and dialysis techniques

acting on the swimming style of the particles. In the second example, we have demonstrated that the self-trapping of particle with a persistency leads to the emergence of dynamical clusters that can eventually grow up to a compete phase transition into an ordered state.

Chapter 7

Asymmetric swimmers

The experimental results I have discussed so far address the particular case of phoretic swimmers whose shape is spherical, ergo, perfectly symmetric. The propulsion drives the particle straight and any reorientation is due to the rotational diffusion alone. These artificial micro-motors are often employed to understand and resemble the active motion of more complex biological swimmers as bacteria, cells or algae. However, biological microorganisms are often far from being symmetric. Simple rotationally symmetric shapes, e.g., spheres, provide thus only a crude approximation.

In the particular case of asymmetric propellers where the driving force is no longer applied on the center of mass, an active torque is induced alongside the driving perturbing significantly the swimming path. In this Chapter I will show that this perturbation results in a characteristic circular motion. We model a front-rear asymmetry by fabricating patchy L-shaped particles, coated on the short arm, which are by construction asymmetric around their propulsion axis. These asymmetric self-propelled particles perform a circular motion whose curvature radius is independent of the propulsion strength. Furthermore, the motion of asymmetric particles in lateral confinement reveals a fascinating novel feature, i.e., a critical contact angle that determines a switch from a stable sliding along the wall to a reflection.

I wish to acknowledge Felix Kümmel who made the experiments summarized in this Chapter. I will also present some numerical simulations done by B. ten Hagen, R. Wittkowski and H. Löwen at the Heinrich-Heine-Universität in Düsseldorf.

7.1   Circular motion of L-shaped active particles

Spherical active colloids undergo a persistent motion that recalls the behavior of several biological organisms (see §1.2). The typical example, discussed more than once throughout the manuscript, is the "run" and "tumble" trajectory of *E.coli* bacteria [7]. In short, such trajectories are the consequence
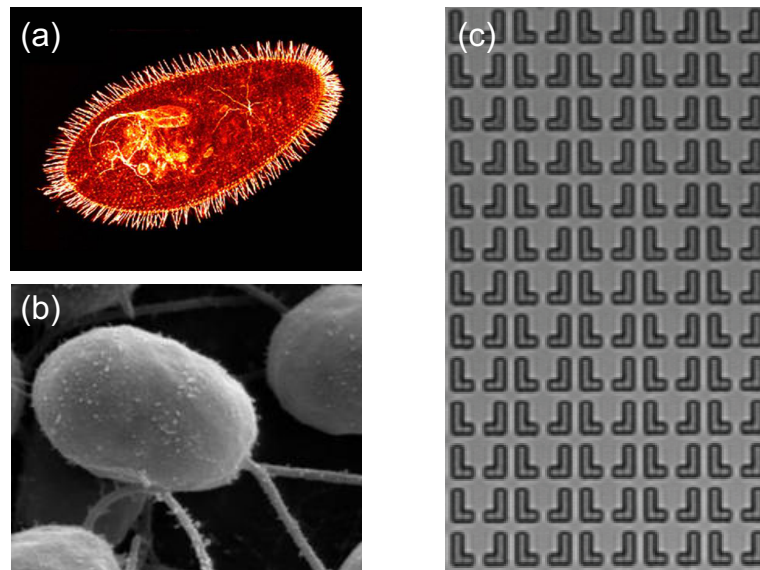
Figure 7.1: (a) The bean-like shape of the *Paramecium*'s body (picture taken from http://boomerblog.sdsu.edu). The external surface is clothed with short filaments (cilia) that pull the body forward with synchronized whip-like beating. (a) Example of a front-rear asymmetry in a *Chlamydomonas reinhardtii* (picture taken from Wikipedia). This alga is pulled by the two flagella embedded in the front of its body. (c) Microscope image of L-shaped particles laying on the silicon wafer after the lithographic process.

of a propulsive force that reorients randomly with a fixed tumbling rate. As highlighted in §5.3 the features of this motion are reproduced pretty well by the active motion of self-propelled particles. The equivalent of the tumbling rate is hereby the free rotational diffusion of the colloids.

Nevertheless, sometimes the approximation of a biological microswimmer with a sphere is too daring. Biological microorganisms possess often a shape that is stretched or deformed in one or more direction. In particular, the shape of a swimmer remarkably affects the active motion when the asymmetry develops around the propulsion axis (front-rear asymmetry).

Figs.7.1(a-b) illustrate microscopic images of a *Paramecium* and a *Chlamydomonas reinhardtii*, respectively. The first is a relatively large cell (dozens of microns) that is propelled by the synchronous beating of cilia attached to the body; the second is a green alga that swims thanks to the whip-like strokes of its two front flagella. Anyways, from both Figures appears clear that the body of the organism has a side fatter than the other reminding somehow the shape of a bean.

To reproduce artificially the front-rear asymmetry that characterizes some biological swimmers, we have replaced the spherical colloids described in Chapter 5 with L-shaped particles fabricated from photoresist SU-8 by

Figure 7.2: (a),(b) Trajectories of an (a) L+ and (b) L- swimmer for an illumination intensity of 7.5 $\mu W \mu m^2$. (Red) bullet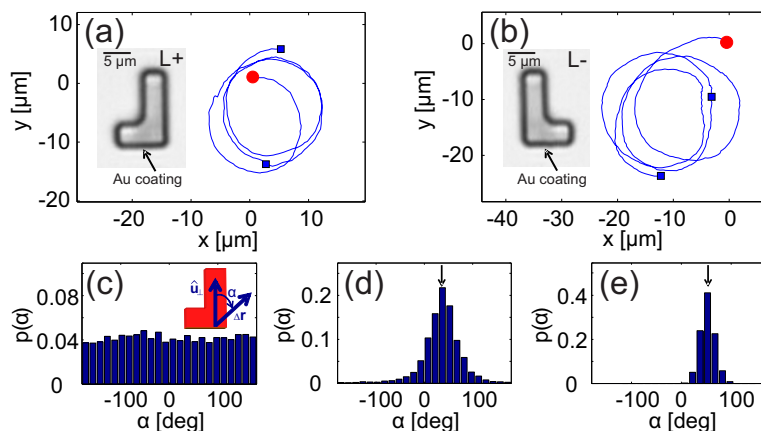s and (blue) square symbols correspond to initial particle positions and those after 1 min each, respectively. The insets show microscope images of two different swimmers with the Au coating (not visible in the bright-field image) indicated by an arrow. (c),(d),(e) Probability distributions $p(\alpha)$ of the angle α [see inset in (c)] between the normal vector $\mathbf{u}_\perp$ of the metal coating and the displacement vector $\triangle \mathbf{r}$ of an L+ particle in time intervals of 12 s each for illumination intensities (c) $I = 0$ $\mu W \mu m^{-2}$, (d) 5 $\mu W \mu m^{-2}$ and (e) 7.5 $\mu W \mu m^{-2}$ [190].

photolithography [190]. The details of the fabrication of particles made of SU-8 with different shapes can be found in Ref. [191]. In short, a 2.5 μm thick layer of SU-8 is spin coated onto a silicon wafer, soft baked for 80 s at 95 degrees and then exposed to ultraviolet light through a photomask. After a post-exposure bake at 95 degrees for 140 s the entire wafer with the attached particles is coated with a 20 nm thick Au layer by thermal evaporation. When the wafer is tilted to approximately 90 degrees relative to the evaporation source, the Au is selectively deposited at the front side of the short arms. A sacrificial layer is added beneath the SU-8 layer in order to remove the particles from the wafer (Fig.(c)) once the lithographic printing is made. The insets of Figs.7.2(a,b) show microscope images of the two configurations of L-particles used, denoted as L+ (left) and L- (right).

Once removed from the wafer, the particles are finally diluted in the critical binary mixture of water-2,6-lutidine and propelled according to the mechanism thoroughly described in §5.1. To confine the particle's motion to two dimensions, the suspension is contained in a sealed sample cell with 7 μm height. The particles are localized above the lower wall at an average height of about 100 nm due to the presence of electrostatic and gravitational forces. Under these conditions, they cannot rotate between the two configurations shown in Figs. 7.2(a) and 7.2(b).

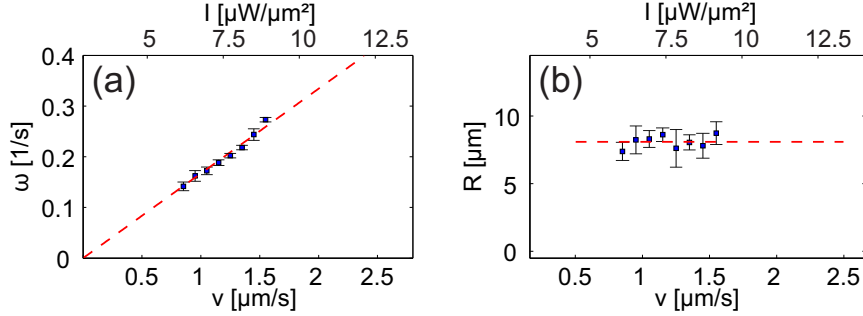Figs.7.2(a) and 7.2(b) also show the trajectories of L+ and L- swimmers

Figure 7.3: (a) Angular velocity ω and (b) radius R of the circular motion of an L+ swimmer plotted as functions of the linear velocity v and the illumination intensity $I \sim v$. The dashed lines correspond to a linear fit with nonzero and zero slope, respectively [190].

obtained by digital video microscopy for an illumination intensity of 7.5 $\mu W \mu m^{-2}$, which corresponds to a mean propulsion speed of 1.25 $\mu m s^{-1}$. In contrast to spherical swimmers, here a pronounced circular motion with clockwise (L+) and counterclockwise (L-) direction of rotation is observed. For the characterization of trajectories we determined the center-of-mass position $\mathbf{r}(t) \equiv (x(t), y(t))$ and the normalized orientation vector $\mathbf{u}_\perp$ of the particles (see inset of Fig.7.2(c)). From this, we derived the angle α between the displacement vector $\triangle \mathbf{r}$ and the particle's body orientation $\mathbf{u}_\perp$. Figs.7.2(c-e) show how the normalized probability distribution $p(\alpha)$ changes with increasing illumination intensity I. In the case of pure Brownian motion (see Fig.7.2(c)) $p(\alpha) \approx const$ since the orientational and translational degrees of freedom are decoupled when only random forces are acting on the particle.

In the presence of a propulsion force which is constant in the body frame of the particle, however, the translational and rotational motion of an asymmetric particle are coupled. This leads to a peaked behavior of $p(\alpha)$ as shown in Figs.7.2(d) and (e). The peak's half-width decreases with increasing illumination intensity since the contribution of the Brownian motion is more and more dominated by the propulsive part. In addition, the peaks are shifted to positive (negative) values for a particle swimming in a (counter)clockwise direction. The position of the peak is given by $\alpha = \pi \Delta t / \tau$, where τ is the intensity-dependent cycle duration of the circle swimmer and Δt is the considered time interval. This estimate (see arrows in Figs.7.2(d,e)) is in good agreement with the experimental data. The shift of the maximum of $p(\alpha)$ documents a torque responsible for the observed circular motion of such asymmetric swimmers. In contrast to an externally applied constant torque [192], here it is due to viscous forces acting on the self-propelling particle.

The internal nature of the torque is supported by the experimental observation of the particle's angular velocity: $\omega(t) = d\alpha/dt$ strongly depends
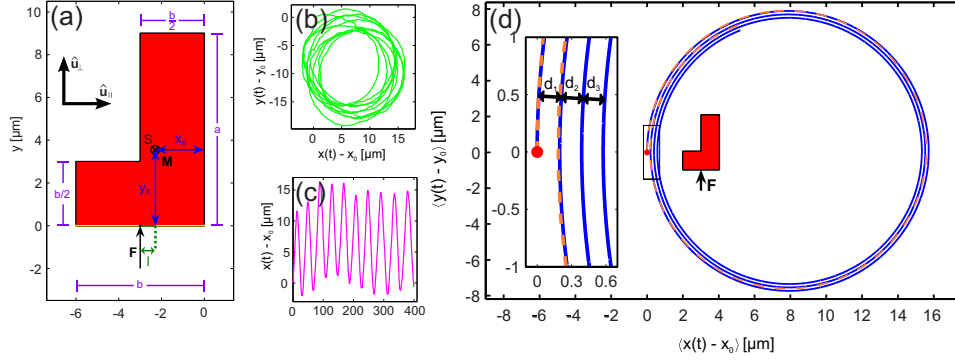
105

Figure 7.4: Geometrical sketch of an ideal L+ swimmer as considered in our model. The dimensions are a $a = 9~\mu m$, $b = 6~\mu m$, $x_S = 2.29~\mu m$, and $y_S = 3.55~\mu m$ (for homogeneous mass density and an additional $20~nm$ thick Au layer). The internal force $\mathbf{F}$ induces a torque $\mathbf{M}$ on the center of mass S depending on the lever arm l. (b),(c) Visualization of the experimental trajectory (for an illumination intensity of $I = 7.5~\mu W \mu m^{-2}$) that is used for the quantitative analysis of the fluctuation-averaged trajectory in (d). The dashed curve in (d) is the experimental one, and the solid curve shows the theoretical prediction with the starting point indicated by a red bullet. Inset: closeup of the framed area in the plot [190].

on the propulsion speed and, in particular, we find a linear increase of ω with v (Fig.7.3(a)). As a direct result of the linear relationship between ω and v, the radius $R = (\partial \omega / \partial v)^{-1}$ of the circular trajectories becomes independent of the propulsion speed, which is set by the illumination intensity (see Fig.7.3(b)).

7.2   Comparison with a theoretical description

For a theoretical description of the motion of asymmetric swimmers, we consider an effective propulsion force $\mathbf{F}$ [193], which is constant in a body-fixed coordinate system that rotates with the active particle. With the unit vectors $\hat{\mathbf{u}}_\perp = (-\sin\phi, \cos\phi)$ and $\hat{\mathbf{u}}_\parallel = (\cos\phi, \sin\phi)$ (see 7.4(a)), where, in case of L-shaped particles, ϕ is the angle between the short arm and the x axis, the propulsion force $\mathbf{F}$ is given by $\mathbf{F} = F\hat{\mathbf{u}}_{int}$ with $\hat{\mathbf{u}}_{int} = (c\hat{\mathbf{u}}_\parallel + \hat{\mathbf{u}}_\perp)/\sqrt{1+c^2}$ with the constant c depending on how the force is aligned relative to the particle shape. If the propulsion force is aligned along the long axis $\hat{\mathbf{u}}_\perp$, one obtains $c = 0$, i.e., $\hat{\mathbf{u}}_{int} = \hat{\mathbf{u}}_\perp$. In case of an asymmetric particle, the propulsion force leads also to a velocity-dependent torque relative to the particle's center-of-mass. For $c = 0$ this torque is given by $M = lF$ with l the effective lever arm (Fig.7.4(a)). Our theoretical model is valid for arbitrary particle shapes and values of c and l. However, for the sake of clarity, we set $c = 0$ as this applies for the L-shaped particles considered

106

here. Accordingly, we obtain the following coupled Langevin equations, which describe the motion of an asymmetric microswimmer.

$$\dot{\mathbf{r}} = \beta F\big(\mathrm{D_T}\hat{\mathbf{u}}_\perp + l\mathbf{D_C}\big) + \boldsymbol{\zeta_r} \,,$$
$$\dot{\phi} = \beta F\big(lD_\mathrm{R} + \mathbf{D_C}\!\cdot\!\hat{\mathbf{u}}_\perp\big) + \zeta_\phi \,.$$

(7.1)

Here, $\beta = 1/(k_B T)$ is the inverse effective thermal energy of the system. These Langevin equations contain the translational short-time diffusion tensor $\mathrm{D_T}(\phi) = D_\parallel \hat{\mathbf{u}}_\parallel \otimes \hat{\mathbf{u}}_\parallel + D_\parallel^\perp(\hat{\mathbf{u}}_\parallel \otimes \hat{\mathbf{u}}_\perp + \hat{\mathbf{u}}_\perp \otimes \hat{\mathbf{u}}_\parallel) + D_\perp \hat{\mathbf{u}}_\perp \otimes \hat{\mathbf{u}}_\perp$ with the dyadic product $\otimes$ and the translation-rotation coupling vector $\mathbf{D_C}(\phi) = D_\mathrm{C}^\parallel \hat{\mathbf{u}}_\parallel + D_\mathrm{C}^\perp \hat{\mathbf{u}}_\perp$. The translational diffusion coefficients $D_\parallel$, $D_\parallel^\perp$, and $D_\perp$, the coupling coefficients $D_\mathrm{C}^\parallel$ and $D_\mathrm{C}^\perp$, and the rotational diffusion constant D_R are determined by the specific shape of the particle. Finally, $\boldsymbol{\zeta_r}(t)$ and $\zeta_\phi(t)$ are Gaussian noise terms.

In case of vanishing noise, Eq. (7.1) immediately leads to a circular trajectory with a radius that, in agreement with the experimental observations (Fig.7.3(b)), does not depend on the particle velocity set by the propulsion force. Rather, the value of R is only determined by the particle's geometry, which defines its diffusion properties. Moreover, the translational and angular particle velocities are $v = \beta F\sqrt{(D_\parallel^\perp + lD_\mathrm{C}^\parallel)^2 + (D_\perp + lD_\mathrm{C}^\perp)^2}$ and $\omega = \beta F(D_\mathrm{C}^\perp + lD_\mathrm{R})$. Both quantities are proportional to the internal force F and ensure $R = v/|\omega|$ in perfect agreement with the experimental results shown in Fig.7.3(b).

For a quantitative comparison with the experimental data, most importantly, the diffusion and coupling coefficients for the particles under study have to be determined. They constitute the components of the generalized diffusion matrix and are, in principle, obtained from solving the Stokes equation that describes the low Reynolds number flow field around a particle close to the substrate [194]. This procedure can be approximated by using a bead model [195], where the L-shaped particle is assembled from a large number of rigidly connected small spheres. Exploiting the linearity of the Stokes equation, the hydrodynamic interactions between any pair of those beads can be superimposed to calculate the generalized mobility tensor of the L-shaped particle and from that its diffusion and coupling coefficients; details of the calculation are outlined in Ref. [195]. This method is well established for arbitrarily shaped particles in bulk solution [195, 196]. We take into account the presence of the substrate by using the Stokeslet close to a no-slip boundary [197] to model the hydrodynamic interactions between the component beads in the bead model. For the L-shaped particles considered here, we find the following approximated relation for the trajectory's radius R:

$$R = |D_\perp/(lD_\mathrm{R})|$$

(7.2)

and, correspondingly,

$$\omega = \beta D_{\mathrm{R}} l F \qquad (7.3)$$

for the angular velocity.

	experiment	theory
$D_{\perp}$ $[10^{-3}\mu m^2 s^{-1}]$	8.1 ± 0.6	8.3
$D_{\parallel}$ $[10^{-3}\mu m^2 s^{-1}]$	7.2 ± 0.4	7.5
D_{R} $[10^{-4} s^{-1}]$	6.2 ± 0.8	6.1

Table 7.1: Diffusion coefficients for the L-shaped particle in Fig.7.4(a) on a substrate: translational diffusion along the long ($D_{\perp}$) and the short ($D_{\parallel}$) axis of the L-shaped particle as well as rotational diffusion constant D_{R}.

We determined the diffusion coefficients $D_{\perp}$, $D_{\parallel}$, and D_{R} experimentally under equilibrium conditions ,i.e., in the absence of propulsion from the short-time correlations of the translational and orientational components of the particle's trajectories [198, 199] (see Tab. 7.1). The experimental values are in good agreement with the theoretical predictions.

Inserting the experimentally determined values for the diffusion coefficients and the mean trajectory radius $R = 7.91$ μm into Eq. (7.2), we obtain the effective lever arm $l = -1.65$ μm. This value is about a factor of two larger compared to an ideally shaped L-particle (see Fig.7.4(a)) with its propulsion force perfectly centered at the middle of the Au layer. This deviation suggests that the force is shifted by 0.94 μm in lateral direction, which is most likely caused by small inhomogeneities of the Au layer due to shadowing effects during the grazing incidence metal evaporation. Accordingly, from Eq. (7.3) we obtain the intensity-dependent propulsion force $F/I = 0.83 \times 10^{-13}$ $N\mu m^2 \mu W^{-1}$.

To compare the trajectories obtained from the Langevin equations (7.1) with experimental data, we divided the measured trajectories into smaller segments and superimposed them such that the initial slopes and positions of the segments overlap. After averaging the data we obtained the noise-averaged mean swimming path, which is predicted to be a logarithmic spiral (*spira mirabilis*) [200] that is given in polar coordinates by

$$r(\phi) = \beta F \sqrt{\frac{D_{\perp}^2}{D_{\mathrm{R}}^2 + \omega^2}} \exp\left(-\frac{D_{\mathrm{R}}}{\omega}(\phi - \phi_0)\right). \qquad (7.4)$$

Qualitatively, such spirals can be understood as follows: in the absence of thermal noise, the average swimming path corresponds to a circle with radius R given by Eq. (7.2). In the presence of thermal noise, however, single trajectory segments become increasingly different as time proceeds. This leads to decreasing distances d_i between adjacent turns of the mean
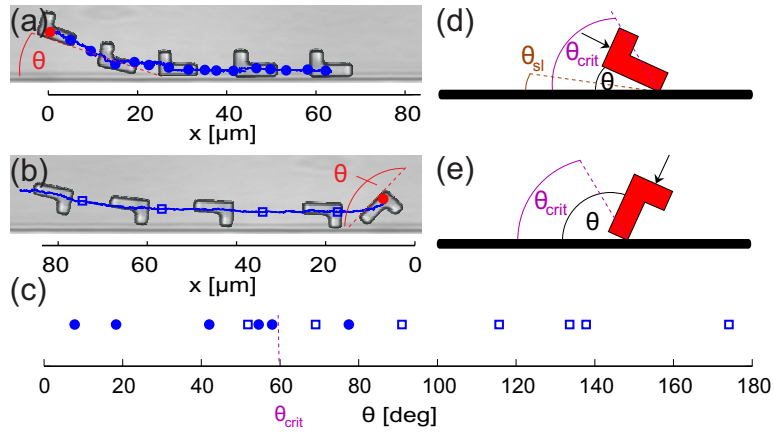
108

Figure 7.5: (a),(b) Trajectories of an L+ swimmer approaching a straight wall at different angles (symbols correspond to positions after 1 minute each). (c) Experimentally determined particle motion for different contact angles θ. Bullets and open squares correspond to particle sliding and reflection. (d),(e) Visualization of the predicted types of motion for an L+ swimmer with arrows indicating the direction of the propulsion force: (d) stable sliding and (e) reflection [190].

swimming path $(d_i/d_{i+1} = \exp(2\pi D_R/|\omega|)$, see Fig.7.4(d)) and, finally, to the convergence in a single point for $t \to \infty$. Due to the alignment of the initial slope, this point is shifted relative to the starting point depending on the alignment angle and the circulation direction of the particle.

The solid curve in Fig.7.4(d) is the theoretical prediction from Eq. (7.4) with the measured values of $D_\perp$, D_R, and ω. On the other hand, the dashed curve in Fig.7.4(d) visualizes the noise-averaged trajectory determined directly from the experimental data (Figs.7.4(b),(c)). The agreement of the two curves constitutes a direct verification of our theoretical model on a fundamental level.

7.3   Circular swimmers confined by a straight wall

We finally checked the behavior of L-shaped particles across a simple straight confinement, i.e., a wall. In §6.1.2 I have highlighted that the interaction of spherical (symmetric) swimmers with a wall do not any surprising behavior: the swimmers glides along the wall and gets reflected when its orientation points outwards. When the symmetry of the object is broken, the additional active torque widely enriches the behavior of the swimmers.

The interaction of an active L-particle with the wall is shown in Fig.7.5(a) exemplarily for an L+ swimmer which approaches the wall at an angle . Because of the internal torque associated with the active particle motion, it becomes stabilized at the wall and smoothly glides to the right along the

interface. In contrast, for a much larger initial contact angle the internal torque rotates the front part of the particle away from the obstacle, the motion is unstable, and the swimmer is reflected by the wall (see Fig.7.5(b)]. Fig.7.5(c) shows the observed dependence of the motional behavior on the approaching angle.

The experimental findings are in line with an instability analysis based on a torque balance condition of an L-shaped particle at wall contact as a function of its contact angle θ. For $\theta_{\mathrm{crit}} < \theta < \pi$ (see Figs.7.5(b),(e)) with a critical angle θ_{crit}, the particle is reflected, while for $0 < \theta < \theta_{\mathrm{crit}}$ (see Figs.7.5(a),(d)) stable sliding with an angle θ_{sl} occurs. Both, θ_{sl} and θ_{crit} are given as stable and unstable solutions, respectively, of the torque balance condition

$$|l| = [(a - y_{\mathrm{S}})\cos\theta - x_{\mathrm{S}}\sin\theta]\sin\theta . \qquad (7.5)$$

For $l = -0.71~\mu m$ corresponding to an ideal L-shaped particle with the propulsion force centered in the middle of the Au layer, we obtain $\theta_{\mathrm{sl}} = 8$ degrees and $\theta_{\mathrm{crit}} = 59.2$ degrees, which is in good agreement with the measured value of about $\theta_{\mathrm{crit}} = 60$ degrees (see Fig.7.5(c)). The observed scatter in the experimental data around the critical angle is due to thermal fluctuations that wash out the sharp transition between the sliding and the reflection regime.

7.4   Summary

We have demonstrated that, due to the viscous forces of the surrounding liquid, asymmetric microswimmers are subjected to a velocity-dependent torque. This leads to a circular motion, which is observed in experiments in agreement with a theoretical model based on two coupled Langevin equations. In a channel geometry, this torque leads either to a reflection or a stable sliding motion along the wall.

Our findings could be directly used to interpret the behavior of those biological swimmers whose shape cannot be approximated with a sphere.

Summary and outlook

In this thesis I have contextualized our experimental system in the broad field of active matter. This fascinating topic includes out-of-equilibrium phenomena where an object, either biological or artificial, takes up energy from the environment in order to perform a self-propelled directed motion.

At the micrometric scale, the propulsion in a viscous fluid becomes tricky because of the absence of inertial terms in the classical Navier-Stokes equation. In this case, a symmetry break is needed to achieve a directed motion without any additional external field. Chapter 1 focuses on this issue and on the tricks that biological microswimmers, such as bacteria, employ to navigate under low Reynold's number conditions.

During the past decades active matter at low Re also received a large interest among the physic and the nano-engineering communities. The opportunity of devising micron- and nano-sized motors, capable of powering their own motion inside, e.g., small capillaries, has been stimulating studies on a very fundamental level. Specifically, Chapter 2 addresses one class of autonomous propellers, based on self-generated phoretic forces. Such microswimmers break the symmetry of the medium creating a local gradient through which are then propelled due to phoretic forces.

A deep comparison with the classical Brownian motion of micrometric objects in a liquid unravels the novel properties of these tiny particles equipped with an internal driving. Chapter 3 highlights that the internal propulsion leads to a characteristic persistency given by the strength of the driving force. This persistency, combined with random features such as rotational diffusion, gives birth to novel bewitching paths usually grouped under the name of "active Brownian motion".

We have contributed to this field conceiving a novel 2D active system with half-coated colloids propelled by diffusiophoretic forces. The driving mechanism works when the solvent is a critical binary mixture and relies on the critical decomposition nearby the coated hemispheres of the particles. A laser light is used to heat selectively the coated side approaching thereby the critical temperature of the fluid. The activity, i.e., the strength of the propulsion, is controlled by the illumination power. Chapters 4 and 5 show the advantages of such propulsion mechanism and underline the tight

analogies with other active systems such as bacterial solution.

The active Brownian particles differ from their Brownian counterparts in many aspects due to the additional persistency (activity). We asked ourselves what are the implications of these differences when the swimmers are immersed in complex environments rather than in bulk solutions. This question is of extreme importance to acquire a better insight on the behavior of active organisms, like bacteria, in complex media (e.g., soils, blood vessels, dense solutions). Our self-propelled particles are the perfect tool to study these phenomena on the laboratory scale, providing thereby a direct observation of the samples. Chapter 6 describes two scenarios where the environment strongly deviates from the bulk. On one hand the presence of fixed obstacles leads to a preferential motion along open channels. On the other hand dense active suspension display a dynamical clustering induced by a reciprocal self-trapping. Under specific conditions of particles density and activity, this clustering can even develop into the phase separation of the sample.

Finally, the active motion of a particle changes radically when the driving force is not applied in the center-of-mass as it happens in many biological system where the weight is not homogenously distributed or where the body shows a geometrical asymmetry. The last Chapter investigates the behavior of asymmetric model L-shaped swimmers where, due to the geometrical configuration, an active torque is present along with the driving. The additional torque leads to a circular motion whose radius of curvature only depends on the geometry of the particles.

Of course the examples mentioned above and studied throughout this manuscript do not cover all the possible issues about this relatively new field, known as active matter. In the following I suggest few application of our experimental system aimed at modelling further realistic conditions.

Firstly, although we achieved a good control of the experimental system, a further investigation is certainly needed to understand the details of the propulsion mechanism. In Chapter 5 I have shown the profile of the demixing zone responsible for the directed motion. However, the full flow profile would definitely provide further insights on the propulsion. To grasp this information, neutral tracers particles, i.e., small colloids with no preference for either the lutidine or the water phase, would be needed to track the flow.

The ability of steering active objects only by tuning the light permits also to employ swimmers that act as shuttles in cargo delivery applications, e.g, drugs throughout human tissues. In the past decade several methods have been provided in order to collect and guide cargos: motor proteins, for instance, can be tether to their loads through a biotin-streptavidin bond [17]. Electrostatics [17] and magnetic links [18] have been also implemented onto catalytic motors. In this context, of course, both the cargo and the

shuttle have to be specifically functionalized to achieve the bond. The first step towards the realization of a suitable autonomous micro-shuttle consists in providing it with the ability of moving either backward or forward; the evaporation method described in Chapter 4 allows to coat opposite facets of the particle with two different materials absorbing light at different wavelengths. This way, according to the propulsion mechanism delineated in Chapter 5, the direction of the swimming speed would swap depending on which material is heated at the current wavelength. As a second step, a suitable shape of the swimmer has to be used in order to grab or dump the cargo. The fabrication of particles through soft-lithography, illustrated in Chapters 4 and 7 permits to create U-shaped swimmers able to collect the cargos in their "alcoves" and to release them when the motion is reversed.

Moreover, a study of the motion of self-propelled particles upon further complex environmental conditions would be for sure helpful to achieve a better understanding of some biological phenomena. The patterned structure and the clusters described in Chapter 6 resemble somehow the motion of bacteria in porous material and inside large colonies, respectively. However, chemotactic bacteria sometimes also move in swarms of passive (e.g., dead) organisms [201]. Such passive objects could be easily reproduced artificially using homogeneous, i.e., uncoated, Brownian colloids. Therefore, it would be definitely interesting to investigate experimentally the behavior of active particles in the presence of a medium made of mobile obstacles, as passive Brownian beads. An active particle, in order to carry on its active motion, has hereby to shove aside the surrounding Brownian colloids; therefore, while swimming, the active particle depletes "channels" which then remain open behind until the passive particles manage to diffuse back. Since crowded areas are tough for microswimmers to enter, microswimmers can help each other by undertaking the same paths. We expect that this behavior generates a so-called *adaptive landscape*, where swimmers indeed cooperate between each other.

Finally, an appealing outlook for the asymmetric swimmers described in Chapter 7 the motion of chiral swimmers in the presence of external fields such as gravity [202]. In the case of asymmetric particles, this leads to an orientational alignment during their sedimentation, which may result in a preferential motion relative to gravity similar to the gravitactic behavior of asymmetric cells as, e.g., *Chlamydomonas* [203, 204].

Thanks to..

There are several people I feel obliged to thank for their help and their support on different levels. You are/have been part of my life, You shared this experience with me although You might not have been physically here. You are a piece of my world and I feel lucky about that.

I hope nobody minds if I mention my family first and foremost. My mom Alda, my grandma Giuseppina, my aunts Loredana and Cecilia, my uncle Achille and my cousins Andrea and Alessandro. No other word is needed but a huge "thanks": you have been always on my side and I am sure you always will. Mom, we have been a small family: I think we turn out great though. My achievements have your fingerprint.

I would like thank all the people who guided me through science. Clemens Bechinger, for being more than just an advisor. You have been available every time I needed you, thank you. I hope I have been able to give you something back during these three years together at work. Giovanni Volpe and Felix Kümmel: I couldn't have wished for better colleagues. I truly enjoyed my time with you and I learned a lot from you. Roberto Piazza, together with Stefano Buzzaccaro and Daniele Vigolo: without you, I wouldn't be sitting here writing my thesis. I hope this gives you an idea of how important you have been. My science-mates at 2. Physikalisches Institut in Stuttgart and, in particular, Lamiss, Thomas, Maria, Olga, Ruben and Christoph with whom I had some cool times outside the institute too. Thomas Speck, for the worthwhile and profitable collaboration. Finally, all the Comploids fellows: I had so much fun with you guys.

Last but not least, thanks to my friends in Italy and to those scattered around the world. In particular, my flatmate Satoshi: good luck for your new life in Japan. Fabio, Paolo, Paola and Fabio for the wonderful times together and the blast we had each year at the Volksfest. Anna: I wish we had shared more experiences and, anyways, I am going to miss you wherever you will end up. The London-pals Luigi and Stefano: I look forward to visiting you again and to seeing you in Zürich soon.

Bibliography

[1] E. M. Purcell. "Life at low Reynolds number." *Am. J. Phys*, **45**, 1, (1977), 3–11.

[2] L. T. Haimo and J. L. Rosenbaum. "Cilia, flagella, and microtubules." *The journal of cell biology*, **91**, 3, (1981), 125s–130s.

[3] E. Lauga and T. R. Powers. "The hydrodynamics of swimming microorganisms." *Reports on Progress in Physics*, **72**, 9, (2009), 096601.

[4] D. Bray. *Cell movements: from molecules to motility* (Routledge) (2000).

[5] S. Koyasu and Y. Shirakihara. "Caulobacter crescentus flagellar filament has a right-handed helical form." *Journal of molecular biology*, **173**, 1, (1984), 125–130.

[6] N. Shao, C. F. Beck, S. D. Lemaire and A. Krieger-Liszkay. "Photosynthetic electron flow affects H2O2 signaling by inactivation of catalase in Chlamydomonas reinhardtii." *Planta*, **228**, 6, (2008), 1055–1066.

[7] H. C. Berg. *E. coli in Motion* (Springer) (2003).

[8] H. C. Berg, D. A. Brown et al. "Chemotaxis in Escherichia coli analysed by three-dimensional tracking." *Nature*, **239**, 5374, (1972), 500–504.

[9] A. Najafi and R. Golestanian. "Propulsion at low Reynolds number." *Journal of Physics: Condensed Matter*, **17**, 14, (2005), S1203.

[10] R. Dreyfus, J. Baudry, M. L. Roper, M. Fermigier, H. A. Stone and J. Bibette. "Microscopic artificial swimmers." *Nature*, **437**, 7060, (2005), 862–865.

[11] L. Zhang, J. J. Abbott, L. Dong, K. E. Peyer, B. E. Kratochvil, H. Zhang, C. Bergeles and B. J. Nelson. "Characterizing the swimming properties of artificial bacterial flagella." *Nano letters*, **9**, 10, (2009), 3663–3667.

[12] P. Tierno, R. Golestanian, I. Pagonabarraga and F. Sague?s. "Magnetically actuated colloidal microswimmers." *The Journal of Physical Chemistry B*, **112**, 51, (2008), 16525–16528.

[13] A. Ghosh and P. Fischer. "Controlled propulsion of artificial magnetic nanostructured propellers." *Nano letters*, **9**, 6, (2009), 2243–2245.

[14] T. Mirkovic, N. S. Zacharia, G. D. Scholes and G. A. Ozin. "Fuel for thought: chemically powered nanomotors out-swim nature flagellated bacteria." *ACS nano*, **4**, 4, (2010), 1782–1789.

[15] S. J. Ebbens and J. R. Howse. "In pursuit of propulsion at the nanoscale." *Soft Matter*, **6**, 4, (2010), 726–738.

[16] Z. Ghalanbor, S.-A. Marashi and B. Ranjbar. "Nanotechnology helps medicine: nanoscale swimmers and their future applications." *Medical hypotheses*, **65**, 1, (2005), 198–199.

[17] S. Sundararajan, P. E. Lammert, A. W. Zudans, V. H. Crespi and A. Sen. "Catalytic motors for transport of colloidal cargo." *Nano letters*, **8**, 5, (2008), 1271–1276.

[18] J. Burdick, R. Laocharoensuk, P. M. Wheat, J. D. Posner and J. Wang. "Synthetic nanomotors in microchannel networks: Directional microchip motion and controlled manipulation of cargo." *Journal of the American Chemical Society*, **130**, 26, (2008), 8164–8165.

[19] M. O. I. Prirody. *Nouveaux mémoires de la Société Impériale des Naturalistes de Moscou*, vol. 10 (1855).

[20] A. Tiselius. "A new apparatus for electrophoretic analysis of colloidal mixtures." *Transactions of the Faraday Society*, **33**, (1937), 524–531.

[21] J. F. Robyt and B. J. White. *Biochemical techniques: theory and practice* (Waveland Press Illinois, IL) (1990).

[22] P. H. Prausnitz and J. Reitstötter. *Elektrophorese, elektroosmose, elektrodialyse in flüssigkeiten*, vol. 24 (T. Steinkopff) (1931).

[23] S. Dukhin, B. Derjaguin and E. Matijevic. "Surface and colloid science." *Vol. 7Wiley, New York*, pages 143–145.

[24] B. Derjaguin. *Some results from 50 years' research on surface forces* (Springer) (1987).

[25] Y. K. Wei and H. J. Keh. "Diffusiophoresis and electrophoresis in concentrated suspensions of charged colloidal spheres." *Langmuir*, **17**, 5, (2001), 1437–1447.

116

[26] J. Ebel, J. L. Anderson and D. Prieve. "Diffusiophoresis of latex particles in electrolyte gradients." *Langmuir*, **4**, 2, (1988), 396–406.

[27] J. L. Anderson and D. C. Prieve. "Diffusiophoresis: migration of colloidal particles in gradients of solute concentration." *Separation And Purification Methods*, **13**, 1, (1984), 67–103.

[28] H. J. Keh and J. S. Jan. "Boundary effects on diffusiophoresis and electrophoresis: motion of a colloidal sphere normal to a plane wall." *Journal of colloid and interface science*, **183**, 2, (1996), 458–475.

[29] C. Ludwig, K. H.-u. Staatsdruckerei and W. Braumüller. *Diffusion zwischen ungleich erwärmten Orten gleich zusammengesetzter Lösung* (Aus der KK Hof-und Staatsdruckerei, in Commission bei W. Braumüller, Buchhändler des KK Hofes und der K. Akademie der Wissenschaften) (1856).

[30] J. Platten and P. Costesèque. "Charles Soret. A short biographya." *The European Physical Journal E*, **15**, 3, (2004), 235–239.

[31] J. L. Anderson. "Colloid transport by interfacial forces." *Annual Review of Fluid Mechanics*, **21**, 1, (1989), 61–99.

[32] N. Young, J. S. Goldstein and M. Block. "The motion of bubbles in a vertical temperature gradient." *Journal of Fluid Mechanics*, **6**, 03, (1959), 350–356.

[33] E. Ruckenstein. "Can phoretic motions be treated as interfacial tension gradient driven phenomena?" *Journal of Colloid and Interface Science*, **83**, 1, (1981), 77–81.

[34] P. K. Dasgupta and S. Liu. "Electroosmosis: a reliable fluid propulsion system for flow injection analysis." *Analytical Chemistry*, **66**, 11, (1994), 1792–1798.

[35] T. M. Squires and M. Z. Bazant. "Induced-charge electro-osmosis." *Journal of Fluid Mechanics*, **509**, 217-252, (2004), 72–80.

[36] A. Ajdari and L. Bocquet. "Giant amplification of interfacially driven transport by hydrodynamic slip: Diffusio-osmosis and beyond." *Physical review letters*, **96**, 18, (2006), 186102.

[37] H. J. Keh and H. C. Ma. "Diffusioosmosis of electrolyte solutions in fine capillaries." *Colloids and Surfaces A: Physicochemical and Engineering Aspects*, **233**, 1, (2004), 87–95.

[38] I. W. Hamley. *Introduction to soft matter: synthetic and biological self-assembling materials* (Wiley) (2008).

[39] M. Smoluchowski. "Contribution to the theory of electro-osmosis and related phenomena." *Bull Int Acad Sci Cracovie*, **3**, (1903), 184–199.

[40] P. C. Hiemenz and R. Rajagopalan. *Principles of Colloid and Surface Chemistry, revised and expanded*, vol. 14 (CRC Press) (1997).

[41] A. S. Khair and T. M. Squires. "Ion steric effects on electrophoresis of a colloidal particle." *Journal of Fluid Mechanics*, **640**, (2009), 343.

[42] R. W. O'Brien and L. R. White. "Electrophoretic mobility of a spherical colloidal particle." *J. Chem. Soc., Faraday Trans. 2*, **74**, (1978), 1607–1626.

[43] H. Lüth. *Surfaces and interfaces of solid materials* (Springer Berlin, Heidelberg, New York) (1997).

[44] D. Vigolo. *Thermophoresis in Complex Fluids* (PhD Thesis, Politecnico di Milano, Facoltà di Ingegneria) (AA 2007-2010).

[45] R. Piazza and A. Parola. "Thermophoresis in colloidal suspensions." *Journal of Physics: Condensed Matter*, **20**, 15, (2008), 153102.

[46] M. Braibanti, D. Vigolo and R. Piazza. "Does thermophoretic mobility depend on particle size?" *Physical review letters*, **100**, 10, (2008), 108303.

[47] R. Piazza and A. Guarino. "Soret effect in interacting micellar solutions." *Physical review letters*, **88**, 20, (2002), 208302.

[48] J. Rauch and W. Köhler. "Collective and thermal diffusion in dilute, semidilute, and concentrated solutions of polystyrene in toluene." *The Journal of chemical physics*, **119**, (2003), 11977.

[49] H. Ning, J. K. Dhont and S. Wiegand. "Thermal-diffusive behavior of a dilute solution of charged colloids." *Langmuir*, **24**, 6, (2008), 2426–2432.

[50] S. Iacopini, R. Rusconi and R. Piazza. "The macromolecular tourist: Universal temperature dependence of thermal diffusion in aqueous colloidal suspensions." *The European Physical Journal E*, **19**, 1, (2006), 59–67.

[51] R. Golestanian, T. B. Liverpool and A. Ajdari. "Propulsion of a molecular machine by asymmetric distribution of reaction products." *Physical review letters*, **94**, 22, (2005), 220801.

[52] S. Jiang, Q. Chen, M. Tripathy, E. Luijten, K. S. Schweizer and S. Granick. "Janus particle synthesis and assembly." *Advanced Materials*, **22**, 10, (2010), 1060–1071.

[53] Q. Chen, S. C. Bae and S. Granick. "Directed self-assembly of a colloidal kagome lattice." *Nature*, **469**, 7330, (2011), 381–384.

[54] Q. Chen, J. K. Whitmer, S. Jiang, S. C. Bae, E. Luijten and S. Granick. "Supracolloidal reaction kinetics of Janus spheres." *Science*, **331**, 6014, (2011), 199–202.

[55] Z. Zhang and S. C. Glotzer. "Self-assembly of patchy particles." *Nano Letters*, **4**, 8, (2004), 1407–1413.

[56] Z. Zhang, A. S. Keys, T. Chen and S. C. Glotzer. "Self-assembly of patchy particles into diamond structures through molecular mimicry." *Langmuir*, **21**, 25, (2005), 11547–11551.

[57] S. C. Glotzer and M. J. Solomon. "Anisotropy of building blocks and their assembly into complex structures." *Nature materials*, **6**, 8, (2007), 557–562.

[58] M. G. Noro and D. Frenkel. "Extended corresponding-states behavior for particles with variable range attractions." *The Journal of Chemical Physics*, **113**, 8, (2000), 2941.

[59] E. Bianchi, R. Blaak and C. N. Likos. "Patchy colloids: state of the art and perspectives." *Physical Chemistry Chemical Physics*, **13**, 14, (2011), 6397–6410.

[60] F. Sciortino, A. Giacometti and G. Pastore. "Phase diagram of janus particles." *Physical review letters*, **103**, 23, (2009), 237801.

[61] F. Sciortino, A. Giacometti and G. Pastore. "A numerical study of one-patch colloidal particles: from square-well to Janus." *Physical Chemistry Chemical Physics*, **12**, 38, (2010), 11869–11877.

[62] R. Fantoni, A. Giacometti, F. Sciortino and G. Pastore. "Cluster theory of Janus particles." *Soft Matter*, **7**, 6, (2011), 2419–2427.

[63] M. Lattuada and T. A. Hatton. "Synthesis, properties and applications of Janus nanoparticles." *Nano Today*, **6**, 3, (2011), 286–308.

[64] Y. Yin, S. Zhou, B. You and L. Wu. "Facile fabrication and self-assembly of polystyrene silica asymmetric colloid spheres." *Journal of Polymer Science Part A: Polymer Chemistry*, **49**, 15, (2011), 3272–3279.

[65] J. Hu, S. Zhou, Y. Sun, X. Fang and L. Wu. "Fabrication, properties and applications of Janus particles." *Chemical Society Reviews*, **41**, 11, (2012), 4356–4378.

[66] M. D. McConnell, M. J. Kraeutler, S. Yang and R. J. Composto. "Patchy and multiregion janus particles with tunable optical properties." *Nano letters*, **10**, 2, (2010), 603–609.

[67] A. Perro, F. Meunier, V. Schmitt and S. Ravaine. "Production of large quantities of Janus nanoparticles using wax-in-water emulsions." *Colloids and Surfaces A: Physicochemical and Engineering Aspects*, **332**, 1, (2009), 57–62.

[68] K.-H. Roh, D. C. Martin and J. Lahann. "Biphasic Janus particles with nanoscale anisotropy." *Nature Materials*, **4**, 10, (2005), 759–763.

[69] L. Hong, S. Jiang and S. Granick. "Simple method to produce Janus colloidal particles in large quantity." *Langmuir*, **22**, 23, (2006), 9495–9499.

[70] S. U. Pickering. "Emulsions." *Journal of the Chemical Society, Transactions*, **91**, (1907), 2001–2021.

[71] W. Poon. "From Clarkia to Escherichia and Janus: the physics of natural and synthetic active colloids." *arXiv preprint arXiv:1306.4799*.

[72] J. Palacci, C. Cottin-Bizonne, C. Ybert and L. Bocquet. "Sedimentation and effective temperature of active colloidal suspensions." *Physical review letters*, **105**, 8, (2010), 088304.

[73] I. Theurkauff, C. Cottin-Bizonne, J. Palacci, C. Ybert and L. Bocquet. "Dynamic clustering in active colloidal suspensions with chemical signaling." *Physical Review Letters*, **108**, 26, (2012), 268303.

[74] J. R. Howse, R. A. Jones, A. J. Ryan, T. Gough, R. Vafabakhsh and R. Golestanian. "Self-motile colloidal particles: from directed propulsion to random walk." *Physical review letters*, **99**, 4, (2007), 048102.

[75] S. Ebbens, M.-H. Tu, J. R. Howse and R. Golestanian. "Size dependence of the propulsion velocity for catalytic Janus-sphere swimmers." *Physical Review E*, **85**, 2, (2012), 020401.

[76] W. F. Paxton, K. C. Kistler, C. C. Olmeda, A. Sen, S. K. St. Angelo, Y. Cao, T. E. Mallouk, P. E. Lammert and V. H. Crespi. "Catalytic nanomotors: Autonomous movement of striped nanorods." *Journal of the American Chemical Society*, **126**, 41, (2004), 13424–13431.

[77] Y. Wang, R. M. Hernandez, D. J. Bartlett, J. M. Bingham, T. R. Kline, A. Sen and T. E. Mallouk. "Bipolar electrochemical mechanism for the propulsion of catalytic nanomotors in hydrogen peroxide solutions." *Langmuir*, **22**, 25, (2006), 10451–10456.

[78] W. F. Paxton, A. Sen and T. E. Mallouk. "Motility of catalytic nanoparticles through self-generated forces." *Chemistry-A European Journal*, **11**, 22, (2005), 6462–6470.

[79] S. Fournier-Bidoz, A. C. Arsenault, I. Manners and G. A. Ozin. "Synthetic self-propelled nanorotors." *Chemical Communications*, , 4, (2005), 441–443.

[80] N. Mano and A. Heller. "Bioelectrochemical propulsion." *Journal of the American Chemical Society*, **127**, 33, (2005), 11574–11575.

[81] D. Pantarotto, W. R. Browne and B. L. Feringa. "Autonomous propulsion of carbon nanotubes powered by a multienzyme ensemble." *Chemical Communications*, , 13, (2008), 1533–1535.

[82] J. Palacci, S. Sacanna, A. P. Steinberg, D. J. Pine and P. M. Chaikin. "Living Crystals of Light-Activated Colloidal Surfers." *Science*, **339**, 6122, (2013), 936–940.

[83] H.-R. Jiang, N. Yoshinaga and M. Sano. "Active motion of a Janus particle by self-thermophoresis in a defocused laser beam." *Physical review letters*, **105**, 26, (2010), 268302.

[84] R. Golestanian. "Debut of a hot fantastic voyager." *Physcs Online Journal*, **3**, (2010), 108.

[85] R. M. Mazo. *Brownian motion: fluctuations, dynamics, and applications*, vol. 112 (OUP Oxford) (2008).

[86] F. Schweitzer. *Brownian agents and active particles: collective dynamics in the natural and social sciences* (Springer) (2007).

[87] R. Brown. "XXVII. A brief account of microscopical observations made in the months of June, July and August 1827, on the particles contained in the pollen of plants; and on the general existence of active molecules in organic and inorganic bodies." *The Philosophical Magazine, or Annals of Chemistry, Mathematics, Astronomy, Natural History and General Science*, **4**, 21, (1828), 161–173.

[88] A. Einstein. "On the movement of small particles suspended in stationary liquids required by the molecular-kinetic theory of heat." *Annalen der Physik*, **17**, 549-560, (1905), 16.

[89] E. Nelson. *Dynamical theories of Brownian motion*, vol. 17 (Princeton university press Princeton) (1967).

[90] M. Von Smoluchowski. "Zur kinetischen theorie der brownschen molekularbewegung und der suspensionen." *Annalen der physik*, **326**, 14, (1906), 756–780.

[91] P. Langevin. "Sur la theorie du mouvement brownien." *CR Acad. Sci. Paris*, **146**, 530-533.

[92] K. Pearson. "The problem of the random walk." *Nature*, **72**, 1865, (1905), 294.

[93] V. Tejedor, R. Voituriez and O. Bénichou. "Optimizing persistent random searches." *Physical Review Letters*, **108**, 8, (2012), 088103.

[94] G. Viswanathan, S. V. Buldyrev, S. Havlin, M. Da Luz, E. Raposo and H. E. Stanley. "Optimizing the success of random searches." *Nature*, **401**, 6756, (1999), 911–914.

[95] A. Reynolds and C. Rhodes. "The Levy flight paradigm: random search patterns and mechanisms." *Ecology*, **90**, 4, (2009), 877–887.

[96] G. Viswanathan, E. Raposo and M. Da Luz. "Levy flights and superdiffusion in the context of biological encounters and random searches." *Physics of Life Reviews*, **5**, 3, (2008), 133–150.

[97] F. Bartumeus i Ferré et al. "Levy Processes in Animal Movement and Dispersal."

[98] U. Erdmann, W. Ebeling, L. Schimansky-Geier and F. Schweitzer. "Brownian particles far from equilibrium." *The European Physical Journal B-Condensed Matter and Complex Systems*, **15**, 1, (2000), 105–113.

[99] W. Ebeling and F. Schweitzer. "Self-organization, active brownian dynamics, and biological applications." *arXiv preprint cond-mat/0211606*.

[100] A. Mikhailov and D. Meinköhn. "Self-motion in physico-chemical systems far from thermal equilibrium." In "Stochastic Dynamics," pages 334–345 (Springer) (1997).

[101] E. A. Codling, M. J. Plank and S. Benhamou. "Random walk models in biology." *Journal of the Royal Society Interface*, **5**, 25, (2008), 813–834.

[102] W. Thomson. "On the theory of the electric telegraph." *Proceedings of the Royal Society of London*, **7**, (1854), 382–399.

[103] J. P. Hernandez-Ortiz, C. G. Stoltz and M. D. Graham. "Transport and collective dynamics in suspensions of confined swimming particles." *Physical review letters*, **95**, 20, (2005), 204501.

[104] I. O. Götze and G. Gompper. "Flow generation by rotating colloids in planar microchannels." *EPL (Europhysics Letters)*, **92**, 6, (2010), 64003.

[105] V. B. Putz and J. M. Yeomans. "Hydrodynamic synchronisation of model microswimmers." *Journal of Statistical Physics*, **137**, 5-6, (2009), 1001–1013.

[106] D. Saintillan and M. J. Shelley. "Instabilities, pattern formation, and mixing in active suspensions." *Physics of Fluids*, **20**, (2008), 123304.

[107] C. Pooley, G. Alexander and J. Yeomans. "Hydrodynamic interaction between two swimmers at low Reynolds number." *Physical review letters*, **99**, 22, (2007), 228103.

[108] P. D. Frymier, R. M. Ford, H. C. Berg and P. T. Cummings. "Three-dimensional tracking of motile bacteria near a solid planar surface." *Proceedings of the National Academy of Sciences*, **92**, 13, (1995), 6195–6199.

[109] S. Ramaswamy and M. Rao. "Active-filament hydrodynamics: instabilities, boundary conditions and rheology." *New Journal of Physics*, **9**, 11, (2007), 423.

[110] M. Cates. "Diffusive transport without detailed balance in motile bacteria: does microbiology need statistical physics?" *Reports on Progress in Physics*, **75**, 4, (2012), 042601.

[111] M. T. Downton and H. Stark. "Simulation of a model microswimmer." *Journal of Physics: Condensed Matter*, **21**, 20, (2009), 204101.

[112] H. Takei and N. Shimizu. "Gradient sensitive microscopic probes prepared by gold evaporation and chemisorption on latex spheres." *Langmuir*, **13**, 7, (1997), 1865–1868.

[113] O. Cayre, V. N. Paunov and O. D. Velev. "Fabrication of asymmetrically coated colloid particles by microcontact printing techniques." *Journal of Materials Chemistry*, **13**, 10, (2003), 2445–2450.

[114] Y. Lu, H. Xiong, X. Jiang, Y. Xia, M. Prentiss and G. M. Whitesides. "Asymmetric dimers can be formed by dewetting half-shells of gold deposited on the surfaces of spherical oxide colloids." *Journal of the American Chemical Society*, **125**, 42, (2003), 12724–12725.

[115] G. Volpe, I. Buttinoni, D. Vogt, H.-J. Kümmerer and C. Bechinger. "Microswimmers in patterned environments." *Soft Matter*, **7**, 19, (2011), 8810–8815.

[116] F. Sciortino, S. Mossa, E. Zaccarelli and P. Tartaglia. "Equilibrium cluster phases and low-density arrested disordered states: the role of short-range attraction and long-range repulsion." *Physical review letters*, **93**, 5, (2004), 055701.

[117] P. J. Lu and D. A. Weitz. "Colloidal Particles: Crystals, Glasses, and Gels." *Annu. Rev. Condens. Matter Phys.*, **4**, 1, (2013), 217–233.

[118] W. Poon, P. Pusey and H. Lekkerkerker. "Colloids in suspense." *Physics World*, **9**, 4, (1996), 27–34.

[119] A. Yethiraj and A. van Blaaderen. "A colloidal model system with an interaction tunable from hard sphere to soft and dipolar." *Nature*, **421**, 6922, (2003), 513–517.

[120] V. J. Anderson and H. N. Lekkerkerker. "Insights into phase transition kinetics from colloid science." *Nature*, **416**, 6883, (2002), 811–815.

[121] P. J. Lu, J. C. Conrad, H. M. Wyss, A. B. Schofield and D. A. Weitz. "Fluids of clusters in attractive colloids." *Physical review letters*, **96**, 2, (2006), 028306.

[122] P. J. Lu, E. Zaccarelli, F. Ciulla, A. B. Schofield, F. Sciortino and D. A. Weitz. "Gelation of particles with short-range attraction." *Nature*, **453**, 7194, (2008), 499–503.

[123] F. Sciortino. "Disordered materials: One liquid, two glasses." *Nature materials*, **1**, 3, (2002), 145–146.

[124] J. N. Israelachvili and H. Wennerstroem. "Entropic forces between amphiphilic surfaces in liquids." *The Journal of Physical Chemistry*, **96**, 2, (1992), 520–531.

[125] I. Buttinoni, J. Bialké, F. Kümmel, H. Löwen, C. Bechinger and T. Speck. "Dynamical clustering and phase separation in suspensions of self-propelled colloidal particles." *Physical Review Letters*, **110**, 23, (2013), 238301.

[126] Y. Xia and G. M. Whitesides. "Soft lithography." *Annual review of materials science*, **28**, 1, (1998), 153–184.

[127] I. Buttinoni, G. Volpe, F. Kümmel, G. Volpe and C. Bechinger. "Active Brownian motion tunable by light." *Journal of Physics: Condensed Matter*, **24**, 28, (2012), 284129.

[128] P. M. Chaikin and T. C. Lubensky. *Principles of condensed matter physics*, vol. 1 (Cambridge Univ Press) (2000).

[129] J. W. Cahn. "Phase separation by spinodal decomposition in isotropic systems." *The Journal of Chemical Physics*, **42**, (1965), 93.

[130] E. Herzig, K. White, A. Schofield, W. Poon and P. Clegg. "Bicontinuous emulsions stabilized solely by colloidal particles." *Nature materials*, **6**, 12, (2007), 966–971.

[131] M. E. Cates and P. S. Clegg. "Bijels: A new class of soft materials." *Soft Matter*, **4**, 11, (2008), 2132–2138.

[132] C. A. Grattoni, R. A. Dawe, C. Y. Seah and J. D. Gray. "Lower critical solution coexistence curve and physical properties (density, viscosity, surface tension, and interfacial tension) of 2, 6-lutidine+ water." *Journal of Chemical and Engineering Data*, **38**, 4, (1993), 516–519.

[133] Q. Zhan. "Trapping metallic Rayleigh particles with radial polarization." *Optics express*, **12**, 15, (2004), 3377–3382.

[134] E. Palik. "Handbook of Optical Constants of Solids (Orlando, FL: Academic)."

[135] G. Baffou, R. Quidant and C. Girard. "Heat generation in plasmonic nanostructures: Influence of morphology." *Applied Physics Letters*, **94**, 15, (2009), 153109–153109.

[136] O. J. Martin, C. Girard and A. Dereux. "Generalized field propagator for electromagnetic scattering and light confinement." *Physical review letters*, **74**, 4, (1995), 526.

[137] J. G. Mitchell and K. Kogure. "Bacterial motility: links to the environment and a driving force for microbial physics." *FEMS microbiology ecology*, **55**, 1, (2006), 3–16.

[138] W.-W. Tso and J. Adler. "Negative chemotaxis in Escherichia coli." *Journal of bacteriology*, **118**, 2, (1974), 560–576.

[139] J. Adler. "A method for measuring chemotaxis and use of the method to determine optimum conditions for chemotaxis by Escherichia coli." *Journal of General Microbiology*, **74**, 1, (1973), 77–91.

[140] F. Matthaus, M. Jagodic and J. Dobnikar. "E. coli. Superdiffusion and Chemotaxis Search Strategy, Precision, and Motility." *Biophysical journal*, **97**, 4, (2009), 946–957.

[141] J. Männik, R. Driessen, P. Galajda, J. E. Keymer and C. Dekker. "Bacterial growth and motility in sub-micron constrictions." *Proceedings of the National Academy of Sciences*, **106**, 35, (2009), 14861–14866.

[142] L. Hall-Stoodley, J. W. Costerton and P. Stoodley. "Bacterial biofilms: from the natural environment to infectious diseases." *Nature Reviews Microbiology*, **2**, 2, (2004), 95–108.

[143] K. H. Baker, D. S. Herson et al. *Bioremediation*. (McGraw-Hill, Inc.) (1994).

[144] H. Moon, R. Isaacson and J. Pohlenz. "Mechanisms of association of enteropathogenic Escherichia coli with intestinal epithelium." *The American journal of clinical nutrition*, **32**, 1, (1979), 119–127.

[145] R. M. Ford and R. W. Harvey. "Role of chemotaxis in the transport of bacteria through saturated porous media." *Advances in water resources*, **30**, 6, (2007), 1608–1617.

[146] M. Binz, A. P. Lee, C. Edwards and D. V. Nicolau. "Motility of bacteria in microfluidic structures." *Microelectronic Engineering*, **87**, 5, (2010), 810–813.

[147] R. Di Leonardo, L. Angelani, D. Dell'Arciprete, G. Ruocco, V. Iebba, S. Schippa, M. Conte, F. Mecarini, F. De Angelis and E. Di Fabrizio. "Bacterial ratchet motors." *Proceedings of the National Academy of Sciences*, **107**, 21, (2010), 9541–9545.

[148] F. J. Valdes-Parada, M. L. Porter, K. Narayanaswamy, R. M. Ford and B. D. Wood. "Upscaling microbial chemotaxis in porous media." *Advances in Water Resources*, **32**, 9, (2009), 1413–1428.

[149] R. Huang, I. Chavez, K. M. Taute, B. Lukiic, S. Jeney, M. G. Raizen and E.-L. Florin. "Direct observation of the full transition from ballistic to diffusive Brownian motion in a liquid." *Nature Physics*, **7**, 7, (2011), 576–580.

[150] D. L. Englert, M. D. Manson and A. Jayaraman. "Investigation of bacterial chemotaxis in flow-based microfluidic devices." *Nature protocols*, **5**, 5, (2010), 864–872.

[151] H. Mao, P. S. Cremer and M. D. Manson. "A sensitive, versatile microfluidic assay for bacterial chemotaxis." *Proceedings of the National Academy of Sciences*, **100**, 9, (2003), 5449–5454.

[152] D. L. Englert, M. D. Manson and A. Jayaraman. "Flow-based microfluidic device for quantifying bacterial chemotaxis in stable, competing gradients." *Applied and environmental microbiology*, **75**, 13, (2009), 4557–4564.

[153] D. L. Englert, A. Jayaraman and M. D. Manson. "Microfluidic techniques for the analysis of bacterial chemotaxis." In "Chemotaxis," pages 1–23 (Springer) (2009).

[154] A. Czirók, E. Ben-Jacob, I. Cohen and T. Vicsek. "Formation of complex bacterial colonies via self-generated vortices." *Physical Review E*, **54**, 2, (1996), 1791.

[155] A. Cavagna, A. Cimarelli, I. Giardina, G. Parisi, R. Santagati, F. Stefanini and M. Viale. "Scale-free correlations in starling flocks." *Proceedings of the National Academy of Sciences*, **107**, 26, (2010), 11865–11870.

[156] K. Drescher, K. C. Leptos, I. Tuval, T. Ishikawa, T. J. Pedley and R. E. Goldstein. "Dancing Volvox: Hydrodynamic bound states of swimming algae." *Physical review letters*, **102**, 16, (2009), 168101.

[157] F. Peruani, J. Starruß, V. Jakovljevic, L. Søgaard-Andersen, A. Deutsch and M. Bär. "Collective motion and nonequilibrium cluster formation in colonies of gliding bacteria." *Physical Review Letters*, **108**, 9, (2012), 098102.

[158] K. Drescher, J. Dunkel, L. H. Cisneros, S. Ganguly and R. E. Goldstein. "Fluid dynamics and noise in bacterial cell–cell and cell–surface scattering." *Proceedings of the National Academy of Sciences*, **108**, 27, (2011), 10940–10945.

[159] A. Sokolov and I. S. Aranson. "Physical properties of collective motion in suspensions of bacteria." *Physical review letters*, **109**, 24, (2012), 248109.

[160] A. Sokolov, I. S. Aranson, J. O. Kessler and R. E. Goldstein. "Concentration dependence of the collective dynamics of swimming bacteria." *Physical review letters*, **98**, 15, (2007), 158102.

[161] G. O'Toole, H. B. Kaplan and R. Kolter. "Biofilm formation as microbial development." *Annual Reviews in Microbiology*, **54**, 1, (2000), 49–79.

[162] T. Vicsek, A. Czirók, E. Ben-Jacob, I. Cohen and O. Shochet. "Novel type of phase transition in a system of self-driven particles." *Physical Review Letters*, **75**, 6, (1995), 1226.

[163] H. H. Wensink, J. Dunkel, S. Heidenreich, K. Drescher, R. E. Goldstein, H. Löwen and J. M. Yeomans. "Meso-scale turbulence in living fluids." *Proceedings of the National Academy of Sciences*, **109**, 36, (2012), 14308–14313.

[164] D. Chandler. "Introduction to modern statistical mechanics." *Introduction to Modern Statistical Mechanics, by David Chandler, pp. 288. Foreword by David Chandler. Oxford University Press, Sep 1987. ISBN-10: 0195042778. ISBN-13: 9780195042771*, **1**.

[165] C. Van den Broeck, J. Parrondo and R. Toral. "Noise-induced nonequilibrium phase transition." *Physical review letters*, **73**, 25, (1994), 3395.

[166] F. Sagués, J. M. Sancho and J. García-Ojalvo. "Spatiotemporal order out of noise." *Reviews of Modern Physics*, **79**, 3, (2007), 829.

[167] D. Helbing, I. J. Farkas and T. Vicsek. "Freezing by heating in a driven mesoscopic system." *Physical review letters*, **84**, 6, (2000), 1240.

[168] A. Czirók and T. Vicsek. "Collective behavior of interacting self-propelled particles." *Physica A: Statistical Mechanics and its Applications*, **281**, 1, (2000), 17–29.

[169] G. S. Redner, M. F. Hagan and A. Baskaran. "Structure and Dynamics of a Phase-Separating Active Colloidal Fluid." *Physical review letters*, **110**, 5, (2013), 055701.

[170] A. Deutsch, G. Theraulaz and T. Vicsek. "Collective motion in biological systems." *Interface Focus*, **2**, 6, (2012), 689–692.

[171] V. Narayan, S. Ramaswamy and N. Menon. "Long-lived giant number fluctuations in a swarming granular nematic." *Science*, **317**, 5834, (2007), 105–108.

[172] J. Deseigne, O. Dauchot and H. Chaté. "Collective motion of vibrated polar disks." *Physical review letters*, **105**, 9, (2010), 098001.

[173] J. Bialké, T. Speck and H. Löwen. "Crystallization in a dense suspension of self-propelled particles." *Physical Review Letters*, **108**, 16, (2012), 168301.

[174] Y. Fily and M. C. Marchetti. "Athermal Phase Separation of Self-Propelled Particles with No Alignment." *Physical Review Letters*, **108**, 23, (2012), 235702.

[175] J. Tailleur and M. Cates. "Statistical mechanics of interacting run-and-tumble bacteria." *arXiv preprint arXiv:0803.1069*.

[176] M. Cates and J. Tailleur. "When are active Brownian particles and run-and-tumble particles equivalent? Consequences for motility-induced phase separation." *EPL (Europhysics Letters)*, **101**, 2, (2013), 20010.

[177] J. Stenhammar, A. Tiribocchi, R. J. Allen, D. Marenduzzo and M. E. Cates. "A continuum theory of phase separation kinetics for active Brownian particles." *arXiv preprint arXiv:1307.4373*.

[178] E. F. Keller and L. A. Segel. "Model for chemotaxis." *Journal of Theoretical Biology*, **30**, 2, (1971), 225–234.

[179] M. P. Brenner, L. S. Levitov and E. O. Budrene. "Physical mechanisms for chemotactic pattern formation by bacteria." *Biophysical Journal*, **74**, 4, (1998), 1677–1693.

[180] D. Woodward, R. Tyson, M. Myerscough, J. Murray, E. Budrene and H. Berg. "Spatio-temporal patterns generated by Salmonella typhimurium." *Biophysical journal*, **68**, 5, (1995), 2181–2189.

[181] J. Saragosti, V. Calvez, N. Bournaveas, B. Perthame, A. Buguin and P. Silberzan. "Directional persistence of chemotactic bacteria in a traveling concentration wave." *Proceedings of the National Academy of Sciences*, **108**, 39, (2011), 16235–16240.

[182] R. Golestanian, T. Liverpool and A. Ajdari. "Designing phoretic micro-and nano-swimmers." *New Journal of Physics*, **9**, 5, (2007), 126.

[183] J. Taktikos, V. Zaburdaev and H. Stark. "Collective dynamics of model microorganisms with chemotactic signaling." *Physical Review E*, **85**, 5, (2012), 051901.

[184] G. S. Redner, A. Baskaran and M. F. Hagan. "Reentrant Phase Behavior in Active Colloids with Attraction." *arXiv preprint arXiv:1303.3195*.

[185] H. Stark et al. "Collective motion of squirmers in a quasi-2D geometry." *Bulletin of the American Physical Society*, **58**.

[186] S. M. Fielding. "Hydrodynamic suppression of phase separation in active suspensions." *arXiv preprint arXiv:1210.5464*.

[187] T. Ishikawa and T. Pedley. "Coherent structures in monolayers of swimming particles." *Physical review letters*, **100**, 8, (2008), 088103–088103.

[188] M. Raible and A. Engel. "Langevin equation for the rotation of a magnetic particle." *Applied organometallic chemistry*, **18**, 10, (2004), 536–541.

[189] J. Bialké, H. Löwen and T. Speck. "Microscopic theory for the phase separation of self-propelled repulsive disks." *arXiv preprint arXiv:1307.4908*.

[190] F. Kummel, B. ten Hagen, R. Wittkowski, I. Buttinoni, R. Eichhorn, G. Volpe, H. Lowen and C. Bechinger. "Circular Motion of Asymmetric Self-Propelling Particles." *Phys. Rev. Lett.*, **110**, 19.

[191] S. Badaire, C. Cottin-Bizonne, J. W. Woody, A. Yang and A. D. Stroock. "Shape selectivity in the assembly of lithographically designed colloidal particles." *Journal of the American Chemical Society*, **129**, 1, (2007), 40–41.

[192] M. Mijalkov and G. Volpe. "Sorting of chiral microswimmers." *Soft Matter*.

[193] B. ten Hagen, S. van Teeffelen and H. Löwen. "Brownian motion of a self-propelled particle." *Journal of Physics: Condensed Matter*, **23**, 19, (2011), 194119.

[194] J. Happel and H. Brenner. *Low Reynolds Number Hydrodynamics: With Special Applications to Particulate Media*, vol. 1 of *Mechanics of Fluids and Transport Processes* (Kluwer Academic Publishers, Dordrecht), 2 ed. (1991). ISBN 9-024-72877-0.

[195] B. Carrasco and J. Garcia de la Torre. "Improved hydrodynamic interaction in macromolecular bead models." *Journal of Chemical Physics*, **111**, (1999), 4817.

[196] J. Garcia de la Torre, S. Navarro, M. C. Lopez Martinez, F. G. Diaz and J. J. Lopez Cascales. "HYDRO: a computer program for the prediction of hydrodynamic properties of macromolecules." *Biophysical Journal*, **67**, 2, (1994), 530–531.

[197] J. R. Blake. "Image system for a stokeslet in a noslip boundary." *Proceedings of the Cambridge Philosophical Society - Mathematical and physical sciences*, **70**, (1971), 303.

[198] Y. Han, A. M. Alsayed, M. Nobili, J. Zhang, T. C. Lubensky and A. G. Yodh. "Brownian motion of an ellipsoid." *Science*, **314**, (2006), 626.

[199] Y. Han, A. Alsayed, M. Nobili and A. G. Yodh. "Quasi-two-dimensional diffusion of single ellipsoids: Aspect ratio and confinement effects." *Physical Review E*, **80**, (2009), 011403.

[200] S. van Teeffelen and H. Löwen. "Dynamics of a Brownian circle swimmer." *Physical Review E*, **78**, 2, (2008), 020101.

[201] G. Luna, E. Manini and R. Danovaro. "Large fraction of dead and inactive bacteria in coastal marine sediments: comparison of protocols for determination and ecological significance." *Applied and Environmental Microbiology*, **68**, 7, (2002), 3509–3513.

[202] R. Wittkowski and H. Löwen. "Self-propelled Brownian spinning top: Dynamics of a biaxial swimmer at low Reynolds numbers." *Physical Review E*, **85**, 2, (2012), 021406.

[203] A. Roberts. "The mechanics of gravitaxis in Paramecium." *The Journal of Experimental Biology*, **213**, 24, (2010), 4158–4162.

[204] D.-P. Häder. "Gravitaxis in unicellular microorganisms." *Advances in Space Research*, **24**, 6, (1999), 843–850.

Appendix A

Stochastic Calculus

I will hereafter briefly summarize few basic features of stochastic calculus that are of particular interest to revisit the Langevin equation. In particular, I will introduce and define some tools that can be then applied to the Brownian dynamic of micrometric particles suspended in a liquid. This Appendix does not claim, however, to be a mathematical guideline for the entire stochastic calculus. Many aspects will be in fact overlooked and I will primarily focus on definitions that are relevant to understand the stochastic approach to Brownian motion. For further details and applications as well as for exhaustive mathematical derivations I suggest the reader to refer to Refs. [85, 89].

A stochastic process X is a family of random variables, such as the positions of a particle at different times, and is usually represented mathematically as

$$X = \{X_t : t\epsilon T\} \tag{A.1}$$

Stochastic processes characterize our everyday life and their definition does not only concern Physics: any systems has to be considered stochastic as long as one of its variables is aleatory. Therefore, tons stochastic processes can be defined mathematically. Amongst them, it is useful to introduce here the so-called *Wiener process*, which is strictly related to Brownian diffusion (see Chapter 3). A Wiener process W_t is characterized by a probability of transition from two different states that is drawn from a Gaussian distribution, i.e.

$$\begin{cases} W_t - W_k \sim N(0, t - k) & \text{for } t > k \\ W_0 = 0 \end{cases} \tag{A.2}$$

When no "memory" is involved, stochastic processes are known as *Markovian*. In this case the probability of a certain state (e.g., position) at time $t + 1$ depends merely on the t-state and is not affected by prior events, i.e.

$$Prob\left\{X_{t+1} = j | X_0 = i_0; ...; X_t = i_t\right\} = Prob\left\{X_{t+1} = j | X_t = i_t\right\} \quad \text{(A.3)}$$

For Markovian chains the transition from a generic state i to a final state j can be expressed as the sum of all the intermediate transitions. This means that, if p_{ij} is the probability of transition from the state i to the state j, then

$$p_{ij} = \sum_r p_{ir} p_{rj}. \quad \text{(A.4)}$$

Eq. (A.4) is known as *Chapman-Kolmogorov equality.*

The Chapman-Kolmogorov equality is rather general and holds for several kind of stochastic processes. However, to extend its applicability to physical phenomena we need to introduce additional hypothesis. These additional restrictions are typical of the so-called *diffusion processes.*

A Markov process X belongs to the diffusive subclass if:

- X is homogeneous.

- The transition probabilities are twice continuously differentiable.

- The transition moments (see below for definition) are proportional to the time difference.

Under these conditions, the Chapman-Kolmogorov equality for the transition probabilities can be rewritten in a continuous form as

$$p(x, t + \Delta t | y, 0) = \int p(x, t + \Delta t | z, t) p(z, t | y, 0) dz \quad \text{(A.5)}$$

where x, y and z outline here three different states.

Eq. (A.5) can be modify to assume a more useful form. In particular, it can be shown [85] that from Chapman-Kolmogorov continuous equality one can derive the following differential equation for the transition probabilities.

$$\frac{\partial p(x, t | y, 0)}{\partial t} = -\frac{\partial}{\partial x}(A(x)p) + \frac{1}{2}\frac{\partial^2}{\partial x^2}(B(x)p) \quad \text{(A.6)}$$

where $A(X)$ and $B(x)$ are the transition moments defined in the short time limit as:

$$A(x) = \lim_{\Delta t \to 0} \int (x - z) p(x, \Delta t | z, 0) dz \quad \text{(A.7)}$$

$$B(x) = \lim_{\Delta t \to 0} \int (x - z)^2 p(x, \Delta t | z, 0) dz \quad \text{(A.8)}$$

Eq. (A.6) is the renowned *Fokker-Plank equation* (aka *forward Kolmogorov equation*) and it is the main tool used to determine the probability distributions in Brownian dynamics.

Hereafter, I am going to derive the form of the Fokker-Plank equation employed on those stochastic processes of interest for physical phenomena.

Let us consider a Markovian process $Y(t)$ that obeys the following differential equation:

$$\begin{cases} dY(t) = b(Y(t), t)dt + \sigma(Y(t), t)dW_t \\ Y(0) = y_0 \end{cases} \tag{A.9}$$

being W_t the Wiener process defined in (A.2). Clever readers recognize in (A.9) a general form of the Langevin equation (3.2); for this reason $b(Y(t), t)$ and $\sigma(Y(t), t)$ are addressed as *drift coefficient* and *diffusion coefficient*, respectively.

A stochastic process $Y(t)$ that satisfies (A.9) is equally known as *Ito's process* and, in its integral form, Eq. (A.9) reads as

$$Y(t) = y_0 + \int_0^t b(Y(s), s)ds + \int_0^t \sigma(Y(s), s)dW(s), \tag{A.10}$$

The integral that contains the Wiener process is ambiguous and has been historically defined in the two ways:

$$\int_0^t \sigma(Y(s), s)dW(s) = \lim \sum \sigma(Y_{s_i})(W_{s_{i+1}} - W_{s_i}) \tag{A.11}$$

$$\int_0^t \sigma(Y(s), s)dW(s) = \lim \sum \sigma\left(\frac{Y_{s_{i+1}} - Y_{s_i}}{2}\right)(W_{s_{i+1}} - W_{s_i}) \tag{A.12}$$

These two definitions belong to Ito and Stratonovich, respectively, and they obviously differ only due to the choice of the nodes of the Riemann integral. The discussion about which definition is more physical and, at the same time, mathematically correct, albeit very fascinating, is beyond the scope of this Appendix. We need however to keep in mind that any result that follows is biased by the interpretation of the integral.

If we consider a generic probability function $p(Y(t), t)$ of the process $Y(t)$, and we calculate the transition moments $A(Y(t))$ and $B(Y(t))$ of Eq. (A.6) for each stochastic variable y_i of the process, we come up with the Ito's and the Stratonovich's formulations of the Fokker-Plank equation (A.6).

$$\frac{\partial p}{\partial t} = -\sum_i \frac{\partial}{\partial y_i}(bp) + \sum_{i,j} \frac{1}{2} \frac{\partial^2}{\partial y_i \partial y_j}(\sigma^2 p) \qquad \text{(Ito)}$$

$$\frac{\partial p}{\partial t} = -\sum_i \frac{\partial}{\partial y_i}\left[\left(b + \frac{1}{2}\sigma\frac{\partial \sigma}{\partial y_i}\right)p\right] + \sum_{i,j} \frac{1}{2} \frac{\partial^2}{\partial y_i \partial y_j}(\sigma^2 p) \quad \text{(Stratonovich)} \tag{A.13}$$

Looking at (A.13) with the eyes of a physicist as we do in the attempt of describing the dynamics of a physical particle in a liquid, the set of variables y_i is given by the phase space $(\overrightarrow{r}, \overrightarrow{v})$. Furthermore, in several physical applications the diffusion coefficient $\sigma(\overrightarrow{r}, \overrightarrow{v}, t)$, luckily, does no longer depend on $\overrightarrow{r}$ and $\overrightarrow{v}$ and the two descriptions match exactly.

Abstract

In dieser Arbeit untersuche ich die wesentlichen Eigenschaften biologischer und künstlicher aktiver Systeme und stelle eine neue Technik zur Herstellung von selbstgetriebenen mikroskopischen Kolloiden vor. Um den Antrieb zu erhalten nutzen wir phoretische Kräfte, welche ins Spiel kommen, wenn ein Janus-Teilchen seine Umgebung asymmetrisch verändert. Erheblicher experimenteller Aufwand wird der Entwicklung aktiver Kolloide gewidmet, welche sich näherungsweise als selbstgetriebene harte Kugeln verhalten. Dies ermöglicht es uns, die Rolle der aktiven Bewegung hinsichtlich ihrer Phänomene unter komplexeren Bedingungen zu untersuchen. Zur Unterstützung unserer experimentellen Erkenntnisse vergleichen wir diese mit numerischen Simulationen von miteinander wechselwirkenden harten Kugeln. Tatsächlich beobachten wir, dass die Nichtgleichgewichtsphysik, welche diese aktiven Objekte beschreibt, voller neuer und überraschender Besonderheiten steckt.